J. Mech. Phys. Solids 206 (2026) 106337

Contents lists available at ScienceDirect

Journal of the Mechanics and Physics of Solids

journal homepage: www.elsevier.com/locate/jmps

A generalized dual potential for inelastic Constitutive Artificial Neural Networks: A JAX implementation at finite strains

Hagen Holthusen [a,*], Kevin Linka [a,b], Ellen Kuhl [c], Tim Brepols [a]

[a] Institute of Applied Mechanics, RWTH Aachen University, Germany
[b] Institute for Continuum and Material Mechanics, Hamburg University of Technology, Germany
[c] Department of Mechanical Engineering, Stanford University, United States

ARTICLE INFO

Keywords:
Dual potential
Neural network
Finite strains
Generalized standard materials
Inelasticity
Automated model discovery

ABSTRACT

We present a methodology for designing a generalized dual potential, or pseudo potential, for inelastic Constitutive Artificial Neural Networks (iCANNs). This potential, expressed in terms of stress invariants, inherently satisfies thermodynamic consistency for large deformations. In comparison to our previous work, the new potential captures a broader spectrum of material behaviors, including pressure-sensitive inelasticity.

To this end, we revisit the underlying thermodynamic framework of iCANNs for finite strain inelasticity and derive conditions for constructing a convex, zero-valued, and non-negative dual potential. To embed these principles in a neural network, we detail the architecture's design, ensuring a priori compliance with thermodynamics.

To evaluate the proposed architecture, we study its performance and limitations discovering visco-elastic material behavior, though the method is not limited to visco-elasticity. In this context, we investigate different aspects in the strategy of discovering inelastic materials. Our results indicate that the novel architecture robustly discovers interpretable models and parameters, while autonomously revealing the degree of inelasticity.

The iCANN framework, implemented in JAX, is publicly accessible at https://doi.org/10.5281/zenodo.14894687.

1. Introduction

Constitutive material modeling plays a crucial role in understanding the behavior of history-dependent materials, as it allows for accurate predictions of their response under various loading conditions. The selection of an appropriate material model requires extensive expertise, particularly when addressing both elastic and inelastic behaviors which are often strongly coupled. A flawed choice can lead to a focus on optimizing material parameters rather than identifying the most suitable model for the material's behavior.

It is important to recognize that the expertise of professionals is often related to their practical experience, which can lead to biases in the modeling process. This subjectivity has the potential to influence the selection of models and parameters, thereby constraining the exploration of alternative approaches.

In this context, neural networks which are grounded in physical principles – whether strongly or weakly – can provide significant assistance, besides model-free approaches (Eggersmann et al., 2019; Prume et al., 2023). Such neural networks are particularly valuable in the field of finite deformations, where complexity is a major challenge. By using advanced computational methods, we

* Correspondence to: Mies-van-der-Rohe-Str. 1, 52074 Aachen, Germany.
E-mail address: hagen.holthusen@ifam.rwth-aachen.de (H. Holthusen).

https://doi.org/10.1016/j.jmps.2025.106337
Received 19 February 2025; Received in revised form 27 June 2025; Accepted 22 August 2025
Available online 12 September 2025

can improve our ability to capture the complex responses of materials under different conditions, ultimately leading to more reliable and effective engineering solutions and paving the way for novel advanced materials.

1.1. State-of-the-art

Neural networks for inelastic materials. In recent years, the use of neural networks has surged across various scientific fields, particularly for analyzing large data sets beyond human analytical capabilities. For instance, Kepner et al. (2019) demonstrate the societal impact of the internet using hypersparse neural networks on a data set of 50 billion packets.

In medical science, neural networks significantly enhance the understanding of complex brain connectivity essential for identifying neurodegenerative diseases, as shown in Xu et al. (2023) with data from 2702 subjects. Additionally, Girardi et al. (2018) utilize an attention-based neural network trained on 600,000 medical notes to detect critical warning symptoms. Moreover, Ferle et al. (2024) combine Long Short-Term Memory networks with Conditional Restricted Boltzmann Machines to predict multiple myeloma events up to twelve months in advance, improving patient care. In the field of mechanics, Nagle et al. (2024) trained a neural network on 1000 individual virtual subjects to predict skin growth.

In continuum mechanics, access to extensive experimental data is often limited, prompting the question of how neural networks can be beneficial in this field. Expert-based neural network architectures offer distinct advantages, particularly when modeling the diverse behaviors of inelastic materials. The phenomena of interest, such as visco-elasticity and plasticity, exhibit variability based on factors like pressure-sensitivity.

Typically, experts evaluate experimental data to determine both the inelastic phenomenon and the corresponding constitutive model equations. These decisions are often influenced by prior experience, introducing bias. Given the complexity of constitutive equations, it is challenging for humans to formulate highly nonlinear relationships accurately.

Neural networks address this limitation by accommodating a wide range of material behaviors and approximating complex nonlinear functions with high accuracy through scaling their depth and width. Recent research has focused on integrating neural networks with machine learning to enhance modeling capabilities in continuum mechanics.

One of the earliest applications of neural networks in the field of solid mechanics was presented by Ghaboussi et al. (1991), who employed a feed-forward neural network to model the path-dependent behavior of concrete. The network was trained to map stress, strain, and stress increments onto strain increments, thereby capturing the material's nonlinear and history-dependent response. Later, Le et al. (2015) applied neural networks within the context of computational homogenization to learn the macroscopic effective potential of heterogeneous materials, from which both the stress and the tangent stiffness tensor were derived. Bessa et al. (2017) further extended the use of feed-forward neural networks to facilitate the design and modeling of complex material systems, including inelastic behaviors such as plasticity. Among the first, a notable advancement was made by Mozaffar et al. (2019), who utilized recurrent neural networks to predict stress evolution based on microstructural features, time, and strain history, thereby enabling a more accurate modeling of plastic deformation. Despite these advancements, none of the aforementioned approaches incorporated physics-based constraints explicitly, and thus did not enforce physical laws *a priori*.

One of the pioneering thermodynamics-based networks was introduced in Masi et al. (2021), focusing specifically on inelastic multiscale modeling (Masi and Stefanou, 2022) and the inelastic evolution process (Masi and Stefanou, 2023). Further advancements by Piunno et al. (2025) employed proper orthogonal decomposition to extract macroscopic internal state variables, thereby enriching the data set for training the network. A hierarchical discovery framework that aligns with thermodynamic principles has been proposed in Zhang et al. (2025).

As'ad and Farhat (2023a) proposed a mechanics-informed neural network (As'ad et al., 2022) aimed at elucidating the behavior of visco-elastic solids. Physics-augmented neural networks (Klein et al., 2023; Kalina et al., 2024) exploit fundamental principles from continuum mechanics, such as polyconvexity of the Helmholtz free energy, facilitating discoveries related to visco-elasticity (Rosenkranz et al., 2024) and thermo-elasticity (Fuhg et al., 2024b). In this context, Tac et al. (2022) proposed a methodology that integrates deformation invariants with the architecture of neural ordinary differential equations.

To uncover inelastic materials characterized by an inelastic potential, the idea of input convex neural networks (Amos et al., 2017) is particularly helpful due to their ability to ensure thermodynamically consistent designs. For example, physics-informed neural networks developed for elasto-viscoplasticity discovery align with this network architecture (Eghtesad et al., 2024).

The unsupervised learning framework EUCLID incorporates Generalized Standard Materials (GSM) – a method also used by Flaschel et al. (2024) – into its architecture to autonomously identify plasticity under small strain conditions (Flaschel et al., 2022, 2023). This framework has recently been extended to address non-associative pressure-sensitivity under small strains (Xu et al., 2025). Additionally, Upadhyay et al. (2024) utilized a dissipation potential based on the rate of the right Cauchy–Green tensor to characterize finite visco-elastic behavior within a GSM framework.

In scenarios involving damage, a built-in physics neural network was proposed by Tac et al. (2024), while fracture problems were addressed through generalizable symbolic regression techniques in Yi et al. (2025). Moreover, a deep neural network capable of automatically locating and inserting regularized discontinuities for modeling brittle fractures was introduced in Baek and Chen (2024).

We adopt the approach established by Constitutive Artificial Neural Networks (CANNs) (Linka et al., 2021; Linka and Kuhl, 2023), which were extended to visco-elasticity based on a Prony series in Abdolazizi et al. (2024). Recently, the idea of CANNs served as foundation for constitutive Kolmogorov Arnold networks (Abdolazizi et al., 2025). Its generalization to inelastic behavior (iCANN) under finite strains was proposed in Holthusen et al. (2024a,b) and investigated in studies on visco-elasticity and elasto-plasticity with kinematic hardening (Boes et al., 2024), as well as applications to biological tissue growth (Holthusen et al., 2025). Although

this custom-designed architecture inherently satisfies thermodynamic consistency for inelastic materials, it has certain limitations regarding scalability concerning depth and width and fails to incorporate pressure sensitivity effectively.

Therefore, in this study, we explore methodologies for transitioning traditional feed-forward architectures onto the iCANN framework. Our novel architecture has similarities to recent contributions from Jadoon et al. (2025), who pertain to finite elasto-plasticity and share conceptual foundations with iCANNs. However, unlike Jadoon et al. (2025), we fully custom-design our feed-forward network based on comprehensive discussions aimed at achieving a thermodynamically consistent yet generalized potential.

This overview of neural networks applied within the realm of thermodynamically consistent discovery of inelastic materials is not exhaustive; indeed, data-driven mechanics is an expanding field. Therefore, interested readers are encouraged to consult recent survey articles such as Linden et al. (2023), Watson et al. (2024) and Fuhg et al. (2024a), which discuss methodologies for integrating physics into neural network architectures.

Discovery of inelastic neural networks. As mentioned by Battalgazy et al. (2025), different constitutive models can describe specific mechanical behaviors depending on parameter variations. The authors proposed a Bayesian-based procedure that combines model selection with parameter identification. Similarly, neural networks in continuum mechanics face challenges; as their architectures become more generalized, encompassing various inelastic phenomena, the complexity of the discovery process increases.

While highly generalizable, dense networks offer numerous advantages, they pose challenges in uniquely identifying the network's weights. In this context, obtaining a sparse network during the discovery process is preferred over a dense one, as it can be considered 'unique' to a certain extent. Regularizing the network's weights in thermodynamics-based architectures has proven to be a valuable tool in this regard (McCulloch et al., 2024). This emphasis on sparsity not only enhances the model's interpretability but also aligns with the objective of extracting meaningful insights from the underlying physical processes.

This consideration becomes increasingly critical in scenarios where data is subject to uncertainties (Linka et al., 2025), as establishing a deterministic relationship between stresses and strains may often be unrealistic. Strategically, incrementally increasing the network's complexity could facilitate the identification of a unique network configuration (Linka and Kuhl, 2024).

The challenge of creating a 'rich' data set that enables optimal training of neural networks is gaining importance. On a structural level, this raises questions about how to design test specimens that maximize information extraction, which has been explored for one-shot identification in Ghouli et al. (2025). Additionally, microstructural simulations serve as powerful tools for enriching macroscopic data sets (Prume et al., 2025). In this regard, the work presented in Zhang et al. (2024) provides methodologies for reconstructing microstructures from extremely limited data sets.

1.2. Hypothesis

We hypothesize that leveraging the depth and width of neural networks within a dual potential framework enables the modeling and discovery of a broad spectrum of inelastic material behaviors, including pressure-sensitive inelastic flow. By scaling the complexity of the neural network architecture, we aim to capture increasingly sophisticated material responses. Furthermore, we anticipate that utilizing sufficiently 'rich' data sets will lead to accurate model development and reliable training outcomes.

In this initial phase of our work, we simplify the problem by neglecting both intrinsic and induced directional influences. Consequently, we do not incorporate preferred directions (i.e. anisotropy) in the formulation of the Helmholtz free energy, we disregard hardening effects, and we assume that the potential depends solely on the driving force.

To ensure full accessibility of the source code and to facilitate reproducibility, we implement the entire framework and training scheme using `JAX` (Bradbury et al., 2018).

1.3. Outline

We begin with a description of the constitutive framework for inelastic materials at finite strains, applicable to a wide range of materials, in Section 2. There, we formulate the dual/pseudo potential in terms of stress invariants and comment on its connection to Generalized Standard Materials in Section 2.1. In Section 3, we present the novel neural network architecture of the generalized dual potential embedded in a recurrent context, discussing time discretization schemes and our regularization approach. Therefore, in Section 3.1.1, we briefly discuss mathematical properties to obtain a potential that satisfies thermodynamics a priori. In Section 3.1.3, we show how well-known models, such as the *von Mises* or *Drucker–Prager* models, are included in the architecture. Afterwards, in Section 4, we train our network on artificial and experimentally obtained data and evaluate its performance. Our results are critically assessed in Section 5, including a discussion on currently observed limitations of the approach. Finally, in Section 6, we conclude on the proposed method and outline possible future investigations.

2. Constitutive framework for finite strain inelasticity

In this section, we briefly outline the underlying constitutive framework for general inelastic materials at finite strains, which are modeled using the multiplicative decomposition of the deformation gradient. For this, we introduce two fundamental scalar-valued quantities: The Helmholtz free energy, ψ, as well as a dual potential, ω. All constitutively dependent quantities can be derived from these thermodynamic potentials. This dual potential approach is certainly not the only method for modeling inelastic behavior.

We will elucidate its close relationship to Generalized Standard Materials (Halphen and Nguyen, 1975), another well-established framework for characterizing inelasticity, in Section 2.1.

Kinematics. We employ the multiplicative decomposition of the deformation gradient, $\boldsymbol{F} = \boldsymbol{F}_e\boldsymbol{F}_i$, into an elastic part, $\boldsymbol{F}_e$, and an inelastic part, $\boldsymbol{F}_i$, cf. Eckart (1948), Kröner (1959), Sidoroff (1974) and Rodriguez et al. (1994). Both determinants of the individual parts are greater than zero. Conceptually, we introduce an intermediate configuration, relative to which the elastic response is characterized. Unfortunately, the multiplicative decomposition is non-unique, i.e. we may superimpose any rotation $\boldsymbol{F} = \boldsymbol{F}_e\boldsymbol{Q}^{\dagger T}\boldsymbol{Q}^{\dagger}\boldsymbol{F}_i =: \boldsymbol{F}_e^{\dagger}\boldsymbol{F}_i^{\dagger}$ where $\boldsymbol{Q}^{\dagger} \in \mathrm{SO}(3)$ with $\mathrm{SO}(3)$ denoting the special orthogonal group. By employing the singular value decomposition, we recognize that $\boldsymbol{F}_i$ and $\boldsymbol{F}_i^{\dagger}$ share the same singular values, and thus, the same stretch tensor $\boldsymbol{U}_i$ resulting from the polar decomposition $\boldsymbol{F}_i = \boldsymbol{R}_i\boldsymbol{U}_i$ with $\boldsymbol{R}_i \in \mathrm{SO}(3)$. Thus, we find $\boldsymbol{U}_i$ to be unique, and further, $\boldsymbol{F}_i^{\dagger} = \boldsymbol{R}_i^{\dagger}\boldsymbol{U}_i$ where $\boldsymbol{R}_i^{\dagger} = \boldsymbol{Q}^{\dagger}\boldsymbol{R}_i$. Lastly, we introduce an appropriate stretch measure of the elastic stretches $\boldsymbol{C}_e = \boldsymbol{F}_e^T\boldsymbol{F}_e = \boldsymbol{Q}^{\dagger}\boldsymbol{F}_e^{\dagger T}\boldsymbol{F}_e^{\dagger}\boldsymbol{Q}^{\dagger T}$, which however, is non-unique.

Clausius–Planck inequality. Any constitutive framework for solids must satisfy the Clausius–Planck inequality $\mathcal{D} := -\dot{\psi} + 1/2\,\boldsymbol{S} : \dot{\boldsymbol{C}} \geq 0$ where $\boldsymbol{S}$ denotes the second Piola–Kirchhoff stress, while $\boldsymbol{C} = \boldsymbol{F}^T\boldsymbol{F}$ refers to the right Cauchy–Green tensor. For the time being, we assume the Helmholtz free energy to be a scalar-valued isotropic function (Spencer, 1971; Zheng, 1994) depending solely on $\boldsymbol{C}_e$, i.e. $\psi = \hat{\psi}(\boldsymbol{C}_e)$. Hence, we obtain the following, cf. (Dettmer and Reese, 2004)

$$\mathcal{D} = \left(\boldsymbol{S} - 2\,\boldsymbol{F}_i^{-1}\,\frac{\partial\psi}{\partial\boldsymbol{C}_e}\,\boldsymbol{F}_i^{-T}\right) : \frac{1}{2}\,\dot{\boldsymbol{C}} + \underbrace{2\,\boldsymbol{C}_e\,\frac{\partial\psi}{\partial\boldsymbol{C}_e}}_{=:\boldsymbol{\Sigma}} : \underbrace{\dot{\boldsymbol{F}}_i\boldsymbol{F}_i^{-1}}_{=:\boldsymbol{L}_i} \geq 0 \tag{1}$$

where we introduce the elastic Mandel-like stress $\boldsymbol{\Sigma}$, which is symmetric since ψ is an isotropic function of $\boldsymbol{C}_e$, cf. Svendsen (2001).[1] Noteworthy, since $\boldsymbol{\Sigma}$ solely depends on $\boldsymbol{C}_e$, the elastic Mandel-like stress is also non-unique, i.e. $\boldsymbol{\Sigma} = \boldsymbol{Q}^{\dagger}\boldsymbol{\Sigma}^{\dagger}\boldsymbol{Q}^{\dagger T}$. Following the arguments of Coleman and Noll (1961, 1963) and Coleman and Gurtin (1967), we assume the term in brackets in Inequality (1) to be zero, revealing the state law for $\boldsymbol{S}$. Consequently, as $\boldsymbol{\Sigma}$ is symmetric, we can reduce the dissipation inequality to

$$\mathcal{D}_{red} := \boldsymbol{\Sigma} : \boldsymbol{D}_i \geq 0 \tag{2}$$

where $\boldsymbol{D}_i := \mathrm{sym}(\boldsymbol{L}_i)$ is the symmetric part of $\boldsymbol{L}_i$. To satisfy the reduced dissipation inequality for arbitrary processes, we will introduce a dual potential, $\omega = \hat{\omega}(\boldsymbol{\Sigma})$, which is assumed to be a scalar-valued isotropic function in order to be independent of the superimposed rotation $\boldsymbol{Q}^{\dagger}$.

Co-rotated intermediate configuration. We have observed that the relevant constitutive quantities, such as $\boldsymbol{C}_e$ and $\boldsymbol{\Sigma}$, suffer from an inherent rotational non-uniqueness. This poses challenges in computing these quantities and derivatives with respect to those, for instance $\frac{\partial\psi}{\partial\boldsymbol{C}_e}$. To address this issue in our numerical implementation, we adopt the approach suggested by Holthusen et al. (2023a) and introduce a co-rotated intermediate configuration. In short, this approach pulls all non-unique quantities back by either $\boldsymbol{R}_i$ or $\boldsymbol{R}_i^{\dagger}$, i.e. $\bar{(\bullet)} := \boldsymbol{R}_i^T\,(\bullet)\,\boldsymbol{R}_i = \boldsymbol{R}_i^{\dagger T}\,(\bullet)^{\dagger}\,\boldsymbol{R}_i^{\dagger}$. Consequently, we obtain the following unique quantities

$$\bar{\boldsymbol{C}}_e = \boldsymbol{U}_i^{-1}\boldsymbol{C}\boldsymbol{U}_i^{-1}, \quad \boldsymbol{S} = 2\,\boldsymbol{U}_i^{-1}\,\frac{\partial\psi}{\partial\bar{\boldsymbol{C}}_e}\,\boldsymbol{U}_i^{-1}, \quad \bar{\boldsymbol{\Sigma}} = 2\,\bar{\boldsymbol{C}}_e\,\frac{\partial\psi}{\partial\bar{\boldsymbol{C}}_e}, \quad \bar{\boldsymbol{D}}_i = \mathrm{sym}\left(\dot{\boldsymbol{U}}_i\,\boldsymbol{U}_i^{-1}\right). \tag{3}$$

Noteworthy, the co-rotated pullback preserves both the symmetry as well as the eigenvalues, which is considered an advantage.

Potential-based evolution equation. It remains to introduce an evolution equation for $\bar{\boldsymbol{D}}_i$ in a thermodynamic consistent way such that Inequality (2) is satisfied for arbitrary processes. Therefore, we postulate the existence of a pseudo potential (Kestin and Rice, 1969), which we may identify as the dual potential resulting from the Legendre-Fenchel transformation of the 'classical' dissipation potential (see Section 2.1) known from Generalized Standard Materials (Halphen and Nguyen, 1975), viz.

$$\bar{\boldsymbol{D}}_i = \frac{\partial\omega\left(\bar{\boldsymbol{\Sigma}}\right)}{\partial\bar{\boldsymbol{\Sigma}}}. \tag{4}$$

According to Germain et al. (1983), the dissipation inequality is naturally fulfilled if ω is *convex*, *zero-valued*, and *non-negative* with respect to $\bar{\boldsymbol{\Sigma}}$ (Holthusen et al., 2025).[2]

Invariant representation. As discussed above, the dual potential is assumed to be an isotropic function of $\bar{\boldsymbol{\Sigma}}$, and can, thus, be expressed in terms of its invariants. Here, we choose the common stress invariants $I_1^{\bar{\Sigma}} := \mathrm{tr}(\bar{\boldsymbol{\Sigma}})$, $J_2^{\bar{\Sigma}} := 1/2\,\mathrm{tr}(\mathrm{dev}(\bar{\boldsymbol{\Sigma}})^2)$, and $J_3^{\bar{\Sigma}} := 1/3\,\mathrm{tr}(\mathrm{dev}(\bar{\boldsymbol{\Sigma}})^3)$. With these invariants at hand, the evolution equation reduces to

$$\bar{\boldsymbol{D}}_i = \frac{\partial\omega^*}{\partial\bar{\boldsymbol{\Sigma}}} = \frac{\partial\omega^*}{\partial I_1^{\bar{\Sigma}}}\,\boldsymbol{I} + \frac{\partial\omega^*}{\partial J_2^{\bar{\Sigma}}}\,\mathrm{dev}\left(\bar{\boldsymbol{\Sigma}}\right) + \frac{\partial\omega^*}{\partial J_3^{\bar{\Sigma}}}\,\mathrm{dev}\left(\mathrm{dev}\left(\bar{\boldsymbol{\Sigma}}\right)^2\right) \tag{5}$$

[1] In the case of initial anisotropy, ψ is usually assumed to be an isotropic function of $\boldsymbol{C}_e$ and a structural tensor $\boldsymbol{H}$. Note that in this case $\boldsymbol{\Sigma}$ is no longer symmetric.

[2] We may understand the evolution equation as a subderivative $\bar{\boldsymbol{D}}_i \in \partial_{\bar{\Sigma}}\omega\left(\bar{\boldsymbol{\Sigma}}\right)$ in case of non-smooth potentials, where $\partial_{\bar{\Sigma}}\omega\left(\bar{\boldsymbol{\Sigma}}\right)$ denotes the subderivative with respect to $\bar{\boldsymbol{\Sigma}}$, see Germain (1998).

where $\omega^* = \hat{\omega}^*\left(I_1^{\bar{\boldsymbol{\Sigma}}}, \sqrt{J_2^{\bar{\boldsymbol{\Sigma}}}}, \sqrt[3]{J_3^{\bar{\boldsymbol{\Sigma}}}}\right)$. The square and cubic roots are calculated to ensure that all invariants share the same unit. If we plug (5) into the co-rotated version of Eq. (2)

$$\mathcal{D}_{red} = \nabla\omega^*(\mathbf{z}) \cdot \mathbf{z} \geq 0, \quad \mathbf{z} = \begin{pmatrix} I_1^{\bar{\boldsymbol{\Sigma}}} \\ \sqrt{J_2^{\bar{\boldsymbol{\Sigma}}}} \\ \sqrt[3]{J_3^{\bar{\boldsymbol{\Sigma}}}} \end{pmatrix} \tag{6}$$

we observe that the inequality is satisfied if ω^* is convex, zero-valued, and non-negative with respect to its arguments; however, this does not guarantee its convexity with respect to $\bar{\boldsymbol{\Sigma}}$, cf. Collins and Kelly (2002). The reason for this lies in the indefinite Hessian of $J_3^{\bar{\boldsymbol{\Sigma}}}$ with respect to the Mandel-like stress.[3] Nevertheless, non-convex yield surfaces, which are typically modeled as a potential subtracted by a threshold such as the yield stress, are not only of significant practical relevance (Glüge and Bucci, 2017; Matzenmiller et al., 1995; Baghous et al., 2022) but also amenable to numerical treatment (Sheng et al., 2011; Pedroso et al., 2008). As ω^* includes the special case of being convex with respect to $\bar{\boldsymbol{\Sigma}}$, we consider this framework advantageous.

2.1. Relation to generalized standard materials for solids

In the following, we will explain the intrinsic relationship between the present modeling framework for iCANNs and the classical framework of Generalized Standard Materials, the latter of which is well-known in the literature (see e.g. Halphen and Nguyen (1975), Germain et al. (1983) and Flaschel et al. (2023)). We start again with the Helmholtz free energy and assume, for the same reasons as explained above, that it is a scalar-valued isotropic function of quantities in the co-rotated intermediate configuration. Specifically, we assume a dependence of ψ on $\bar{\boldsymbol{C}}_e$ only, i.e. $\psi = \hat{\psi}(\bar{\boldsymbol{C}}_e)$. More general cases in which ψ additionally depends on further internal state variables or structural tensors are, of course, possible. However, since this does not lead to additional insights in the presentation that follows, we will not consider this case for simplicity.

Exploiting again the Clausius–Planck inequality and the chain rule of differentiation, we may arrive at

$$\mathcal{D} = -\dot{\psi} + \frac{1}{2}\boldsymbol{S} : \dot{\boldsymbol{C}} \geq 0 \qquad \Rightarrow \qquad \mathcal{D} = -2\frac{\partial\psi}{\partial\bar{\boldsymbol{C}}_e} : \frac{1}{2}\dot{\bar{\boldsymbol{C}}}_e + \boldsymbol{S} : \frac{1}{2}\dot{\boldsymbol{C}} \geq 0. \tag{7}$$

Considering $\bar{\boldsymbol{C}}_e = \boldsymbol{U}_i^{-1}\boldsymbol{C}\boldsymbol{U}_i^{-1}$, the relation $\dot{\boldsymbol{C}} = \dot{\boldsymbol{U}}_i\bar{\boldsymbol{C}}_e\boldsymbol{U}_i + \boldsymbol{U}_i\dot{\bar{\boldsymbol{C}}}_e\boldsymbol{U}_i + \boldsymbol{U}_i\bar{\boldsymbol{C}}_e\dot{\boldsymbol{U}}_i$, and well-known properties of the scalar product of two second-order tensors, Inequality (7) can directly be rewritten as

$$\mathcal{D} = \left(\bar{\boldsymbol{S}} - 2\frac{\partial\psi}{\partial\bar{\boldsymbol{C}}_e}\right) : \frac{1}{2}\dot{\bar{\boldsymbol{C}}}_e + \bar{\boldsymbol{\Sigma}} : \bar{\boldsymbol{L}}_i \geq 0. \tag{8}$$

Here, $\bar{\boldsymbol{S}} := \boldsymbol{U}_i\boldsymbol{S}\boldsymbol{U}_i$ is the second Piola–Kirchhoff stress tensor relative to the co-rotated intermediate configuration and $\bar{\boldsymbol{\Sigma}} = \bar{\boldsymbol{C}}_e\bar{\boldsymbol{S}}$ denotes the (up to this point generally unsymmetric) Mandel-like stress tensor in the very same configuration. With $\bar{\boldsymbol{L}}_i = \mathrm{sym}(\bar{\boldsymbol{L}}_i) + \mathrm{skew}(\bar{\boldsymbol{L}}_i) = \bar{\boldsymbol{D}}_i + \bar{\boldsymbol{W}}_i$, Expression (8) is finally rewritten as

$$\mathcal{D} = \bar{\boldsymbol{S}}^{\mathrm{dis}} : \frac{1}{2}\dot{\bar{\boldsymbol{C}}}_e + \mathrm{sym}(\bar{\boldsymbol{\Sigma}}) : \bar{\boldsymbol{D}}_i + \mathrm{skew}(\bar{\boldsymbol{\Sigma}}) : \bar{\boldsymbol{W}}_i \geq 0 \tag{9}$$

where $\bar{\boldsymbol{S}}^{\mathrm{dis}} := \left(\bar{\boldsymbol{S}} - 2\frac{\partial\psi}{\partial\bar{\boldsymbol{C}}_e}\right)$ can be considered the irreversible or dissipative part of the stress $\bar{\boldsymbol{S}}$.

To fulfill dissipation inequality (9), it is now customary in the framework of Generalized Standard Materials to assume a scalar-valued dissipation potential[4] $\Omega = \hat{\Omega}\left(\dot{\bar{\boldsymbol{C}}}_e, \bar{\boldsymbol{D}}_i, \bar{\boldsymbol{W}}_i\right)$, expressed in terms of the strain-like rate quantities $\dot{\bar{\boldsymbol{C}}}_e$, $\bar{\boldsymbol{D}}_i$, and $\bar{\boldsymbol{W}}_i$, which is convex, non-negative, and zero-valued at the origin, i.e. $\hat{\Omega}(\mathbf{0},\mathbf{0},\mathbf{0}) = 0$. This potential is conveniently used to derive complementary laws for the thermodynamic conjugate forces, i.e.[5]:

$$\bar{\boldsymbol{S}}^{\mathrm{dis}} = \frac{\partial\Omega}{\partial\dot{\bar{\boldsymbol{C}}}_e}, \qquad \mathrm{sym}(\bar{\boldsymbol{\Sigma}}) = \frac{\partial\Omega}{\partial\bar{\boldsymbol{D}}_i}, \qquad \mathrm{skew}(\bar{\boldsymbol{\Sigma}}) = \frac{\partial\Omega}{\partial\bar{\boldsymbol{W}}_i}. \tag{10}$$

As can be shown, with the above definitions, thermodynamic consistency of the formulation is naturally ensured.

Strain-rate independent dissipation potential. Further consequences for the dissipation potential arise when dealing with solid materials, for which it is usually assumed that purely elastic, but otherwise arbitrary deformations ($\dot{\bar{\boldsymbol{C}}}_e \neq \mathbf{0}$, $\bar{\boldsymbol{D}}_i = \bar{\boldsymbol{W}}_i = \mathbf{0}$) do not cause any dissipation. In this case, it can be inferred from Inequality (9) that

$$\mathcal{D} = \bar{\boldsymbol{S}}^{\mathrm{dis}} : \frac{1}{2}\dot{\bar{\boldsymbol{C}}}_e = 0 \qquad \Rightarrow \qquad \bar{\boldsymbol{S}}^{\mathrm{dis}} = \frac{\partial\hat{\Omega}}{\partial\dot{\bar{\boldsymbol{C}}}_e} = \mathbf{0}. \tag{11}$$

[3] For a more in depth discussion on the thermodynamic consistency, the reader is kindly referred to Appendix A.1.

[4] As in case of the Helmholtz free energy ψ, we may directly formulate the dissipation potential Ω as a scalar-valued isotropic function of quantities in the co-rotated intermediate configuration, in order to avoid any ambiguities due to arbitrary rotations of the intermediate configuration.

[5] In case of a non-smooth dissipation potential Ω, the partial derivatives in (10) and the following should be understood as subderivatives.

In other words, it can be concluded that the dissipation potential cannot be a function of the elastic strain rate $\dot{\bar{\boldsymbol{C}}}_e$ in this case.[6] Furthermore, as the second Piola–Kirchhoff stress tensor relative to the intermediate configuration becomes $\bar{\boldsymbol{S}} = 2\frac{\partial \psi}{\partial \bar{\boldsymbol{C}}_e}$, this immediately leads to a symmetric Mandel-like stress tensor $\bar{\boldsymbol{\Sigma}} = \bar{\boldsymbol{C}}_e\,\bar{\boldsymbol{S}} = 2\,\bar{\boldsymbol{C}}_e\,\frac{\partial \psi}{\partial \bar{\boldsymbol{C}}_e}$ (see also $(3)_3$), i.e. $\mathrm{sym}(\bar{\boldsymbol{\Sigma}}) = \bar{\boldsymbol{\Sigma}}$ and $\mathrm{skew}(\bar{\boldsymbol{\Sigma}}) = \boldsymbol{0}$. The Clausius–Planck inequality therefore reduces to

$$D_{red} = \bar{\boldsymbol{\Sigma}} : \bar{\boldsymbol{D}}_i \geq 0, \tag{12}$$

such that the dissipation potential needs to be a function of $\bar{\boldsymbol{D}}_i$ only, i.e. $\Omega = \hat{\Omega}(\bar{\boldsymbol{D}}_i)$ with $\hat{\Omega}(\boldsymbol{0}) = 0$. The complementary law for $\bar{\boldsymbol{\Sigma}}$ is then obtained as

$$\bar{\boldsymbol{\Sigma}} = \frac{\partial \Omega}{\partial \bar{\boldsymbol{D}}_i}. \tag{13}$$

Dual dissipation potential in terms of stress-like quantities. Finally, by means of a Legendre-Fenchel transformation of Ω, a dual dissipation potential ω in terms of the stress-like quantity $\bar{\boldsymbol{\Sigma}}$ can be derived:

$$\omega = \hat{\omega}(\bar{\boldsymbol{\Sigma}}) = \sup_{\bar{\boldsymbol{D}}_i} \left(\bar{\boldsymbol{\Sigma}} : \bar{\boldsymbol{D}}_i - \hat{\Omega}\left(\bar{\boldsymbol{D}}_i\right) \right). \tag{14}$$

The latter potential is also convex, non-negative, and zero-valued at the origin, i.e. $\hat{\omega}(\boldsymbol{0}) = 0$. It can be employed to define a thermodynamically consistent evolution equation (or complementary law) for the strain-like internal state variable $\bar{\boldsymbol{D}}_i$ via

$$\bar{\boldsymbol{D}}_i = \frac{\partial \omega}{\partial \bar{\boldsymbol{\Sigma}}}. \tag{15}$$

Relation to iCANN framework. The above shows that iCANNs perfectly fit into the framework of Generalized Standard Materials. The only difference to the more classical approach is that, in the iCANN modeling framework presented here, the dual dissipation potential (14) in terms of the stress-like variable $\bar{\boldsymbol{\Sigma}}$ is constructed and identified *directly*. However, this alternative procedure is by no means unusual or disadvantageous, and has been proposed as an equally valid approach by other authors in the past (among many others, Lemaitre and Chaboche, 1994; Chaboche, 1997; Leuschner et al., 2015; Holtzman et al., 2018). One potential can always be constructed from the other, owing to the remarkable duality of the Legendre-Fenchel transformation.

3. Architecture of generalized iCANN

Time integration schemes. To solve the evolution Equation (5) numerically, we employ two different discretization schemes for the interval $[t-1, t]$. The exponential integrator map is well suited in the finite strain regime as it, for instance, preserves the volume in case of an absence of hydrostatic pressure. Moreover, as shown in Holthusen et al. (2025), the exponential integrator satisfies that the isochoric invariants of $\boldsymbol{U}_i$ are preserved if the deviator of $\bar{\boldsymbol{\Sigma}}$ is equal to zero.

First, we employ an explicit time integration scheme (Holthusen et al., 2023a)

$$\boldsymbol{C}_{i_t} = \boldsymbol{U}_{i_{t-1}} \exp\left(2\,\Delta t_t\,\bar{\boldsymbol{D}}_{i_{t-1}}\right) \boldsymbol{U}_{i_{t-1}}, \quad \boldsymbol{U}_{i_t} = +\sqrt{\boldsymbol{C}_{i_t}} \tag{16}$$

with Δt_t denoting the time increment between t and $t-1$. Although an explicit integration is numerically efficient as no iterative solution is required, it might be less stable than an implicit scheme. Further, we have to compute the square root of $\boldsymbol{C}_{i_t}$. As `JAX` does not provide an implementation of the matrix square root at the current time, we use the generating function proposed in Hudobivnik and Korelc (2016). Due to these reasons, we additionally introduce the following residual of an implicit integration scheme, cf. (Arghavani et al., 2011; Holthusen et al., 2023a)

$$\log\left(\boldsymbol{U}_{i_t}^{-1}\,\boldsymbol{C}_{i_{t-1}}\,\boldsymbol{U}_{i_t}^{-1}\right) + 2\,\Delta t_t\,\bar{\boldsymbol{D}}_{i_t} \overset{!}{=} \boldsymbol{0} \tag{17}$$

where $\log(\bullet)$ refers to the matrix logarithm, which is again computed using a generating function (Hudobivnik and Korelc, 2016). To solve Eq. (17) in an iterative manner, we employ Broyden's method (see Appendix A.3).

Recurrent architecture. History-dependent materials necessitate the processing of sequential data, as their current response depends on the evolution of past states. In the context of neural networks, *recurrent neural networks* (RNNs) provide a conventional framework for modeling such temporal dependencies. An RNN typically consists of a recurrent cell that is *recursively* applied over time. At each time step, the cell receives an input $\mathbf{z}_t$ and produces an output $\mathbf{y}_t$, while also updating a set of internal state variables $\mathbf{h}_t$ that are propagated to the next time step.

The input $\mathbf{z}_t$ generally comprises the current time step's external input $\mathbf{x}_t$ along with the state variables $\mathbf{h}_{t-1}$ from the previous step. Within each RNN cell, one or more feed-forward neural networks are employed to compute both the current output $\mathbf{y}_t$ and the updated hidden state $\mathbf{h}_t$.[7]

In our proposed architecture, the output $\mathbf{y}_t$ corresponds to the second Piola–Kirchhoff stress tensor $\boldsymbol{S}_t$, while the input $\mathbf{x}_t$ consists of the current right Cauchy–Green deformation tensor $\boldsymbol{C}_t$ and the associated time increment Δt_t. The internal states $\mathbf{h}_t$ are interpreted as history variables in the context of computational mechanics.

[6] This does by no means preclude any strain-rate-dependent behavior of the material model, as the rate dependency can be reflected in the evolution of the internal state variables.

[7] An illustration of the architecture of a simple RNN cell is provided in Appendix A.2, which will also serve as for comparison in Section 4.1.1.

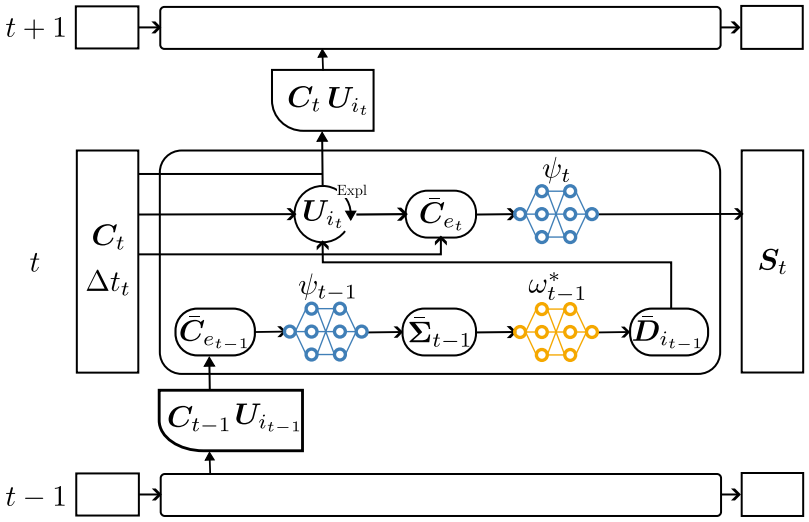

Fig. 1. Explicit recurrent architecture. Schematic representation of our recurrent cell based on explicit time integration. At each time step, the input consists of $\boldsymbol{C}_t$, the time increment Δt_t, and the state variables $\boldsymbol{U}_{i_{t-1}}$ and $\boldsymbol{C}_{t-1}$ from the previous step. The feed-forward networks of the energy, ψ, and the dual potential, ω^*, are evaluated to update the history variable according to Eq. (16). The updated state is propagated to the next time step. Additionally, $\boldsymbol{S}$ is computed based on the updated history variable, cf. Eq. (3).

A crucial distinction from our architecture to conventional RNNs lies in the treatment of these states: Instead of learning $\mathbf{h}_t$ through backpropagation through time, they are computed via the numerical solution of a discretized ordinary differential equation, using either an explicit scheme (16) or an implicit scheme (17). The architecture of the RNN cell differs slightly depending on the chosen integration method, primarily because the implicit variant requires an iterative solution for $\boldsymbol{U}_{i_t}$ at each step. Additionally, the state variables exchanged between successive time steps differ by integration scheme. For explicit integration, the state includes the deformation tensor $\boldsymbol{C}_{t-1}$ from the previous step.

The architectures of the RNN cells for both the explicit and implicit schemes are depicted in Figs. 1 and 2, respectively. As shown, each cell evaluates feed-forward networks representing the energy and dual potential, both of which contribute to the stress computation.[8] The essential formulas to compute $\bar{\boldsymbol{C}}_e$, $\bar{\boldsymbol{\Sigma}}$, and $\boldsymbol{S}$ can be found in Eq. (3), while $\bar{\boldsymbol{D}}_i$ is computed according to Eq. (5). The specific architectures of the feed-forward networks are discussed in Sections 3.1 and 3.2, respectively.

Loss function. Defining the loss function is critical for accurate neural network training. While neural networks effectively learn complex input–output relationships, their flexibility can lead to overfitting. To mitigate this, we apply weight regularization, a well-established method also effective in training Constitutive Artificial Neural Networks (CANNs) (McCulloch et al., 2024; Linka and Kuhl, 2024). For finite elasticity, studies have demonstrated successful regularization strategies for CANNs. For inelasticity, this still poses an open research question. In contrast to elasticity, where sparsity leads to a reasonably 'unique' solution, inelasticity demands not only a sparse network but also the discovery of the underlying inelastic phenomena hidden in the data. Ideally, if the material behaves for instance purely elastically, the network should assign zero weights to the dual potential.

We define the loss as follows

$$L(\boldsymbol{S};\mathbf{W},\mathbf{b}) = \frac{1}{n_{\text{exp}}}\sum_{\alpha=1}^{n_{\text{exp}}}\frac{1}{n_{\text{data}}}\sum_{\beta=1}^{n_{\text{data}}}\|\boldsymbol{S}'_\beta(\boldsymbol{C}_\beta,\boldsymbol{U}_{i_\beta};\mathbf{W},\mathbf{b}) - \hat{\boldsymbol{S}}'_\beta\|_2^2 + R_\psi(\mathbf{W}_\psi,\mathbf{b}_\psi) + R_{\omega^*}(\mathbf{W}_{\omega^*},\mathbf{b}_{\omega^*}) \tag{18}$$

where $(\bullet)'$ refers to Voigt's notation and $\|(\bullet)\|_2^2$ refers to computing the mean of the sum of squared element-wise differences, known as L_2 loss. Further, n_{exp} denotes the number of experiments used for training, while n_{data} is the number of data points per experiment. The experimentally measured stress is denoted by $\hat{\boldsymbol{S}}$. In addition, R_ψ and R_{ω^*} account for the regularization of the weights and biases of the feed-forward networks of the Helmholtz free energy and the dual potential, respectively. These weights and biases are summarized in $\mathbf{W}$ and $\mathbf{b}$.

3.1. Feed-forward network: Dual potential

Deep feed-forward neural networks, i.e. multiple hidden layers between in- and outputs, serve as universal approximators (Hornik et al., 1989) and can approximate functions to any desired degree of accuracy if complexity of the network is increased. Multilayer networks achieve this by recursively applying linear transformations

$$\mathbf{y}_{k+1} = \mathbf{W}_k^{k+1}\,\mathbf{x}_k + \mathbf{b}^{k+1} \tag{19}$$

[8] For additional details, the reader is referred to the original iCANN formulation in Holthusen et al. (2024a).

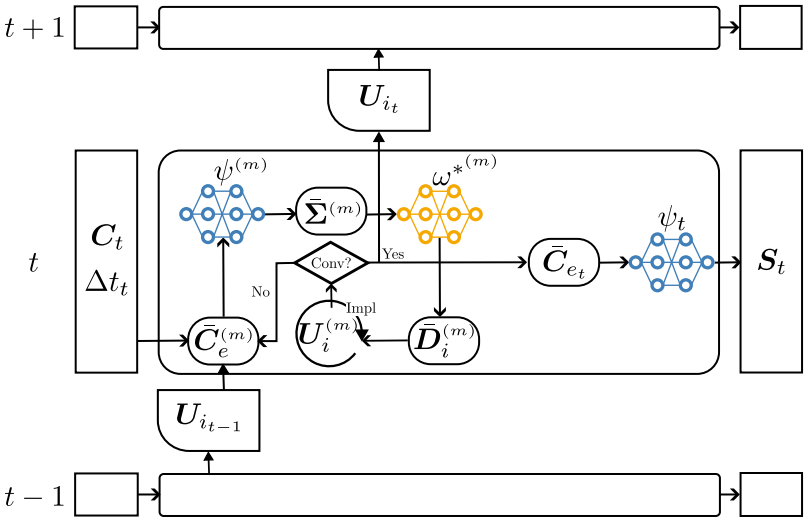

Fig. 2. Implicit recurrent architecture. Schematic representation of our recurrent cell based on implicit time integration. At each time step, the input comprises the current $\boldsymbol{C}_t$, the time increment Δt_t, and the internal state variable $\boldsymbol{U}_{i_{t-1}}$ from the previous step. The updated internal variable $\boldsymbol{U}_{i_t}$ is obtained by iteratively solving Eq. (17), which is indicated by the superscript (m), using Broyden's method (see Appendix A.3). Upon convergence, the current $\bar{\boldsymbol{C}}_{e_t}$ is given by the final iterate $\bar{\boldsymbol{C}}_{e_t}^{(m)}$. The updated state is then propagated to the next time step. In addition, $\boldsymbol{S}_t$ is computed based on the converged internal variable, cf. Eq. (3).

from one layer, k, to the next layer $k+1$. Subsequently, a nonlinear activation function, f, is applied on the linear transformation

$$\mathbf{x}_{k+1} = f(\mathbf{y}_{k+1}). \tag{20}$$

This activation function can vary between layers and can even differ between neurons in the same layer, although this is not common. In the following, we discuss the architecture of a generalized dual potential resulting in a convex, zero-valued, and non-negative function. Specifically, we constrain the layer stacking, permissible activation functions per layer, and the domains of weights, $\mathbf{W}$, and biases, $\mathbf{b}$, between layers. To this end, we briefly recapture some mathematical properties of convexity, zero-valueness, and non-negativity of composed functions in Section 3.1.1. Our discussions inspire the design of the iCANN's dual potential in Section 3.1.2, which is capable of recovering some classical potentials from the literature, see Section 3.1.3.

3.1.1. *Convex, zero-valued, and non-negative dual potential*

To ensure a thermodynamically admissible evolution of inelastic stretches, the dual potential, ω^*, must be convex, non-negative, and zero-valued with respect to its arguments under any arbitrary loading. Since we aim to discover this potential using a multilayer feed-forward neural network, we mathematically outline how such a network can be constructed. Notably, the following considerations are not 'if and only if' conditions – alternative function compositions, for example, may also yield convexity but may probably not align with the proposed framework. However, designing the network according to these principles strictly ensures thermodynamic consistency.

***Convexity:* Composition of a convex function and linear combination.** Suppose we have a function $g : \mathbb{R}^n \to \mathbb{R}$ (linear combination)

$$g(x_1, \dots, x_n) = \mathbf{a}^T\mathbf{x}, \quad \mathbf{x} = \begin{pmatrix} x_1 \\ \vdots \\ x_n \end{pmatrix}, \ \mathbf{a} \in \mathbb{R}^n \tag{21}$$

as well as $f : \mathbb{R} \to \mathbb{R}$ which is convex. The composition $h(\mathbf{x}) = (f \circ g)(\mathbf{x})$ is convex, since the Hessian, $H_h(\mathbf{x})$, is a rank-1 matrix of the outer product

$$H_h(\mathbf{x}) = \frac{\partial^2 f}{\partial g^2}\, \mathbf{a}\mathbf{a}^T. \tag{22}$$

Thus, its only non-zero eigenvalue is $\frac{\partial^2 f}{\partial g^2}\mathbf{a}^T\mathbf{a}$, which is greater or equal to zero since $\frac{\partial^2 f}{\partial g^2} \geq 0$ for a convex function f.

***Convexity:* Positive sum of convex functions.** Let us introduce a family of convex functions $f_1, f_2, \dots, f_n : \mathbb{R}^m \to \mathbb{R}$ and $g : \mathbb{R}^m \to \mathbb{R}$ be the positive sum of these functions, i.e.,

$$g(\mathbf{x}) = \sum_{i=1}^{n} b_i\ f_i(\mathbf{x}), \quad \mathbf{x} \in \mathbb{R}^m, \quad b_i \geq 0 \tag{23}$$

then $g(\mathbf{x})$ is also convex, as each f_i is convex and the positive scaling of convex functions preserves their convexity. Noteworthy, this includes the special case where $n = 1$.

***Convexity:* Composition of convex functions.** We introduce two convex functions $f : \mathbb{R} \to \mathbb{R}$ and $g : \mathbb{R}^n \to \mathbb{R}$. The composition of these functions, $h = (f \circ g)(\mathbf{x})$ with $\mathbf{x} \in \mathbb{R}^n$ is convex if the outer function, f, is monotonically increasing. As g is itself convex, we know that $g(\theta\,\mathbf{x}_1 + (1-\theta)\,\mathbf{x}_2) \leq \theta\, g(\mathbf{x}_1) + (1-\theta)\, g(\mathbf{x}_2)\ \forall\, \mathbf{x}_1, \mathbf{x}_2 \in \mathbb{R}^n$ and $\theta \in [0,1]$. Further, since f is non-decreasing, we observe the following

$$f\left(g(\theta\,\mathbf{x}_1 + (1-\theta)\,\mathbf{x}_2)\right) \leq f\left(\theta\, g(\mathbf{x}_1) + (1-\theta)\, g(\mathbf{x}_2)\right). \tag{24}$$

Having in mind that f itself is convex, we can further conclude that

$$\underbrace{f\left(\theta\, g(\mathbf{x}_1) + (1-\theta)\, g(\mathbf{x}_2)\right)}_{=(f\circ g)(\theta\,\mathbf{x}_1+(1-\theta)\,\mathbf{x}_2)} \leq \underbrace{\theta\, f\left(g(\mathbf{x}_1)\right) + (1-\theta)\, f\left(g(\mathbf{x}_2)\right)}_{\theta(f\circ g)(\mathbf{x}_1)+(1-\theta)(f\circ g)(\mathbf{x}_2)} \quad \forall\, \mathbf{x}_1, \mathbf{x}_2 \in \mathbb{R}^n,\ \theta \in [0,1] \tag{25}$$

which proves that it is sufficient to state that the composition of convex functions is convex if the outer function is non-decreasing.

***Zero-valued:* Composition of zero-valued functions.** We introduce two zero-valued functions $f : \mathbb{R}^n \to \mathbb{R}$ and $g : \mathbb{R}^m \to \mathbb{R}^n$ with $f(\mathbf{0}) = 0$ and $g(\mathbf{0}) = \mathbf{0}$. The composition of these functions is also zero-valued, i.e.

$$(f \circ g)(\mathbf{0}) = 0. \tag{26}$$

***Non-negative:* Composition with non-negative function.** Lastly, let us define two functions $f : \mathbb{R} \to \mathbb{R}^+$ and $g : \mathbb{R}^n \to \mathbb{R}$. The composition of these functions is always greater than or equal to zero, i.e.,

$$(f \circ g)(\mathbf{x}) \geq 0 \quad \forall\, \mathbf{x} \in \mathbb{R}^n \tag{27}$$

since the outer function, f, is always greater than or equal to zero.

Remark 1. As noted, a network designed according to these properties may not encompass all possible constructions of a consistent dual potential. However, given that neural networks are universal approximators (Hornik et al., 1989), we hypothesize that increasing the number of layers and neurons enables us to discover a broad range of inelastic material behaviors.

3.1.2. Custom-designed architecture of feed-forward network

General architecture. The general architecture, whose design is deduced from Section 3.1.1, is illustrated in Fig. 3. We begin by refining the computation methods for the square root of $J_2^{\bar{\Sigma}}$ and the cubic root of $J_3^{\bar{\Sigma}}$

$$\sqrt{x} := \frac{x}{(x+\epsilon_1)^{1/2}}, \quad \sqrt[3]{x} := \frac{x}{(\mathrm{abs}(x)+\epsilon_2)^{2/3}}, \quad \epsilon_1,\, \epsilon_2 \geq 0 \tag{28}$$

in order to be differentiable at zero. In the numerical implementation, we choose $\epsilon_1 = \epsilon_2 = 0.01$.

Next, let us discuss the domain of the weights and biases connecting the different layers. According to Eqs. (21)–(22), the weights between the inputs and the first hidden layer are real-valued $\mathbf{W}_0^{\mathrm{I}} \in \mathbb{R}^{n_{\mathrm{I}} \times n_0}$. Here, n_0 refers to the number of input neurons, while n_{I} represents the total number of neurons in the first hidden layer. For the weights between the first and second hidden layers, the matrix is given as $\mathbf{W}_{\mathrm{I}}^{\mathrm{II}} \in \mathbb{R}_{\geq 0}^{n_{\mathrm{II}} \times n_{\mathrm{I}}}$, where $\mathbb{R}_{\geq 0}$ refers to all real value greater than or equal to zero. Thus, we ensure that while going from one hidden layer to the next, each neuron remains convex, cf. Eq. (23). The weight matrices for subsequent layers, up to $\mathbf{W}_\star^K$, follow a similar definition. In analogy, we introduce the row vector $\mathbf{w}_{\omega^*} \in \mathbb{R}_{\geq 0}^{n_{K+1} \times 1}$. Finally, the biases per activation function, $\mathbf{b}_\star^K$, up the second hidden layer are generally real-valued.

Following the constraints on the weights and biases of the network, we introduce how the choice of activation functions per layer and neuron is limited. Due to Eqs. (22)–(25), we conclude that only the first hidden layer I permits generally convex activation functions, i.e., these functions, f^{I}, might be decreasing. Using a single activation function per layer, as is common in neural networks, severely restricts the choice of decreasing convex functions. To overcome this limitation, we incorporate a diverse set of activation functions in each layer, adhering to our design strategy. The activation functions of each subsequent layer, $f^{\mathrm{II}}, \ldots, f^K$, are only allowed to be non-decreasing to result in a convex function, cf. Eqs. (23) and (25). Additionally, per Eq. (26), all activation functions must be zero-valued to achieve a zero-valued potential.

Lastly, let us consider the case where $K = \mathrm{II}$, cf. Fig. 3. Constructing the network with a single activation function and one neuron per layer, e.g., $f^{\mathrm{I}} \in \{x\}$ and $f^{\mathrm{II}} \in \{\exp(x) - 1\}$, results in the potential $\omega^* = (f^{\mathrm{II}} \circ f^{\mathrm{I}})(x) = \exp(w_0^{\mathrm{I}}\, x) - 1$. This potential is convex and zero-valued, but violates the non-negativity constraint. To address this, we introduce an additional hidden layer, $K+1$, with the same number of neurons as layer K. This final layer employs a single activation function $f^{K+1} \in \{\max(x, 0)\}$, cf. Eq. (27). No weights or biases are introduced between the last two hidden layers,[9] as indicated by dashed lines in Fig. 3.

Specific architecture. With the general architecture at hand, we need to specify the number of layers, the choice of activation functions per layer, and the number of neurons per activation function. In this contribution, we employ the specific architecture shown in Fig. 4. First of all, we enhance the network's inputs by the stress invariants $I_2^{\bar{\Sigma}} := 1/2\,\mathrm{tr}(\bar{\boldsymbol{\Sigma}}^2)$ and $I_3^{\bar{\Sigma}} := 1/3\,\mathrm{tr}(\bar{\boldsymbol{\Sigma}}^3)$. This is

[9] This can be interpreted as a non-trainable identity weight matrix and a zero bias vector.

an easy method of broadening the space of potentials included in our network, see also Section 3.1.3. Note that this does not affect our findings on the potential, see Appendix A.4.

In line with the design of the architecture introduced above, we choose the following set of activation functions per hidden layer

$$\begin{aligned} f^{\mathrm{I}} &\in \{x, |x|^{p_1+1}, \ln(\cosh(|x|^{p_2+1}))\} \\ f^{\mathrm{II}} &\in \{\max(x,0), \exp(x)-1\} \\ f^{\mathrm{III}} &\in \{\max(x,0), \exp(x)-1\}. \end{aligned} \tag{29}$$

Here, we introduce two additional weights, p_1 and p_2, which are discovered during training. These weights are constrained to be greater than or equal to zero, i.e. $p_1, p_2 \geq 0$, to obtain convex activation functions. Moreover, we modify the computation of $|x|^{\alpha+1}$ to guarantee that the function is finite for $x = 0$ and differentiable at $x = 0$

$$|x|^{\alpha+1} := \exp\left((\alpha+1)\ln\left(\mathrm{abs}(u(x)) + \epsilon_1\right)\right), \quad u(x) = x + \mathrm{sgn}(x)\,\epsilon_2, \quad \epsilon_1,\, \epsilon_2 \geq 0 \tag{30}$$

where $\mathrm{sgn}(x)$ refers to the sign function. In the numerical implementation, we choose $\epsilon_1 = \epsilon_2 = 0.0001$. In addition, we introduce biases, $\mathbf{b}_1^{\mathrm{II}} \in \mathbb{R}^{n_{\mathrm{II}}\times 1}_{\leq 0}$ and $\mathbf{b}_1^{\mathrm{III}} \in \mathbb{R}^{n_{\mathrm{III}}\times 1}_{\leq 0}$, for the $\max(x,0)$ activation functions. Noteworthy, the biases must be non-positive to satisfy that the activation function remains zero-valued.

It remains to choose the number of neurons per activation function. For simplicity, we choose the same number of neurons per activation function in each layer. In the first layer, we employ six neurons per function resulting in eighteen neurons in total. For all subsequent layers, we choose four neurons per activation function. Consequently, our specific architecture consist of $90\,(\mathbf{W}_0^{\mathrm{I}}) + 144\,(\mathbf{W}_1^{\mathrm{II}}) + 64\,(\mathbf{W}_{\mathrm{II}}^{\mathrm{III}}) + 8\,(\mathbf{w}_{\omega^*}) + 4\,(\mathbf{b}_1^{\mathrm{II}}) + 4\,(\mathbf{b}_1^{\mathrm{III}}) + 1\,(p_1) + 1\,(p_2) = 316$ weights in total.

Regularization. In Section 3, we introduced the training loss with the regularization R_{ω^*} for the potential. Furthermore, we stated that the regularization should discover a relatively sparse network in order to both be considered as a 'unique' material model and to reveal the inelastic phenomena. Thus, in line with the experiences made in McCulloch et al. (2024) and Linka and Kuhl (2024), we regularize the weights of the last layer, $\mathbf{w}_{\omega^*}$, by a lasso (L_1) regularization to promote sparsity. Additionally, we regularize the weights of the very first hidden layer by an elastic net, which linearly combines lasso and ridge (L_2) regularization, to promote sparsity and mitigate multicollinearity. Lastly, the biases are regularized by lasso. Thus, the overall regularization of the potential reads

$$R_{\omega^*} = \sum_{i=1}^{18}\sum_{j=1}^{5}\left[\lambda_1\left(W^{\mathrm{I}}_{0_{ij}}\right)^2 + \lambda_2\,\mathrm{abs}\left(W^{\mathrm{I}}_{0_{ij}}\right)\right] + \sum_{i=1}^{8}\lambda_3\,\mathrm{abs}\left(w_{\omega^*_i}\right) + \sum_{i=1}^{4}\lambda_4\left[\mathrm{abs}\left(b^{\mathrm{II}}_{1_i}\right) + \mathrm{abs}\left(b^{\mathrm{III}}_{1_i}\right)\right] \tag{31}$$

where we set the regularization parameters to $\lambda_1 = \lambda_2 = \lambda_3 = 0.0001$ and $\lambda_4 = 0.01$ for all training sessions.

3.1.3. Reproduction of classical dual potentials

In the following, we demonstrate that the generalized iCANN architecture, as previously introduced, is capable of recovering a variety of established dual potentials known within the continuum mechanics community. To this end, we streamline the architecture outlined in Section 3.1.2 to its essential neurons, thereby enabling the integration of all these models into a unified architecture. The resulting reduced network is illustrated in Fig. 5. For each of the classical dual potentials examined, we link weight matrices to the material parameters.

The *von Mises* criterion (von Mises, 1913) can be expressed as

$$\omega^*_{vM} = \sqrt{3\,J_2^{\bar{\Sigma}}}, \quad \mathbf{W}_0^{\mathrm{I}} = \begin{pmatrix} 0 & 1 & 0 \\ 0 & 0 & 0 \\ 0 & 0 & 0 \end{pmatrix}, \quad \mathbf{w}_{\mathrm{I}}^{\mathrm{II}} = \begin{pmatrix} \sqrt{3} & 0 & 0 \end{pmatrix} \tag{32}$$

which is mostly applied for ductile materials. At this point, it is already important to note that due to the dense structure of the generalized architecture, the weight matrices are not unique. For instance, for the *von Mises* potential one may exchange the non-zero entries in $\mathbf{W}_0^{\mathrm{I}}$ with those of $\mathbf{w}_{\mathrm{I}}^{\mathrm{II}}$.

Next, we investigate the pressure-sensitive *Drucker–Prager* model (Drucker and Prager, 1952)

$$\omega^*_{DP} = \sqrt{3\,J_2^{\bar{\Sigma}}} + \underbrace{\frac{\sigma_c - \sigma_t}{\sigma_c + \sigma_t}}_{=:\xi} I_1^{\bar{\Sigma}}, \quad \mathbf{W}_0^{\mathrm{I}} = \begin{pmatrix} \xi & \sqrt{3} & 0 \\ 0 & 0 & 0 \\ 0 & 0 & 0 \end{pmatrix}, \quad \mathbf{w}_{\mathrm{I}}^{\mathrm{II}} = \begin{pmatrix} 1 & 0 & 0 \end{pmatrix} \tag{33}$$

which represents a cone within the principal stress space. The yield stresses, σ_c and σ_t, denote the uniaxial yield stress in compression and tension, respectively. It is important to note that ξ might be negative. Note that using the 'original' iCANN architecture (Holthusen et al., 2024a), we were not able to discover the *Drucker–Prager* model, cf. Boes et al. (2024).

The *Bresler-Pister* (Bresler and Pister, 1985) model extends the former potential by a dependence on the quadratic hydrostatic pressure $I_1^{\bar{\Sigma}}$. Usually, this additional dependency is associated with the yield stress under biaxial compression. The potential reads as follows

$$\omega^*_{BP} = \sqrt{3\,J_2^{\bar{\Sigma}}} + \zeta_1\,I_1^{\bar{\Sigma}} + \zeta_2\left(I_1^{\bar{\Sigma}}\right)^2, \quad \mathbf{W}_0^{\mathrm{I}} = \begin{pmatrix} \zeta_1 & \sqrt{3} & 0 \\ 1 & 0 & 0 \\ 0 & 0 & 0 \end{pmatrix}, \quad \mathbf{w}_{\mathrm{I}}^{\mathrm{II}} = \begin{pmatrix} 1 & \zeta_2 & 0 \end{pmatrix} \tag{34}$$

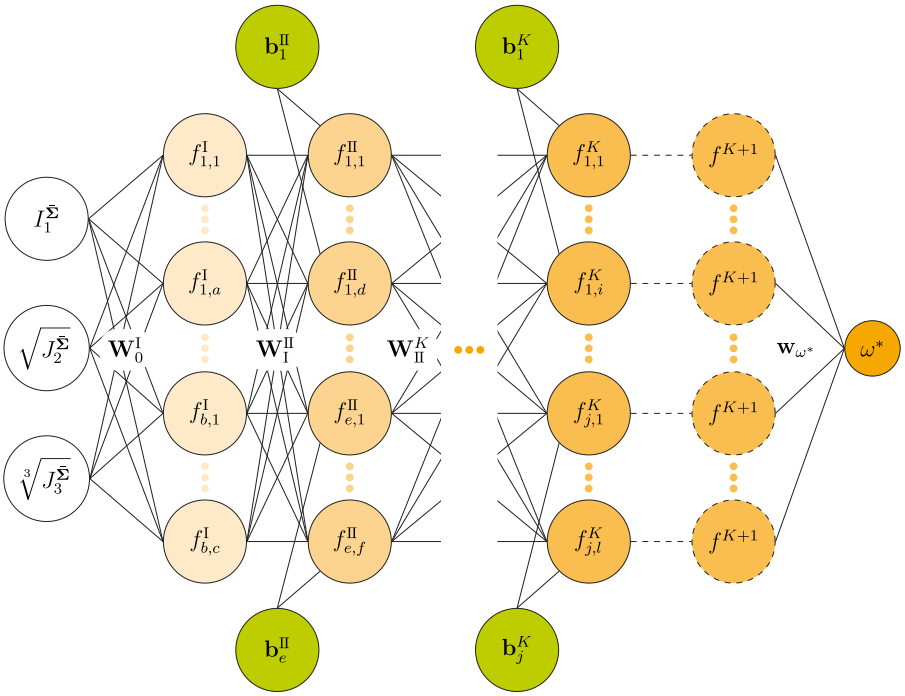

Fig. 3. Schematic of our feed-forward architecture for the dual potential, ω^*, designed to ensure thermodynamic consistency. The network enforces convexity, non-negativity, and a zero-valued potential. Dashed lines indicate neurons without associated weights. Activation functions are denoted as $f_{\alpha,\beta}^{\gamma}$, where γ is the layer index, α specifies the function type, and β indexes the neuron within α. The final layer $(K+1)$ exclusively employs the $\max(x,0)$ activation. The weights are denoted by $\mathbf{W}$ and $\mathbf{w}$, respectively, while $\mathbf{b}$ represents the network's biases.

with the material constants ζ_1 and ζ_2. As for the *Drucker–Prager* model, ζ_1 can be any real number. In contrast, ζ_2 must be positive to be discoverable by the generalized iCANN.

The potential proposed by Stassi-D'Alia (1967) and Tschoegl (1971) represents a paraboloid within the principal stress space

$$\omega_{ST}^* = 3\,J_2^{\bar{\Sigma}} + (\sigma_c - \sigma_t)\,I_1^{\bar{\Sigma}}, \quad \mathbf{W}_0^{\mathrm{I}} = \begin{pmatrix} \sigma_c - \sigma_t & 0 & 0 \\ 0 & \sqrt{3} & 0 \\ 0 & 0 & 0 \end{pmatrix}, \quad \mathbf{w}_{\mathrm{I}}^{\mathrm{II}} = \begin{pmatrix} 1 & 1 & 0 \end{pmatrix} \tag{35}$$

where the difference, $\sigma_c - \sigma_t$, can be negative. Again, this potential cannot be discovered by the original iCANN architecture, see Boes et al. (2024).

A quadratic potential, which is often used to model visco-elasticity at finite strains (Reese and Govindjee, 1998), is expressed in terms of stress invariants as follows

$$\omega_{RG}^* = 0.25\,\mu^{-1}\,J_2^{\bar{\Sigma}} + \frac{\kappa^{-1}}{18}\left(I_1^{\bar{\Sigma}}\right)^2, \quad \mathbf{W}_0^{\mathrm{I}} = \begin{pmatrix} 0 & 0 & 0 \\ 1 & 0 & 0 \\ 0 & 1 & 0 \end{pmatrix}, \quad \mathbf{w}_{\mathrm{I}}^{\mathrm{II}} = \begin{pmatrix} 0 & \kappa^{-1}/18 & 0.25\,\mu^{-1} \end{pmatrix} \tag{36}$$

where μ denotes the material's shear modulus, while κ refers to the bulk modulus.

Lastly, we investigate a smoothed version (Holthusen et al., 2023a) of the maximum principal stress theory, also known as Rankine's theory (Collins, 1993),

$$\omega_{sPs}^* = I_1^{\bar{\Sigma}} + \sqrt{I_2^{\bar{\Sigma}}}, \quad \mathbf{W}_0^{\mathrm{I}} = \begin{pmatrix} 1 & 0 & 1 \\ 0 & 0 & 0 \\ 0 & 0 & 0 \end{pmatrix}, \quad \mathbf{w}_{\mathrm{I}}^{\mathrm{II}} = \begin{pmatrix} 1 & 0 & 0 \end{pmatrix} \tag{37}$$

where it becomes clear why we include also the invariant $I_2^{\bar{\Sigma}}$ into the specific architecture of our proposed generalized dual potential.

3.2. Feed-forward network: Helmholtz free energy

Architecture. As the scope of this manuscript lies on the development of a generalized dual potential, we employ the feed-forward network of the Helmholtz free energy proposed in Holthusen et al. (2024a,b). Fig. 6 illustrates the custom-designed feed-forward network. In contrast to our new proposed network of the potential, the energy network is sparse. As ψ is an isotropic

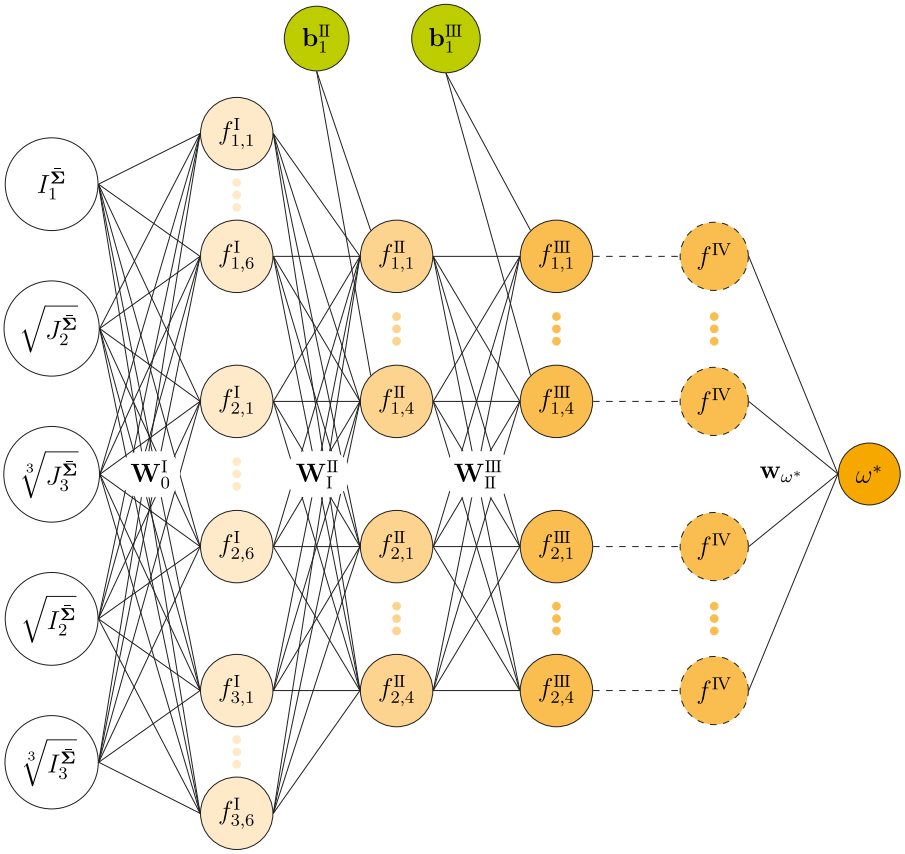

Fig. 4. Specification of our general architecture presented in Fig. 3. The inputs are extended by two invariants, while biases are only associated with the maximum activation function in the second and third layer.

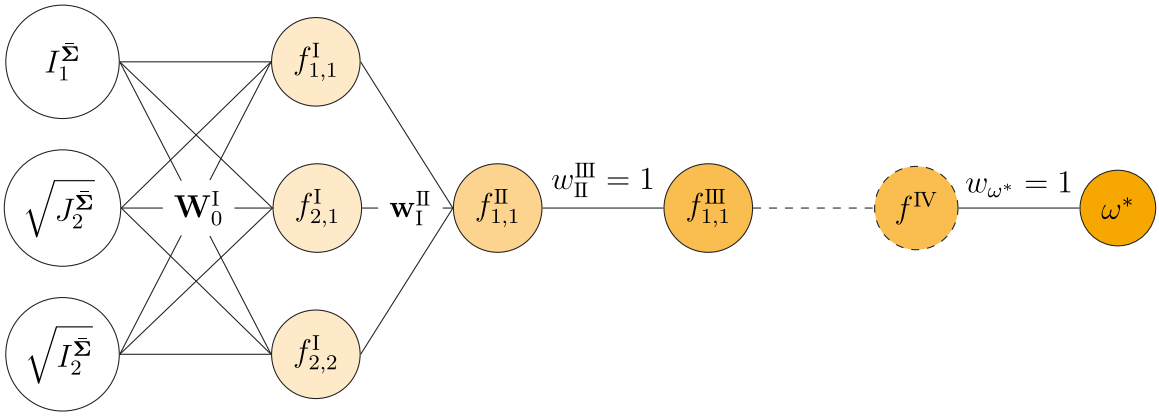

Fig. 5. Reduced architecture of the specific network shown in Fig. 4. For simplicity, the weights between the second and third layers as well as the third layer to the output are set equal to one. The activation functions are chosen as $f^{\mathrm{I}} \in \{x, |x|^{p_1+1}\}$ and f^{II}, $f^{\mathrm{III}} \in \{\max(x, 0)\}$, where the weight p_1 is set equal to one.

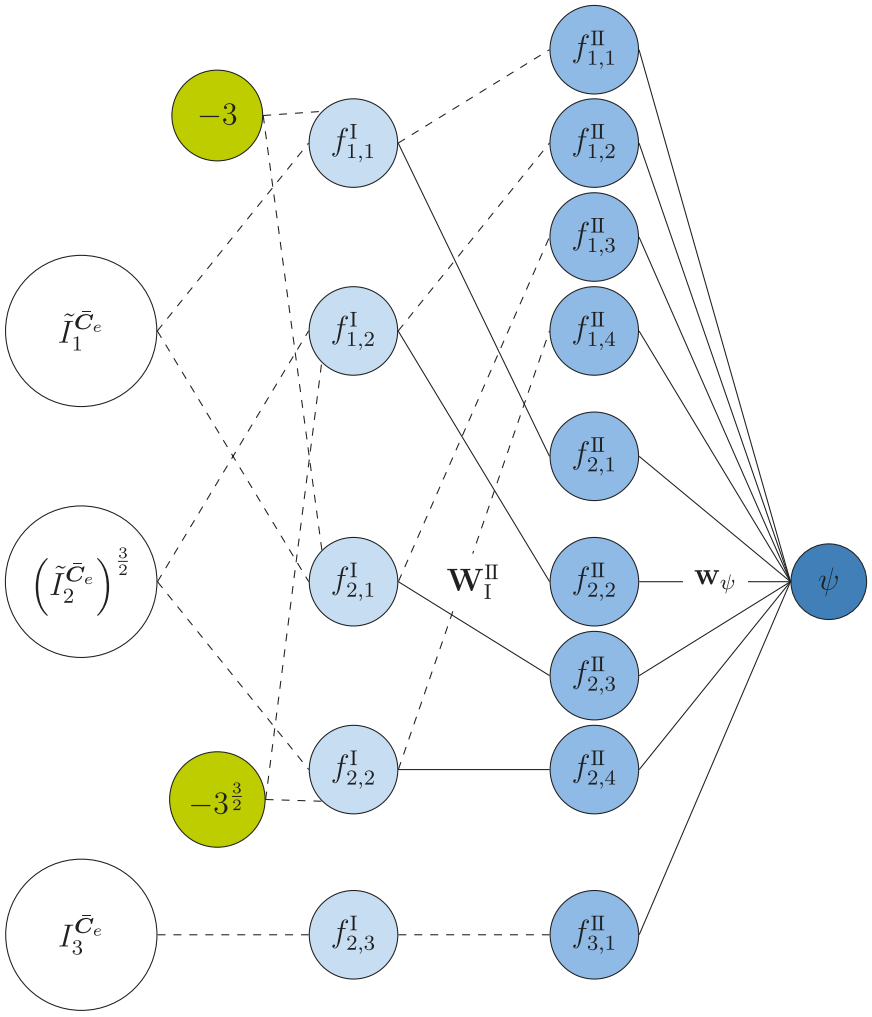

Fig. 6. Schematic of our feed-forward architecture for the Helmholtz free energy, ψ. Dashed lines indicate neurons without associated weights, respectively, being equal to one and non-trainable. The biases are constant and are introduced to ensure a zero-valued energy.

function of $\bar{\boldsymbol{C}}_e$, we express it in terms of invariants. To this end, the determinant, $I_3^{\bar{C}_e} := \det(\bar{\boldsymbol{C}}_e)$, as well as the isochoric invariants, $\tilde{I}_1^{\bar{C}_e} := \mathrm{tr}(\bar{\boldsymbol{C}}_e)/(I_3^{\bar{C}_e})^{1/3}$ and $\tilde{I}_2^{\bar{C}_e} := \mathrm{tr}(\mathrm{cof}(\bar{\boldsymbol{C}}_e))/(I_3^{\bar{C}_e})^{2/3}$, serve as the network's inputs. The latter invariant is raised to the power of $3/2$ to satisfy polyconvexity (Hartmann and Neff, 2003).

For the network, we choose the following set of activation functions per layer

$$\begin{aligned} f^{\mathrm{I}} &\in \{x^2, x\} \\ f^{\mathrm{II}} &\in \{x, \exp(x) - 1, x^{p_3} - 1 - \ln(x^{p_3})\} \end{aligned} \tag{38}$$

where we introduce the weight p_3 in addition to the weights of the network, see Fig. 6. Thus, the total number of weights is $4\,(\mathbf{W}_{\mathrm{I}}^{\mathrm{II}}) + 9\,(\mathbf{w}_\psi) + 1\,(p_3) = 14$ for the network of the energy.

Regularization. As for the dual potential, we regularize the weights introduced for the energy (cf. Eqs. (18) and (31)). According to the experiences made in Holthusen et al. (2023b, 2024a) and Linka and Kuhl (2024), we only employ lasso regularization for the weights of the very last layer, and only regularize the weights associated with the isochoric part of the energy, i.e.,

$$R_\psi = \sum_{i=1}^{8} \lambda_5 \,\mathrm{abs}\left(w_{\psi_i}\right) \tag{39}$$

where λ_5 denotes the regularization parameter which is set to 0.001 within this contribution.

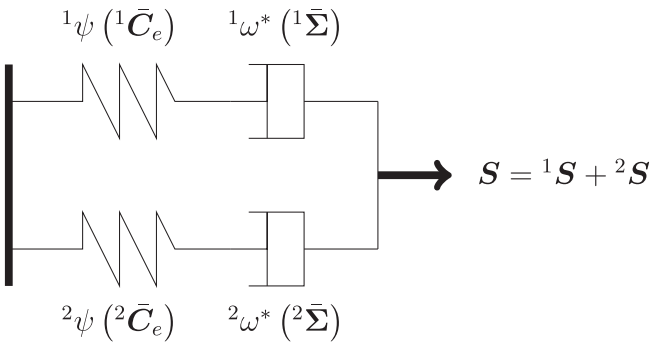

Fig. 7. Rheological representation of the parallel connection of two generalized iCANNs. Each iCANN consists of an individual 'spring', $^1\psi$ or $^2\psi$, and 'dashpot', $^1\omega^*$ or $^2\omega^*$, element with individual states, $^1\boldsymbol{U}_i$ and $^2\boldsymbol{U}_i$, respectively. The entire Helmholtz free energy is $\psi = {}^1\psi + {}^2\psi$, while the overall dual potential is the sum of the individual potentials, i.e., $\omega^* = {}^1\omega^* + {}^2\omega^*$. For both individual iCANNs, the same right Cauchy–Green tensor, $\boldsymbol{C}$, serves as input. Consequently, the outputs are summed up to a single second Piola–Kirchhoff stress, $\boldsymbol{S}$.

4. Results

In the following, we systematically train our generalized iCANN model and evaluate its predictive accuracy on both synthetic (Section 4.1) and experimentally acquired data (Section 4.2). Additionally, we compare explicit and implicit integration schemes, implement a staggered discovery approach, and introduce noise into the data set to assess potential overfitting effects.

To this end, we first consider two distinct artificially generated data sets in Sections 4.1.1 and 4.1.2. These data sets differ in terms of the underlying dual potential as well as the magnitude of dissipated energy. To validate our generalized iCANN model against experimental data, we infer the visco-elastic response of VHB 4910 polymer (Hossain et al., 2012).

Fig. 7 schematically represents the iCANN architecture in terms of a rheological model. Since a *standard* Maxwell element, consisting of a series connection of an 'elastic spring' and a 'viscous dashpot', is insufficient to characterize visco-elastic solids, we employ a parallel configuration of two Maxwell elements ($^1(\bullet)$ and $^2(\bullet)$).[10] This configuration is intended to facilitate the identification of the underlying visco-elastic behavior through training.

For all training sessions, we initialize the network's weights and biases using a uniform random distribution. We maintain fixed lower and upper value bounds across all training scenarios, rather than tuning them to specific problem instances. Furthermore, our regularization parameters remain constant throughout training. The mean squared error serves as the loss function, quantifying the discrepancy between the training data and the neural network's predictions.

The entire computational framework is implemented in JAX (Bradbury et al., 2018), utilizing the ADAM optimizer (Kingma and Ba, 2017) from the Optax library with a learning rate of 0.001. Additionally, we apply gradient clipping based on a maximum global norm, set to 0.001. Our training experience made during the preparation of this study indicates that gradient clipping is particularly crucial for inelastic materials, as it prevents excessive growth in the potential's weights. Uncontrolled weight growth can lead to an unstable evolution equation, potentially resulting in unbounded stress values.

4.1. Discovery of artificial data

In line with Shannon's information theory (Shannon, 1948), 'rich' data sets should enable us to discover a 'unique' set of weights and biases; however, 'rich' does not necessarily mean more data points. Key features such as diverse data sets and higher information entropy prevent overfitting, while the performance during gradient optimization usually improves. In terms of material science and computational discovery, we hypothesize that 'rich' data sets featuring complex, relaxing, multiaxial, and cyclic load paths will help us to discover our weights in the network. Thus, we prescribe the loading path shown in Fig. 8 with $\Delta t = 0.05$ [min] to create a 'rich' data set, which is utilized to obtain stress-time data in Sections 4.1.1 and 4.1.2. To test our discovered weights and biases, we subject the network to uniaxial loading. Here, we compute the remaining entries in Fig. 8 (loading) according to the uniaxial stress constraint with $\Delta t = 0.06$ [min]. Noteworthy, the components of the deformation gradient may vary depending on the energy and potential employed.

4.1.1. Discovering a model for artificial data: Example 1

In this first example, we investigate the network's capabilities to discover the weights and biases of our proposed network in order to accurately describe the material behavior. As alluded in the previous section, we create an artificial data set by subjecting

[10] The term *standard* refers to a dashpot's potential, which is greater than zero for all non-zero stress states.

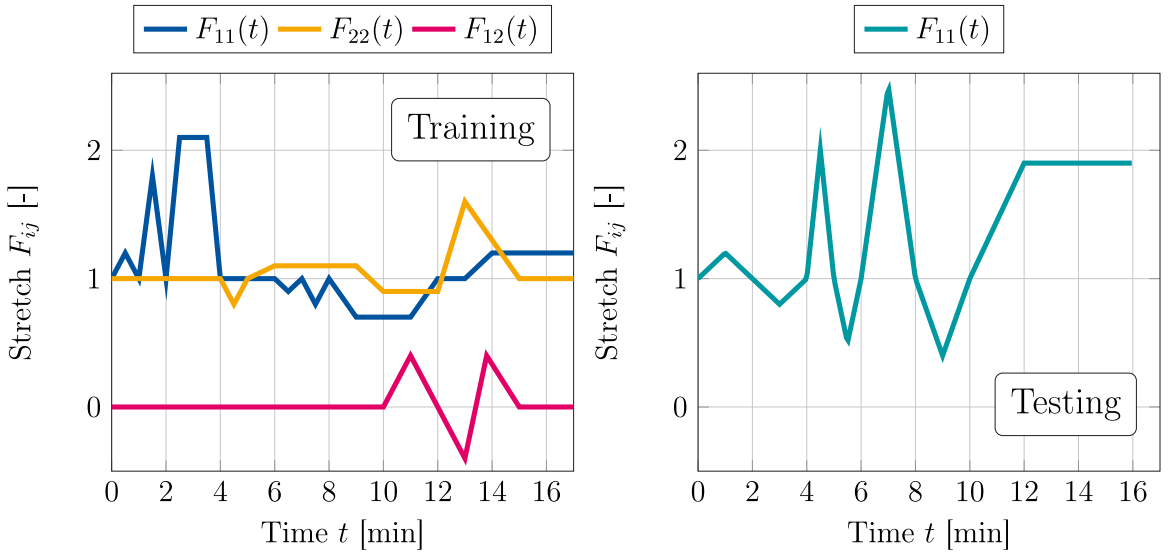

Fig. 8. Left: Deformation gradient components used for creating a training data set. The third entry on the main diagonal, F_{33}, is set to one, while the remaining shear terms are zero. The training set includes multiaxial, cyclic, and relaxation behavior. Right: Prescribed stretch in the main stretch direction for uniaxial loading employed for testing. The remaining components of the deformation gradient are computed according to the constraint that the entries of $\boldsymbol{S}$ in the off-main diagonal direction are zero.

a constitutive model to a complex loading path. For the Helmholtz free energy and the dual potential, we use the following compressible Neo-Hookean model

$$\psi = \frac{\mu}{2}\left(\bar{I}_1^{\bar{C}_e} - 3\right) + \frac{\kappa}{4}\left(I_3^{\bar{C}_e} - 1 - \ln\left(I_3^{\bar{C}_e}\right)\right) + \frac{\mu}{2}\left(\bar{I}_1^{C} - 3\right) + \frac{\kappa}{4}\left(I_3^{C} - 1 - \ln\left(I_3^{C}\right)\right) \tag{40}$$

$$\omega^* = K_1\left(\cosh\left(\frac{J_3^{\bar{\Sigma}}}{J_2^{\bar{\Sigma}} + 1}\right) - 1\right) \tag{41}$$

with $\mu = 1$ [MPa] and $\kappa = 1$ [MPa], and $K_1 = 2$ [1/MPa]. From a rheological viewpoint, Eqs. (40) and (41) describe a 'spring' element connected in parallel to a Maxwell element. Remarkably, the potential is not 'analytically' included in the architecture of the network, but is otherwise arbitrary. However, since neural networks serve as universal approximators, we want to explore the generalized iCANN's capabilities to discover this potential. Additionally, the material parameters are chosen such that there is a high amount of energy dissipation present. The components of the deformation gradient for testing are shown in Fig. 9.

Discovery The weights identified in this study are too numerous to enumerate in this manuscript.[11] However, key components of the weight vector, $\mathbf{w}_{\omega^*}$, are summarized in Table 1, with the corresponding training loss illustrated in Fig. 10. Notably, during training, the iCANN autonomously identifies the components of the first Maxwell element, ${}^1\mathbf{w}_{\omega^*}$, as a zero vector, while the second potential exhibits relative sparsity. This finding is significant as it aligns with the rheological model defined by Eqs. (40)–(41). If the weights associated with the final layer of the generalized potential are zero, it indicates that the iCANN effectively simplifies to a Constitutive Artificial Neural Network (CANN) focused solely on hyperelastic behavior. Fig. 11 presents the training and testing results for the weights identified during training. We observe good agreement between the artificial data and the model's response in both training and testing phases. The model is capable of adequately recovering the relaxation behavior, especially in the constant deformation states, e.g., from $t = 2.5$ [min] up to $t = 3.5$ [min].

Although the test results align well in the primary loading direction, $\hat{S}_{11}$, an artificial stress increase is observed in the off-axis direction, $\hat{S}_{22}$. This suggests that the discovered weights deviate from the exact solution. If they perfectly matched the artificial material model, $\hat{S}_{22}$ should vanish under uniaxial tension (Figs. 8 and 9). Instead, the discovered weights induce a constrained deformation, analogous to the difference between Young's modulus and the longitudinal modulus in elasticity theory. Whether this truly constitutes an 'issue' is debatable. If the discovered network is used to simulate a boundary value problem, the strong form of equilibrium would enforce a uniaxial stress state, albeit with a different transverse elongation.

Comparison with conventional Recurrent Neural Network. Next, we evaluate the performance of our physics-embedded iCANN framework in comparison to a baseline model. Specifically, we consider a conventional Recurrent Neural Network (RNN) that does not incorporate any physical prior — neither in its architectural design nor in the loss function. As inputs, the RNN receives the stretch tensor $\boldsymbol{C}$ and the time increment Δt at each time step. The network outputs the corresponding stress tensor

[11] Comprehensive data on weights and biases is available online.

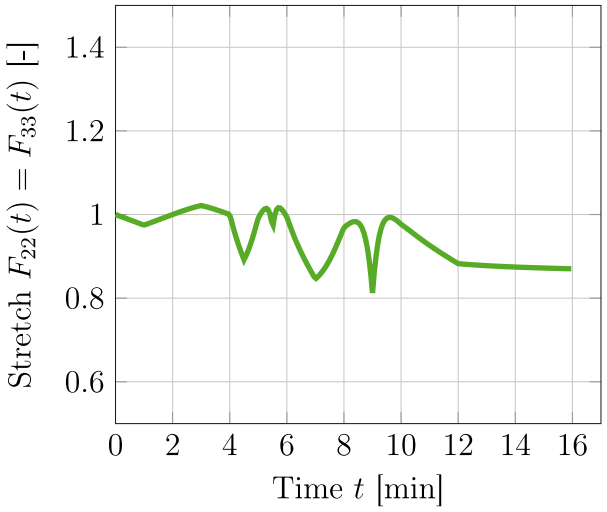

Fig. 9. Components of the deformation gradient for uniaxial loading corresponding to the Helmholtz free energy (40) and potential (41) for the first example of artificial data. The loading path in the main direction is shown in Fig. 8. The remaining shear components of the deformation gradient are equal to zero.

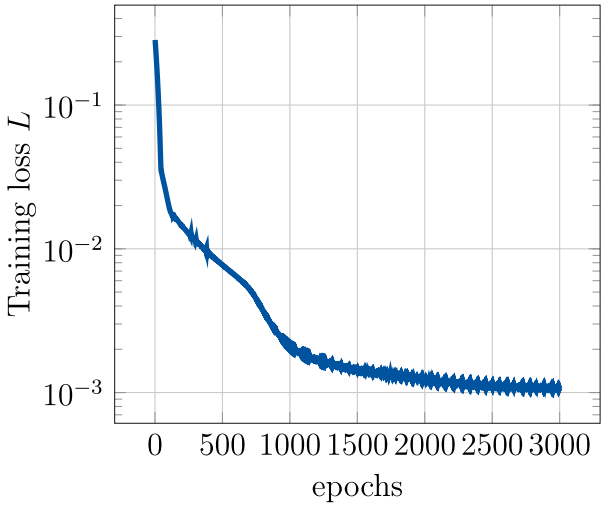

Fig. 10. Loss during training of the generalized iCANN for the first example of artificially generated data. The loss is plotted on a logarithmic scale. For training, 3000 epochs were used.

components $\boldsymbol{S}$, along with a hidden state that is propagated through time. We fix the dimensionality of the hidden state to six. A detailed description of the RNN architecture is provided in Appendix A.2.

The training and testing results of the baseline RNN are displayed in the middle panel of Fig. 11. While the RNN successfully captures the training data, its performance deteriorates significantly in the testing regime. Notably, the model fails to predict the correct peak stress values and exhibits unphysical behavior. For example, although the stretch monotonically increases between $t = 8$ and $t = 9$ [min], the predicted stress by the RNN decreases — clearly violating expected physical trends.

We conclude that our iCANN outperforms the physics-agnostic baseline in terms of generalization and physical consistency. However, it is important to emphasize that this does not imply the iCANN's stress predictions are universally accurate without further validation.

Implicit discovery. Up to now, we have determined the network's weights and biases using an explicit exponential integrator scheme. However, implicit time integration schemes are more commonly employed in computational mechanics due to their superior stability and robustness.

To investigate this, we trained the implicit version of the generalized iCANN using the same data set. The results, shown in Fig. 12, reveal that both weight vectors, ${}^1\mathbf{w}_{\omega^*} = {}^2\mathbf{w}_{\omega^*} = \mathbf{0}$, reduce to the zero vector. This implies that the iCANN collapses entirely into

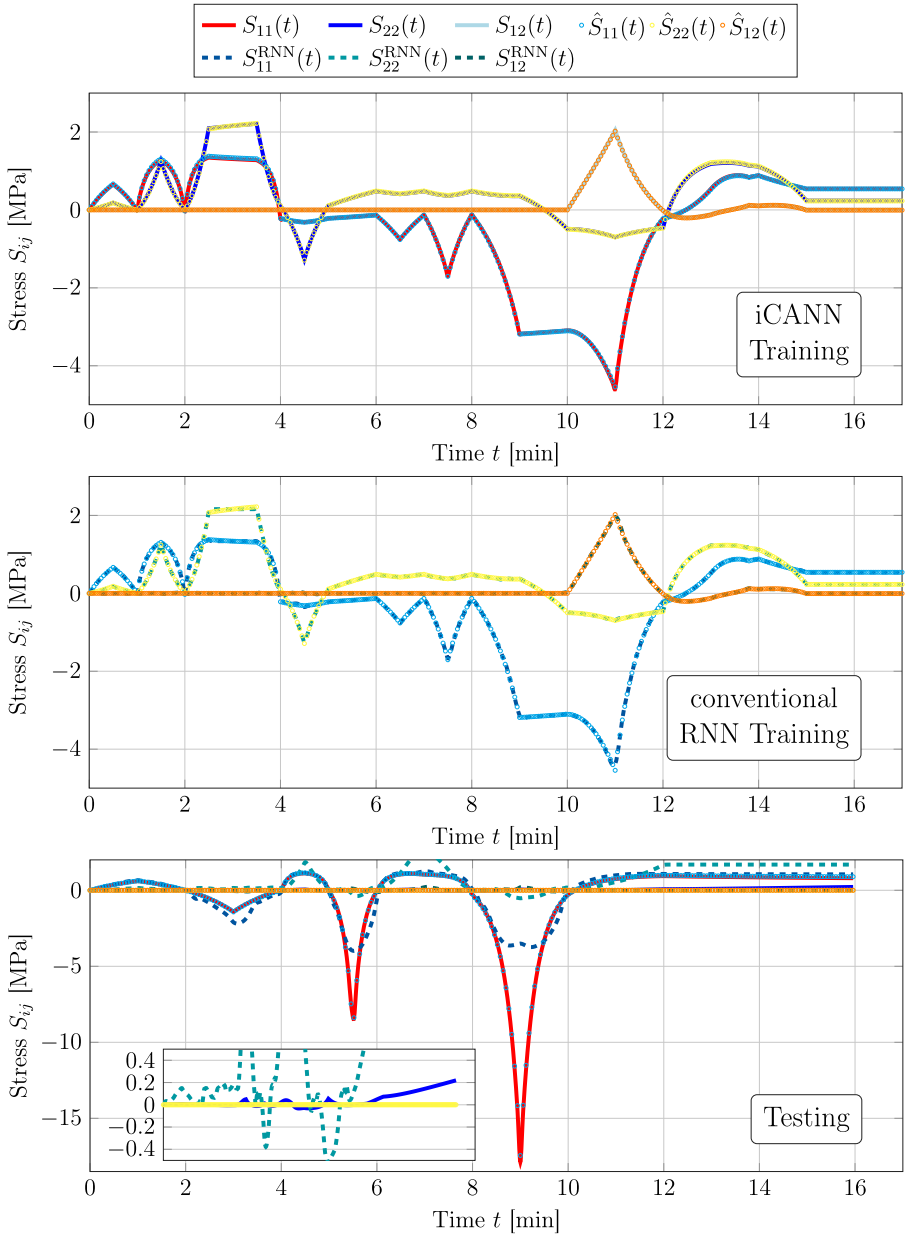

Fig. 11. Discovered model for the first example of artificially generated data. The predicted stress components are plotted against the artificially generated data, $\hat{S}_{ij}$. Top: iCANN training results, S_{ij}, for the discovered weights of multiaxial loading. Middle: Conventional RNN training results, S_{ij}^{RNN}, for the discovered weights of multiaxial loading. Bottom: Testing results for uniaxial tension. The zoomed window shows stresses over the entire load path up to $t = 16$ [min].

a CANN, rendering it incapable of representing inelastic material behavior. Consequently, we observe a strong discrepancy in the training results.

To further analyze this behavior, we evaluate the implicit network using the weights obtained from the explicit scheme (see Fig. 11). Up to $t = 7.35$ [min], the results align well with the training data. However, beyond this point, the local Broyden iteration fails to converge. This suggests that greater attention must be given to developing a stable and robust iterative solving technique, though this is beyond the scope of this study. Nevertheless, Section 5 provides a more detailed discussion on the implementation of the implicit integration scheme.

Table 1
First example of artificially generated data. Listed are the components of the weight vector, $\mathbf{w}_{\omega^*}$, for the generalized iCANN shown in Fig. 7. The first four weights correspond to the maximum activation function, while the latter four correspond to the exponential activation.

	1	2	3	4	5	6	7	8
${}^1\mathbf{w}_{\omega^*}$	0	0	0	0	0	0	0	0
${}^2\mathbf{w}_{\omega^*}$	0	0.2103749	0	0	0	0	0	0

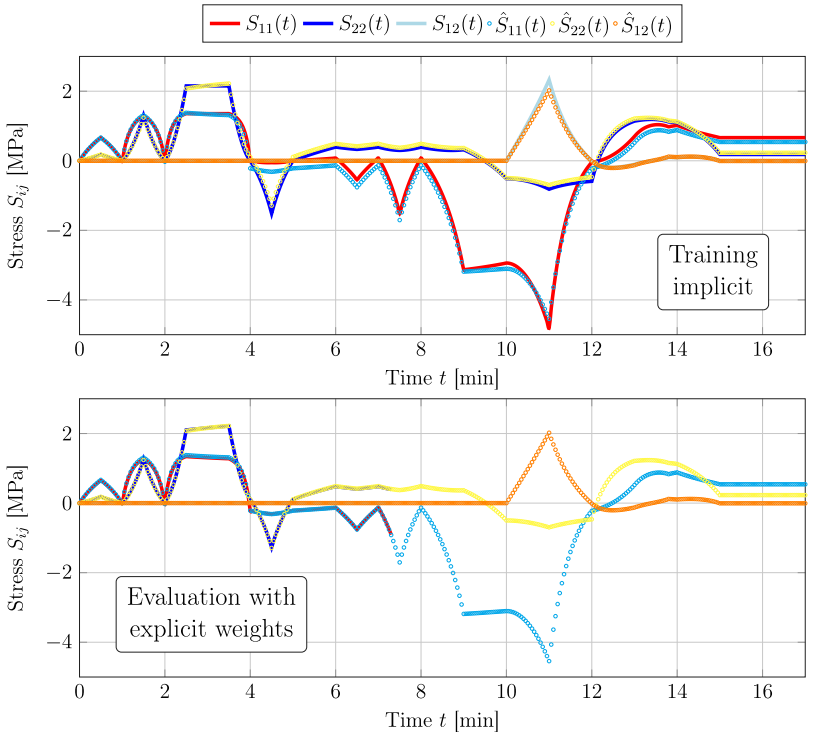

Fig. 12. Implicit discovery. Above: Discovered model for the first example of artificially generated data with an implicit time integration scheme. The network's weights for the generalized dual potential, ${}^1\mathbf{w}_{\omega^*}$ and ${}^2\mathbf{w}_{\omega^*}$, turn out to be the zero vector. Thus, the network behaves as a purely elastic network (CANN). Below: Predicted stresses for the generalized iCANN with implicit time integration but employing the discovered weights and biases of the explicit architecture (cf. Fig. 11). The local iteration aborts after $t = 7.35$ [min].

4.1.2. Discovering a model for artificial data: Example 2

We proceed by evaluating the performance of the generalized iCANN using a different constitutive model. For the Helmholtz free energy, we stick to the very same energy (40) as in the first example, however, we exchange the potential (41) by a quadratic form, i.e.,

$$\omega^* = K_1 \left(2\, J_2^{\bar{\Sigma}}\right) + K_2 \left(I_2^{\bar{\Sigma}}\right)^2 \tag{42}$$

with $\mu = 25$ [MPa], $\kappa = 50$ [MPa], $K_1 = 4 \cdot 10^{-5}$ [1/MPa], and $K_2 = 7.2 \cdot 10^{-4}$ [1/MPa]. The shear modulus, μ, as well as the bulk modulus, κ, are also used to determine the Helmholtz free energy (40). As in the first example, the constitutive model represents a Maxwell and a 'spring' element connected in parallel. However, contrary to the first example, the choice of material parameters yields a small amount of energy dissipation compared to the elastic response of the 'spring'. To create artificial data sets for training and testing, we subject the constitutive model (Eqs. (40) and (42)) to the loadings described in Fig. 8. The remaining components of the deformation gradient to achieve a state of uniaxial tension are shown in Fig. 13.

Discovery. For the chosen material parameters, the training stresses exceed 100 [MPa], causing the iteration to abort. To address this, we normalize the artificial data by the absolute maximum stress value, $S^{\max} = 125.1517$ [MPa], as is common in neural network training.

Fig. 14 presents the training results. As in the first example, the entire load path up to $t = 17$ [min], consisting of 341 data points, is used for training. Once again, the iCANN autonomously identifies that the weights of one Maxwell element vanish while the other retain nonzero values. However, the predicted stresses exhibit poor agreement with the artificial data, particularly in capturing the relaxation behavior.

This discrepancy raises the question of its origin. Given that the same complex loading path is used, the issue is unlikely due to insufficient data richness. A potential bottleneck, particularly for inelastic materials, may be the initialization of the weights.

Staggered discovery. To investigate our assumption regarding initialization, we vary the batch size used for training, i.e., we do not utilize the full data set at once. Instead, we start with a smaller subset of the 341 data points.

Although varying the batch size is a common practice in neural network training and can be applied to CANNs, inelastic materials require special treatment. Due to the strong sequential dependency imposed by the time integration scheme, randomly selecting data points is not feasible. Instead, each training batch must consist of a continuous sequence of data points. Furthermore, even when using sequential subsets, the initial values of the internal states remain unknown. Consequently, every batch must begin at the very start of the entire load path to ensure consistency in training.

In this contribution, we introduce a staggered discovery scheme, where training begins with a small subset of data points. The subset is then incrementally expanded while initializing each new training phase with the discovered weights from the previous step. This process is repeated until the entire load path is used for training. For the current study, we employ three subsets: 70 data points, 170 data points, and 240 data points. The training losses for all sessions are plotted in Fig. 15, while the discovered weights of the last layer of the generalized potential are listed in Table 2. Fig. 16 presents both the training and testing results.

It is noteworthy that the staggered discovery scheme yields better agreement with the artificial data, particularly in capturing the relaxation behavior, compared to the initial approach (cf. Fig. 14). Once again, the iCANN autonomously identifies the viscoelastic nature of the data, as one iCANN reduces to a CANN network. Although the potential is explicitly incorporated into the proposed network architecture, some discrepancies remain, indicating that the network has not yet discovered the optimal solution. Interestingly, despite the inclusion of the quadratic potential, the discovered weights in Table 2 reveal that only the weights associated with the exponential activation function are nonzero.

During testing, the predicted responses align well with the artificial data for most of the loading path, except at the second peak stress. This discrepancy may be attributed to the exponential activation function, which grows rapidly with increasing stress. Consequently, its incorrect influence may manifest only at high stress levels and was likely negligible during training. As in the first example, an artificial increase in off-axis stresses is observed throughout the testing session. The underlying cause of this phenomenon is similar to the explanation provided in Section 4.1.2.

In this study, we did not adjust hyperparameters such as the number of layers, neurons, or activation functions, nor did we refine weight initialization. These factors may influence our findings (see Section 5 for further discussion).

Discover noisy data. So far, we have considered 'clean' data generated deterministically from the constitutive model. However, real measurement data often contain noise. To evaluate the stability of our chosen regularization technique against overfitting, we introduce white Gaussian noise into our training data. We apply the staggered discovery scheme once again. The training results are presented in Fig. 17, while losses are plotted in Fig. 15. Table 2 lists the weights discovered in the last layer of the generalized iCANN. The discovered model aligns well with the noisy data, showing no signs of overfitting; additionally, its qualitative response resembles that without noise. Notably, the same neuron is activated. However, it can be assumed that stress predictions may diverge from artificial data for higher stress peaks due to greater variability in inelastic stretch evolution.

Comparison of different regularization strategies. Thus far, we have employed L_1 regularization to promote sparsity, aiming for interpretable and compact network architectures. However, beyond potential limitations in expressivity, one may question whether interpretability remains critical — especially since the model is already constrained such that only physically admissible behavior can be discovered, which is our primary goal.

To explore this, we revisited the dataset (cf. Fig. 14) under two alternative settings: (i) no regularization and (ii) L_2 regularization. In case of the latter, L_2 penalties of 0.0001 were applied to all weights and biases in the dual potential and 0.001 to the energy network weights.

The corresponding weights of the final layer of the dual potential are listed in Table 2, and training and testing results are shown in Fig. 18. With L_2 regularization, one Maxwell element effectively reduces to a CANN, yet overall performance is inferior to the sparsity-based model. No staggered training was used in any setting.

Notably, the unregularized model outperforms both regularized variants, achieving better training accuracy and closer agreement with experimental stress data. Surprisingly, none of the Maxwell elements reduce to a CANN. In a *standard* Maxwell model, this would imply fluid-like behavior. However, a relaxation test (Fig. 19) reveals a stress plateau rather than decay, indicating solid-like response.

This can be explained by the iCANN architecture: unlike classical formulations, it allows for a zero interval in the dual potential, leading to zero derivative (i.e., no viscoelastic response) until a 'threshold' stress is reached, see the right of Fig. 19. Thus, viscoelastic effects emerge only beyond this threshold. We comment on the implications of this behavior in the next section.

4.2. Discovering a model for the experimental data of VHB 4910 polymer

In this final example, we investigate the generalized iCANN's ability to model experimentally measured data. We utilize experimental data from very-high-bond (VHB) 4910 polymer published by Hossain et al. (2012), which has previously been used to assess the original iCANN formulation (Holthusen et al., 2024a) and has been compared with other constitutive neural network approaches (Abdolazizi et al., 2024) as well as a classical constitutive model (Hossain et al., 2012). In these comparisons, the iCANN demonstrated strong performance and effectively predicted outside the training regime. Thus, this example also facilitates a comparison between our newly proposed iCANN and existing methodologies.

Table 2
Second example of artificially generated data. Listed are the components of the weight vector, $\mathbf{w}_{\omega^*}$, for the generalized iCANN shown in Fig. 7. The first four weights correspond to the maximum activation function, while the latter four correspond to the exponential activation. Both the weights for the clean data set (see Fig. 16) and the noisy data set (see Fig. 17) are shown. In addition, the weights for the comparison between regularization techniques – both without regularization and L_2 regularization – are listed (see Fig. 18).

		1	2	3	4	5	6	7	8
Clean	${}^1\mathbf{w}_{\omega^*}$	0	0	0	0	0.00452437	0	0	0
	${}^2\mathbf{w}_{\omega^*}$	0	0	0	0	0	0	0	0
Noisy	${}^1\mathbf{w}_{\omega^*}$	0	0	0	0	0.086715	0	0	0
	${}^2\mathbf{w}_{\omega^*}$	0	0	0	0	0	0	0	0
No regularization	${}^1\mathbf{w}_{\omega^*}$	0.01524587	0.01438581	0.02298172	0.02187982	0.01962221	0.01970891	0.01715593	0.01683176
	${}^2\mathbf{w}_{\omega^*}$	0.09149758	0.10079461	0.09022211	0.09294859	0.08184145	0.08089893	0.07856774	0.08012391
L_2 regularization	${}^1\mathbf{w}_{\omega^*}$	2.0197620e−13	2.5699806e−13	9.8215957e−14	8.9305570e−14	2.0364191e−13	4.5474741e−13	7.0148396e−13	7.1516122e−13
	${}^2\mathbf{w}_{\omega^*}$	0.00965801	0.00929589	0.0092021	0.01092725	0.21808127	0.24579608	0.27070275	0.2567871

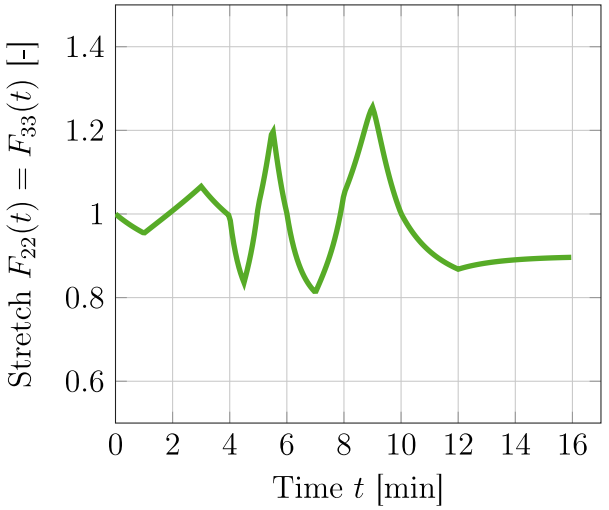

Fig. 13. Components of the deformation gradient for uniaxial loading corresponding to the Helmholtz free energy (40) and potential (42) for the second example of artificial data. The loading path in the main direction is shown in Fig. 8. The remaining shear components of the deformation gradient are equal to zero.

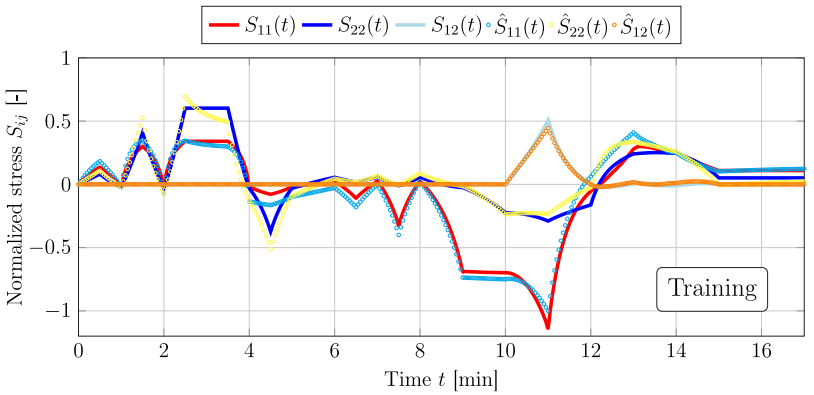

Fig. 14. Full data discovery. Discovered model for the second example of artificially generated data. The predicted stress components, S_{ij}, are plotted against the normalized artificially generated data, $\hat{S}_{ij}$. The data are normalized by $S^{\max} = 125.1517$ [MPa]. The entire load path, consisting of 341 data points, is used simultaneously for training.

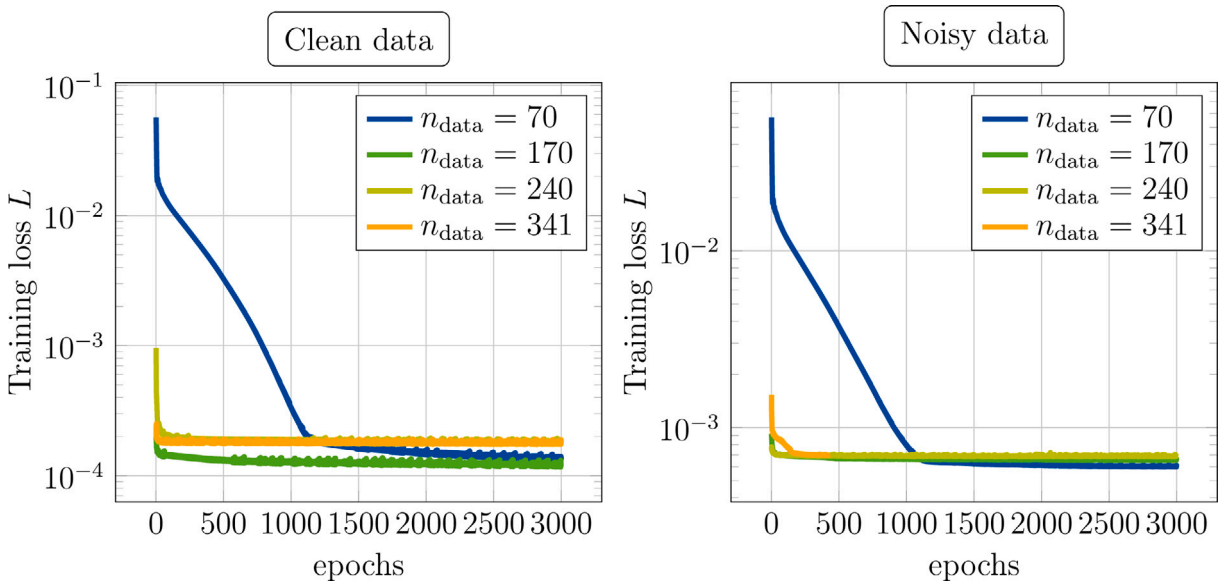

Fig. 15. Losses during training of the generalized iCANN for the second example of artificially generated data. The losses are plotted on a logarithmic scale. For training, 3000 epochs were used. A staggered discovery scheme is employed, i.e., the data points used for training are gradually increased. Left: Losses for the 'clean' data set, see Fig. 16. Right: Losses for the 'noisy' data set, see Fig. 17.

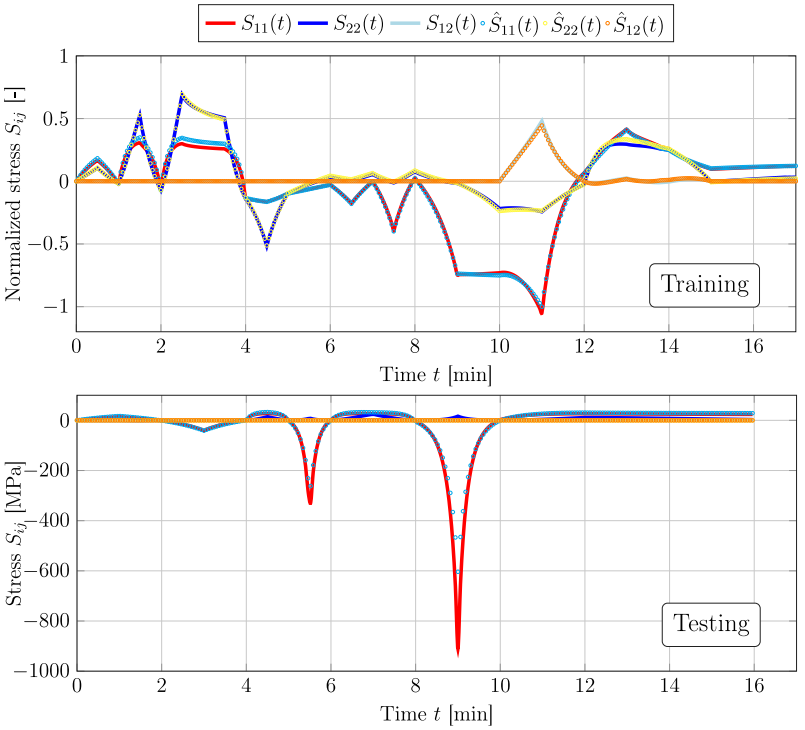

Fig. 16. Staggered discovery with clean data. Discovered model for the second example of artificially generated data. The predicted stress components, S_{ij}, are plotted against the artificially generated data, $\hat{S}_{ij}$. Above: Training results for the discovered weights of multiaxial loading. The stresses are normalized by $S^{\max} = 125.1517$ [MPa]. Below: Testing results for uniaxial tension. The stresses are not normalized.

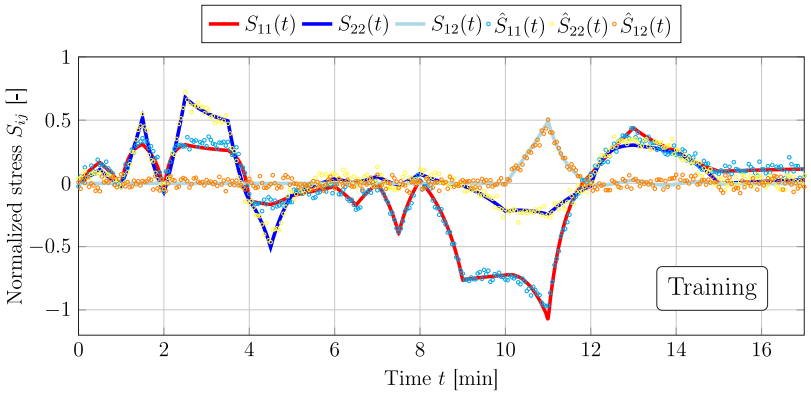

Fig. 17. Staggered discovery with noisy data. Discovered model for the second example of artificially generated data. The predicted stress components, S_{ij}, are plotted against the artificially generated data, $\hat{S}_{ij}$. White Gaussian noise is added to the data shown in Fig. 16.

The polymer is subjected to constant uniaxial loading followed by uniaxial unloading at three distinct but constant rates. Several experiments were conducted with varying maximum stretch levels, specifically $C_{11}^{\max} \in \{2.25, 4.0, 6.25, 9.0\}$ [–]. Notably, no experimental data is provided for a deformation rate of 0.03 [1/s] at the maximum stretch level applied. In contrast to our previous examples, the time increment in this case is not constant, and we normalize the stress data to its maximum value of $S^{\max} = 27.988124$ [kPa].

The data is one-dimensional; thus, no information on transverse elongation is provided. This results in an undetermined problem, leading us to assume incompressibility in line with prior studies (Holthusen et al., 2024a,b; Abdolazizi et al., 2024). For details on implementing incompressibility, interested readers are referred to the original iCANN work (Holthusen et al., 2024a).

Discovery: Training A. We begin with the same training setup as in Holthusen et al. (2024a), utilizing only the data for $C_{11}^{\max} = 9.0$ [–] for training. The corresponding loss during training is depicted in Fig. 20, while the weights of the last layer of the potential are presented in Table 3. Notably, we do not use the deformation rate of 0.03 [1/s] for training, leaving this rate unseen by the network. Furthermore, for the experimental data, the iCANN autonomously discovers visco-elasticity by reducing one iCANN to a CANN architecture, resulting in zero weights.

In contrast to identifying material parameters for classical constitutive models (Hossain et al., 2012), we omit multi-step relaxation data from the training. Our training and testing results are shown in Fig. 21. While there is good agreement during training, the model does not perform well on testing data; few predictions match well, e.g., for $C_{11}^{\max} = 4.0$ [–] with a constant deformation rate of 0.05, while most do not.

A plausible explanation has been provided by Abdolazizi et al. (2024): The experimental data exhibit inconsistencies; for identical loading rates but different maximum stretch levels, the loading paths should align, which is not observed (see Holthusen et al., 2024a). Consequently, a neural network based on constitutive equations – including our generalized iCANN – struggles to predict such stress curves.

Despite our new proposed iCANN performing well during training, it is less accurate compared to previous works (Hossain et al., 2012; Abdolazizi et al., 2024) and particularly when compared to the original iCANN (Holthusen et al., 2024a). This may seem surprising at first, as the original architecture is included within the new one.

However, while the original architecture consists of only nine weights per Maxwell element for the feed-forward network of the potential, our new architecture employs 316 weights (see Section 3.1.2). Thus, it is not surprising that one-dimensional data may lack sufficient complexity to accurately determine all network weights. Considering Shannon's information theory (Shannon, 1948) alongside our results from artificially generated data sets with richer information could provide insight into this issue (see also Section 5).

Lastly, we note that four Maxwell elements were used in the original iCANN architecture to adequately recover stress responses and that it was initialized with a 'spring' (CANN) element. In contrast, our newly proposed architecture autonomously reduces complexity and requires only a single Maxwell element within the generalized iCANN framework to accurately recover stress responses during training.

Discovery: Training B. The results from Training A indicate the need for additional data to enhance model discovery. Therefore, we incorporate not only the data for $C_{11}^{\max} = 9.0$ [–] but also that for $C_{11}^{\max} = 4.0$ [–], including all three deformation rates in the training process.

The loss is illustrated in Fig. 20, and the discovered weights are detailed in Table 3. Once again, the iCANN autonomously identifies the underlying mechanisms of visco-elasticity by reducing one iCANN to a CANN. Our training and testing results are presented in Fig. 22.

Although performance improves within the training regime due to this richer dataset compared to Fig. 21, predictions outside this regime remain poor relative to earlier studies. While qualitative stress responses may be recovered, quantitative curves do not

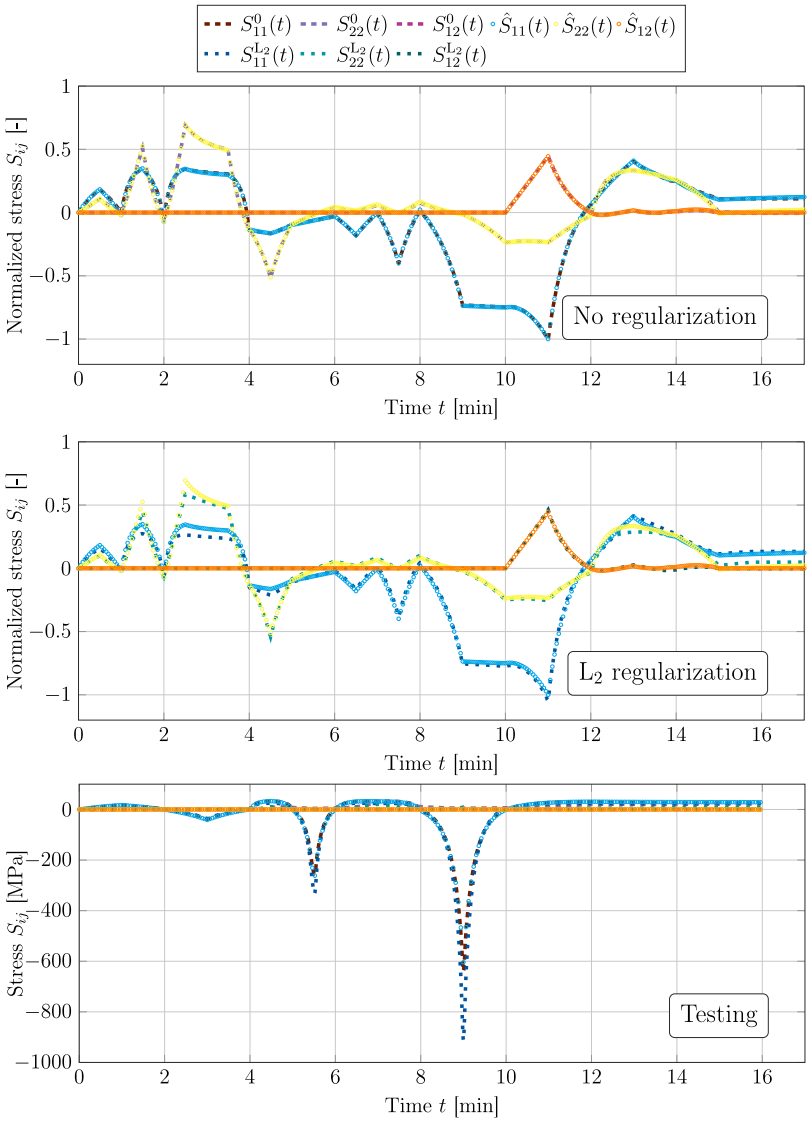

Fig. 18. Full data discovery with different regularization strategies. Comparison of different regularization strategies for full-data discovery in the second artificially generated dataset. Top: Model trained without any regularization. Middle: Model trained with L_2 regularization applied to all weights and biases. Bottom: Testing results for both cases, showing that the unregularized model achieves superior predictive accuracy and better agreement with the target stress data.

align well. The iCANN continues to struggle with insufficiently 'rich' data for accurately determining weights and biases relevant to the material under investigation.

As previously noted, stresses should ideally match for identical deformation rates. Consequently, the additional data from $C_{11}^{\max} = 4.0$ [–] primarily introduces previously unseen deformation rates and unloading curves. Whether this sufficiently enhances the richness of one-dimensional data for discovering numerous weights remains questionable (see also Section 5).

5. Discussion and current limitations

The results from the previous section demonstrated that the proposed iCANN architecture, whose complexity can be recursively increased along the lines of classical feed-forward networks, successfully discovers visco-elasticity at finite strains, and further, automatically uncovers the inelastic phenomenon hidden in the data. However, as with any approach that is still in its early stages, we faced some challenges during the discovery process, took some further steps towards effective discovery of inelastic materials, and were left with some unanswered questions, which we would like to share in the following.

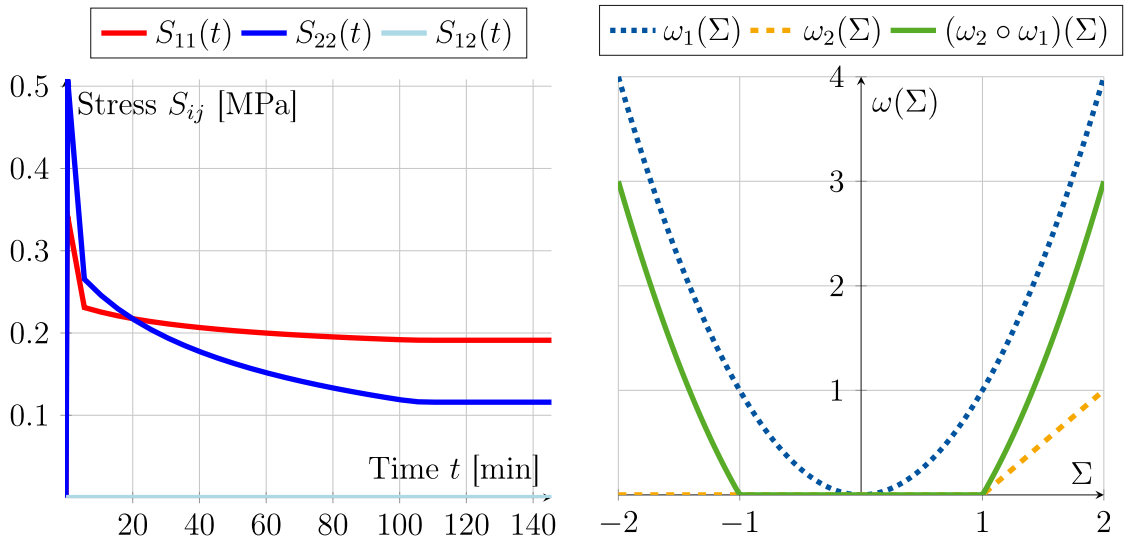

Fig. 19. Relaxation behavior without regularization. Left: Relaxation behavior for the discovered model trained without any regularization, see Fig. 18. The model is subjected to uniaxial relaxation, i.e., $\boldsymbol{F} = \boldsymbol{I}$ and F_{11} is linearly increased over time up to $F_{11} = 1.8$ within eleven time steps and $\Delta t = 0.05$ [min]. Both S_{11} and S_{22} reach a stress plateau. Right: A possible explanation for the visco-elastic behavior of the Maxwell element. The architecture of a hypothetical dual potential (depicted in green) illustrates visco-elastic behavior: its derivative vanishes below $\Sigma = 1$, with $\omega_1 = \Sigma^2$ and $\omega_2 = \max(\Sigma - 1, 0)$.

Table 3
Experimental data of VHB 4910 polymer (Hossain et al., 2012). Listed are the components of the weight vector, $\mathbf{w}_{\omega^*}$, for the generalized iCANN shown in Fig. 7. The first four weights correspond to the maximum activation function, while the latter four correspond to the exponential activation. Both the weights for the training session A (see Fig. 21) and training session B (see Fig. 22) are shown.

		1	2	3	4	5	6	7	8
Training A	${}^1\mathbf{w}_{\omega^*}$	0	0	0	0	0.19749504	0	0	0
	${}^2\mathbf{w}_{\omega^*}$	0	0	0	0	0	0	0	0
Training B	${}^1\mathbf{w}_{\omega^*}$	0	0	0	0	0.09977169	0	0	0
	${}^2\mathbf{w}_{\omega^*}$	0	0	0	0	0	0	0	0

Time integration scheme. Our findings highlight challenges in the integration scheme. Training with an implicit scheme led to an undesired convergence of the weights of the potential towards zero. Based on Section 4.1.1, we attribute this to inaccuracies in the iterative solver rather than the implicit integration itself.[12] Broyden's method seems to be inadequate for solving the nonlinear evolution equation, requiring numerous local iterations (see Appendix A.3), which complicates neural network backpropagation.

Initially, we employed Newton's method, but automatic differentiation of the residual (17) to get its Jacobian introduced issues in the backpropagation, prompting us to switch to the derivative-free Broyden method.

In this context, an intriguing approach has been proposed in the literature. Instead of directly integrating the evolution equation, As'ad and Farhat (2023b) replaced the iterative solution of the ordinary differential equations with a feed-forward neural network. Building upon this idea, Rosenkranz et al. (2024) later introduced a recurrent architecture employing a LSTM cell to address the challenge of time integration and to compute the internal variables — specifically in the framework of Generalized Standard Materials. Their studies indicate that computational time during training can be significantly reduced compared to the iterative solution of the discretized evolution equation.

Further research is needed on combining neural network training with efficient iterative solvers to ensure stable training. The implicit function theorem, applied to the residual to calculate the derivative of the inelastic stretch with respect to the network's weights, may enhance stability. However, our studies show that explicit integration is computationally more efficient, though smaller time steps are required. In real-world experiments, the step size can usually be controlled.

Relation to Input Convex Networks. We briefly relate our architecture of the dual potential to input convex neural networks (ICNNs) (Amos et al., 2017). The authors distinguish between *fully* and *partially* input convex networks, focusing on the former.

[12] Although the code has been carefully reviewed, implementation errors are still possible. We encourage interested readers to scrutinize the implementation, which is available online.

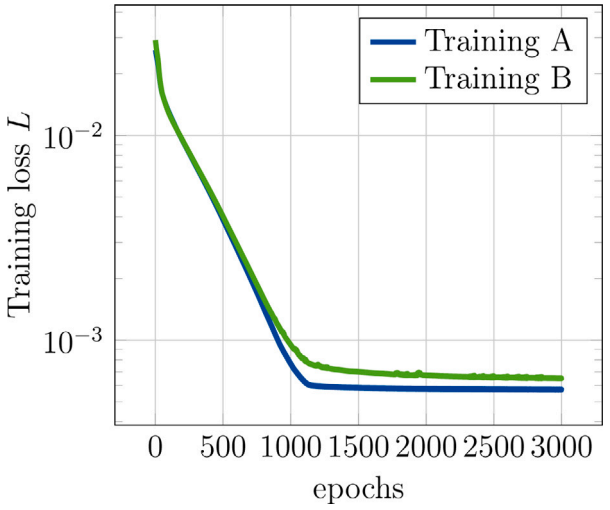

Fig. 20. Losses during training of the generalized iCANN for the experimental data of VHB 4910 polymer (Hossain et al., 2012). The losses are plotted on a logarithmic scale. For training, 3000 epochs were used. Two distinct training sessions are conducted: Training A (see Fig. 21), which utilizes a smaller data set, and Training B (see Fig. 22), which employs a larger data set.

Fully input convex networks evolve as $\mathbf{x}_{k+1} = f^{k+1}(\mathbf{W}_k^{k+1}\mathbf{x}_k + \mathbf{V}^{k+1}\mathbf{x}_0 + \mathbf{b}^{k+1})$, where $\mathbf{W}$ is constrained to be non-negative, $\mathbf{V}$ and $\mathbf{b}$ are unconstrained, and f^{k+1} is convex and non-decreasing.

Our architecture shares structural similarities but introduces important differences. Specifically, we enforce zero-valued outputs and non-negativity of the dual potential. To this end, we constrain all activation functions to vanish at zero and add an additional layer $(K + 1)$ to impose non-negativity. Bias terms are omitted to preserve a zero-valued potential at the origin, except for the maximum activation, where they are constrained to be non-positive.

We allow real-valued weights from the input to the first hidden layer and use several activations per layer, representing an alternative to the connections via $\mathbf{V}$. Moreover, we admit convex but *decreasing* activations, at least in the first hidden layer. While the ICNN architecture of Amos et al. (2017) is more canonical and uniform across layers, it could be adapted to enforce the additional constraints required in our setting. In contrast, our design is motivated by classical dual potentials in mechanics. A systematic comparison between the two approaches is currently absent and would be valuable to clarify their relative advantages and limitations. While a combination of both approaches could potentially offer additional flexibility or improved performance, such exploration is beyond the scope of the present work.

Regularization. We employed elastic net regularization on the weights connecting the input layer to the first hidden layer to balance sparsity and stability, while applying lasso regularization specifically to the final output layer. This choice is motivated by empirical evidence from Constitutive Artificial Neural Networks (CANNs) (McCulloch et al., 2024), where sparsity in the output layer has been associated with improved model interpretability. Although the regularization strategy for the final layer remains heuristic to some extent, it is guided by the rationale that promoting sparsity facilitates the identification of dominant terms, thereby enhancing interpretability. In particular, this enables a clearer connection between the learned representations and known rheological models, as demonstrated in our numerical examples. The overarching objective of this work was to prioritize interpretability over maximal expressive power, aiming to uncover physically meaningful structures rather than solely optimizing predictive performance.

The use of elastic net is also primarily heuristic; however, it has demonstrated effective results and – at least in our experience – enhanced stability during training. It is important to note that heuristic strategies may not represent the optimal solution. The question of whether a superior regularization method exists for every inelastic phenomenon warrants further investigation.

Additionally, in Section 4.1.2, we compared our regularization-based approach with a model trained without any regularization. The unregularized model demonstrated overall better performance — both during training and testing — compared to the regularized counterpart. However, as mentioned in that section, this improvement comes at the cost of interpretability, at least from a *classical* mechanics perspective, where different inelastic phenomena can often be linked to specific rheological elements. Several years ago, when artificial intelligence began gaining traction within the mechanics community, a central question emerged: Should one favor purely data-driven models or those that embed physical priors, even if they are potentially less flexible? We observe a resurgence of a similar dilemma here — this time framed as a trade-off between interpretability and expressivity, albeit under the condition that both modeling approaches satisfy physics *a priori*. This contribution has primarily focused on interpretability and does not attempt to resolve this trade-off. Rather, it represents one of many efforts beginning to explore and reframe this question.

In contrast to the Helmholtz free energy, we allow the potential to be zero. A zero energy implies no stresses would arise, which contradicts experimental data. A zero potential, on the other hand, leads to a hyperelastic model that could find an 'optimal solution' for monotonic loading with constant stretch rates at different maximum stretch levels applied to the same material.

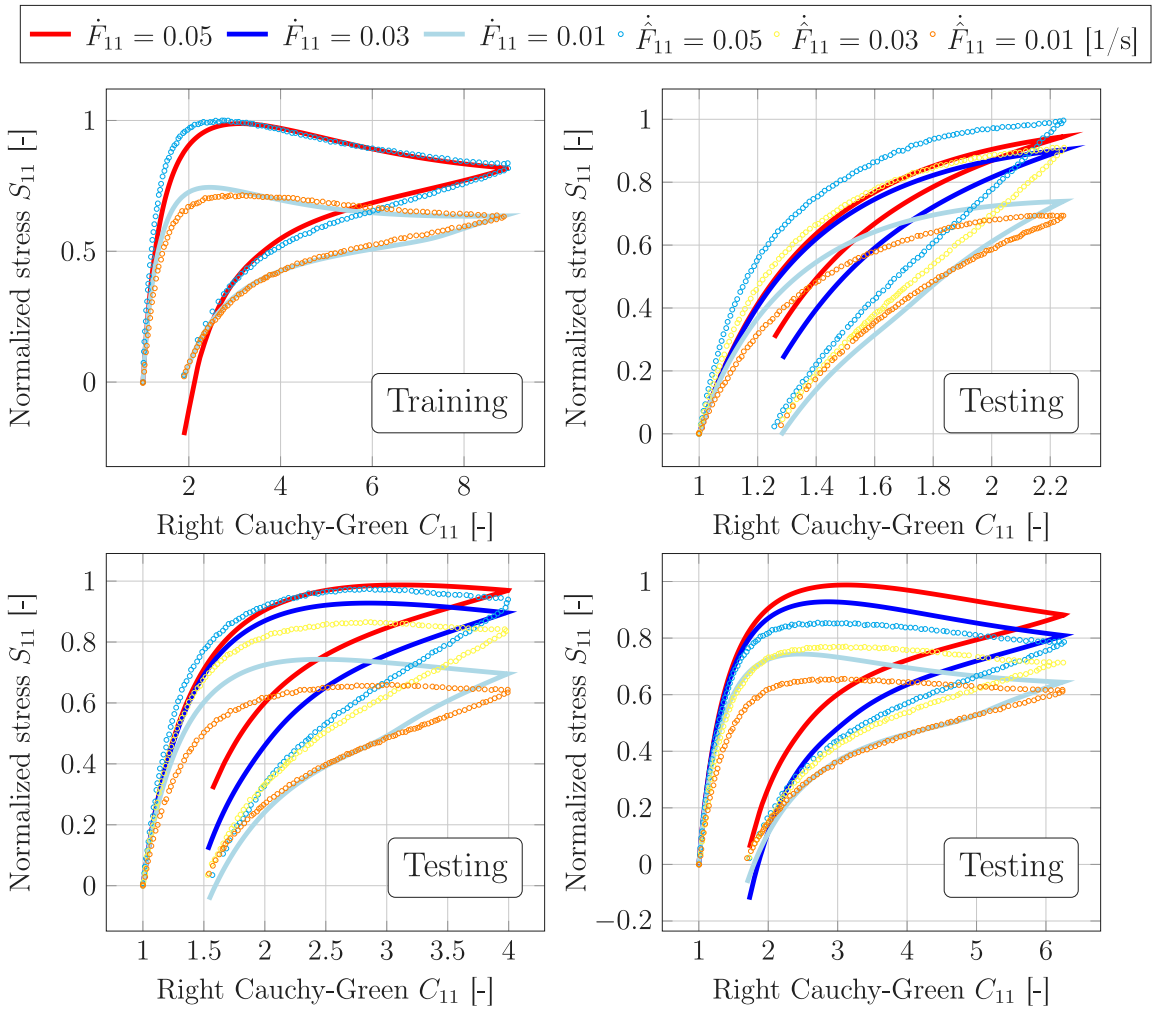

Fig. 21. Training A. Discovered model for the experimental data of VHB 4910 polymer (Hossain et al., 2012) employing three different constant loading/unloading rates, denoted as $\dot{F}_{11}$, for training. The experimentally measured data is represented by $\hat{\dot{F}}_{11}$. Stresses are normalized by $S^{\max} = 27.988124$ [kPa]. Only the experimental data corresponding to $C_{11}^{\max} = 9.0$ [–] are utilized for training.

Interestingly, our chosen regularization approach resulted in sparse networks and appeared capable of identifying the degree of inelasticity within the data. Earlier training sessions conducted without regularization on the feed-forward network produced dense networks – none of which reduced from iCANNs to CANNs, thereby failing to accurately represent visco-elastic solids.

Initialization. We initialized the network weights using a uniform distribution, $U(a, b)$, with heuristically determined bounds

$$\mathbf{W}_0^{\mathrm{I}} \sim U(-1, 1), \quad \mathbf{W}_{\mathrm{I}}^{\mathrm{II}}, \mathbf{W}_{\mathrm{II}}^{\mathrm{III}} \sim U(0, 0.01), \quad \mathbf{w}_{\omega^*} \sim U(0, 0.001), \quad p_1, p_2 \sim U(0, 1) \tag{43}$$

Biases were initialized to zero to prevent symmetry-breaking effects.

Our training results indicate that performance is highly dependent on the amount of data used (see Section 4.1.2). When the data set is too large in combination with a low degree of inelasticity, the information entropy may become insufficient for discovering the optimal potential. Since we have not systematically explored alternative initialization bounds, we cannot exclude the possibility that different choices might enhance the network's ability to generalize across the full data set.

Furthermore, in our experience, the ratio between the weights of energy and potential plays a crucial role. If energy weights are too large, the potential rapidly tends towards infinity regardless of its own weights. To the best of our understanding, these large energy weights lead to disproportionately high values of the thermodynamic driving force $\bar{\boldsymbol{\Sigma}}$. Given the use of, e.g., an exponential activation function in the potential, this can cause the potential to diverge or 'explode'. As a consequence, the derivatives of the potential with respect to $\boldsymbol{\Sigma}$ may become undefined or numerically unstable (e.g., NaN or infinite), ultimately disrupting the training process. In addition, the exponential integrator may lead to an unbounded growth of $\bar{\boldsymbol{D}}_i$ even for finite (albeit possibly large) values of $\bar{\boldsymbol{\Sigma}}$. To mitigate this behavior, we employed gradient clipping (see below), which proved partially effective. Nonetheless,

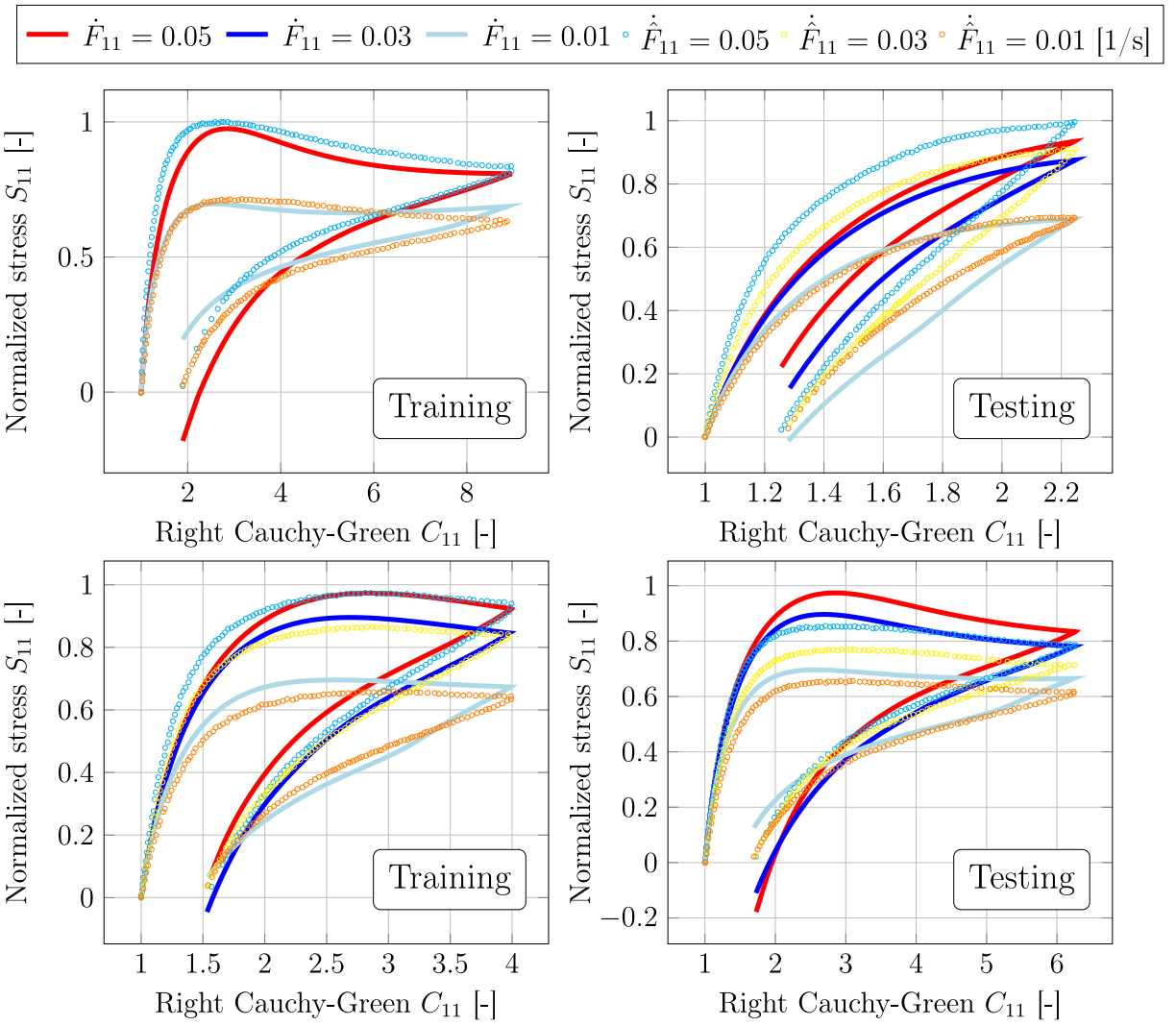

Fig. 22. Training B. Discovered model for the experimental data of VHB 4910 polymer (Hossain et al., 2012) employing three different constant loading/unloading rates, denoted as $\dot{F}_{11}$, for training. The experimentally measured data is represented by $\dot{\hat{F}}_{11}$. Stresses are normalized by $S^{\max} = 27.988124$ [kPa]. The experimental data corresponding to $C_{11}^{\max} = 9.0$ and $C_{11}^{\max} = 4.0$ [–] are utilized for training.

we acknowledge that this solution is not fully satisfactory, and further improvements remain possible — particularly through more robust architectural choices or tailored regularization strategies.

Conversely, if energy weights are too small, the potential may be significantly underestimated, leading to an overly elastic response. In extreme cases, the model may learn a purely elastic behavior that simply balances the data set rather than capturing the underlying material response. More technically, the training process may converge to an elastic minimum of the loss function, i.e., a solution where the network primarily represents elastic behavior. This outcome is highly sensitive to the choice and strength of regularization. In particular, under strong L_1 regularization, the optimal trade-off — purely from a loss minimization perspective — may favor suppressing the inelastic contributions entirely. That is, setting the weights associated with the dual potential to zero can yield a lower overall loss than representing the true underlying inelastic behavior, due to the additive penalty imposed by the regularization term. This highlights a potential bias introduced by sparsity-promoting regularization and emphasizes the importance of carefully balancing data fidelity and model complexity. However, a more detailed investigation of this phenomenon lies beyond the scope of the present contribution.

Given the significant impact of weight initialization on learning dynamics, we recognize the need for systematic investigation. An evolutionary optimization approach, such as a genetic algorithm, could provide an effective strategy for weight distributions and mitigating undesirable energy-to-potential ratios.

Hyperparameters. Across all examples, we employed the same set of hyperparameters, including learning rate, regularization parameters, number of hidden layers, number of neurons per activation function, choice of activation functions, and the clipping

norm for gradient clipping. While some of these define the network architecture itself, such as depth and width, others regulate the training process.

Notably, model performance is influenced not only by the number of neurons, which likely correlates with the number of hidden layers, but also by training-specific parameters such as the clipping norm. The interplay among these factors renders hyperparameter selection a highly nonlinear optimization problem.

We observed that gradient clipping is essential for stabilizing the inelastic potential. Similar to weight initialization, where an improper energy-to-potential ratio can lead to an unbounded potential, the absence of gradient clipping can cause excessive growth of the potential's weights between epochs, ultimately leading to divergence.

The chosen hyperparameters yielded satisfactory results for the examples considered in this study. However, we acknowledge that this may be due to a fortuitous selection of parameters and the specific network complexity in terms of depth and neuron count.

For artificial data, the training procedure performed well, producing results consistent with the data set. In contrast, performance deteriorated when applied to experimentally obtained data. This discrepancy may stem from the network's complexity, which introduces unnecessary flexibility in the learned weights. Furthermore, the information content of artificial and experimental data sets likely differs significantly.

Across all examples, the final state of training consistently produced a sparse weight vector $\mathbf{w}_{\omega^*}$. Whether performance could be further improved through systematic hyperparameter tuning and reduced network complexity remains an open question.

We anticipate that hyperparameter optimization will be particularly critical for modeling more complex inelastic phenomena such as plasticity and damage. Fortunately, hyperparameter optimization is an extensively studied problem in the neural network community. Established techniques such as reinforcement learning (Wu et al., 2020), grid search (Bergstra et al., 2011), genetic algorithms (Sun et al., 2019), and gradient-based optimization (Pedregosa, 2016) offer promising strategies. Recently, agent-based hyperparameter optimization (Esmaeili et al., 2023) has shown the potential to outperform these established techniques and may also serve as a valuable tool in physics-embedded neural networks. For a comprehensive overview, we refer the reader to Bischl et al. (2023).

Richness of data sets. Ultimately, the key question underlying our discussion is: How 'rich' is the data? If the information entropy is sufficiently high, the iCANN architecture is likely capable of uncovering the inelastic phenomena hidden in the data and of accurately identifying the underlying potential governing the material's response. However, the concept of 'richness' in the context of material science requires further clarification.

Consider a previously discussed example: Suppose we conduct a series of uniaxial tension experiments on a visco-elastic solid, varying only the maximum stretch level while keeping the deformation rate constant across all tests. Despite the large number of data points, the information entropy remains low. Consequently, the network will most likely identify a purely hyperelastic response. In contrast, if the deformation rate is also varied, the observed stress differences between experiments can only be attributed to the presence of an inelastic potential.

We encountered this issue with the VHB 4910 polymer (see Section 4.2). While the network accurately reproduced the training data, its predictive performance was poor. This suggests that the 'richness' of uniaxial tension data alone was insufficient to capture an accurate material model given the chosen network's complexity. To illustrate this further, we consider an experiment in which a material undergoes hydrostatic relaxation, ensuring that no shear stresses arise. Since the second and third stress invariants remain zero throughout the experiment, the network would be unable to infer any material dependence on these invariants.

These challenges align with long-standing questions in experimental mechanics. Traditionally, experiments are designed to isolate specific material parameters, such as relaxation time in relaxation tests. However, the combination of neural networks and advanced optimization techniques – both in training and hyperparameter tuning – may enable us to replace numerous experiments with a single, highly complex experiment that captures comprehensive material behavior.

This raises an important question: How to uniquely design a 'rich' experimental setup that captures not only elasticity and visco-elasticity but also phenomena such as plasticity, damage, and even multiphysics interactions? We assume that leveraging structural discovery in complex boundary value problems will be instrumental in achieving this goal, as demonstrated by EUCLID (Flaschel et al., 2022).

6. Conclusion

We took a further step towards the understanding and discovery of general inelasticity at finite strains through a rigorous mathematical formulation that ensures a convex, non-negative, and zero-valued potential. This enabled the design of a scalable, interpretable network architecture akin to traditional feed-forward networks, encompassing various classical potentials in continuum mechanics. Our thermodynamically consistent approach inherently satisfies the dissipation inequality, ensuring predictions beyond training remain aligned with fundamental physical principles.

We introduced a regularization scheme inspired by Constitutive Artificial Neural Networks (CANNs), employing lasso and ridge techniques for sparse representation. This allowed the iCANN to autonomously determine the degree of inelasticity and reducing to a purely elastic CANN when appropriate. Gradient clipping prevented excessive weight growth in the potential network, avoiding unbounded stress responses and training instabilities.

Our studies successfully discovered multiple constitutive material models with high accuracy. A staggered discovery scheme prevented potential network weights from collapsing to zero when inelastic dissipation was low in the training data. The combination of our network architecture and regularization framework enabled stable identification of visco-elastic behavior, even with noisy data.

However, we encountered several limitations. The implicit time integration scheme was unstable when using Broyden's method to iteratively solve the evolution equation. Critically, while our network accurately captured training data for an experimentally measured polymer, it failed to predict accurately beyond the training regime, despite exploring various data set sizes. We attribute this to insufficient data richness, consistent with our findings for artificial data sets.

Balancing network complexity and data richness is a key challenge for meaningful weight discovery. The success of neural networks in approximating material behaviors hinges on sufficiently informative experimental data. This underscores the need for collaboration between experimental mechanics and computational modeling to design new experimental setups and discovery strategies. Future experiments may aim to maximize information content while minimizing test specimens and addressing uncertainties in material properties.

For our approach, this implies extending the network architecture to boundary value problems, leveraging displacement field information to enhance material discovery.

CRediT authorship contribution statement

Hagen Holthusen: Writing – review & editing, Writing – original draft, Visualization, Validation, Software, Methodology, Investigation, Funding acquisition, Formal analysis, Data curation, Conceptualization. **Kevin Linka:** Writing – review & editing, Writing – original draft, Methodology, Funding acquisition. **Ellen Kuhl:** Writing – review & editing, Writing – original draft, Methodology, Funding acquisition. **Tim Brepols:** Writing – review & editing, Writing – original draft, Methodology, Funding acquisition.

Code availability

Our source code and examples of the iCANN implementation in `JAX` are accessible to the public at https://doi.org/10.5281/zenodo.14894687.

Declaration of Generative AI and AI-assisted technologies in the writing process

This document was prepared with the assistance of OpenAI's ChatGPT, an AI language model. ChatGPT was used for language refinement. The authors reviewed, edited, and take full responsibility for the content and conclusions of this work.

Declaration of competing interest

The authors declare that they have no known competing financial interests or personal relationships that could have appeared to influence the work reported in this paper.

Acknowledgments

Hagen Holthusen and Tim Brepols gratefully acknowledge financial support of the projects 417002380 and 453596084 by the Deutsche Forschungsgemeinschaft. In addition, Kevin Linka is supported by the Emmy Noether Grant 533187597 by the Deutsche Forschungsgemeinschaft. This work was supported by the NSF CMMI Award 2320933 Automated Model Discovery for Soft Matter and by the ERC Grant 101141626 DISCOVER to Ellen Kuhl.

Appendix

A.1. Proof of thermodynamic consistency

We begin by showing that thermodynamic consistency is guaranteed if the dual potential $\omega(\boldsymbol{\Sigma})$ is convex, zero-valued at the origin, and non-negative with respect to the thermodynamic force $\boldsymbol{\Sigma}$. For simplicity, we restrict ourselves to the case where ω is continuously differentiable and omit the more general case involving subdifferentials. The interested reader is referred to Germain (1998) and the literature cited therein for a detailed treatment of that case.

To demonstrate consistency, it suffices to show that $\boldsymbol{\Sigma} : \boldsymbol{D}_i \geq 0$. Exploiting the convexity of ω, we obtain the general inequality

$$\omega(\mathbf{0}) \geq \omega(\boldsymbol{\Sigma}) - \frac{\partial \omega}{\partial \boldsymbol{\Sigma}} : \boldsymbol{\Sigma}. \tag{A.1}$$

Since ω is zero-valued at the origin, i.e., $\omega(\mathbf{0}) = 0$, this inequality simplifies to

$$\frac{\partial \omega}{\partial \boldsymbol{\Sigma}} : \boldsymbol{\Sigma} \geq \omega(\boldsymbol{\Sigma}). \tag{A.2}$$

Furthermore, combining this with the evolution Equation (4) and the non-negativity of $\omega(\boldsymbol{\Sigma}) \geq 0$, we find

$$\boldsymbol{\Sigma} : \boldsymbol{D}_i \geq \omega(\boldsymbol{\Sigma}) \geq 0, \tag{A.3}$$

which proves that the second law of thermodynamics is satisfied if $\omega(\boldsymbol{\Sigma})$ is convex, zero-valued, and non-negative with respect to $\boldsymbol{\Sigma}$. However, these are merely *sufficient*, not *necessary*, conditions, as we will see below.

Next, we are interested in whether the invariants I_1, $\sqrt{J_2}$, and $\sqrt[3]{J_3}$ are already convex with respect to $\boldsymbol{\Sigma}$. To assess this, we examine whether the second Gâteaux derivative, $\mathcal{D}^2 f[\boldsymbol{H},\boldsymbol{H}]$, of the invariants is non-negative for all $\boldsymbol{H} \in \mathbb{R}^{3\times3}_{\text{sym}}$, which is a necessary and sufficient condition for convexity.

We begin with the first invariant I_1

$$\begin{aligned}\mathcal{D}^2 I_1(\boldsymbol{\Sigma})[\boldsymbol{H},\boldsymbol{H}] &= \frac{\mathrm{d}}{\mathrm{d}\epsilon}\left[DI_1(\boldsymbol{\Sigma}+\epsilon\,\boldsymbol{H})[\boldsymbol{H}]\right]\Big|_{\epsilon=0} \\ &= \frac{\mathrm{d}}{\mathrm{d}\epsilon}\left[\mathrm{tr}(\boldsymbol{H})\right]|_{\epsilon=0} = 0,\end{aligned} \tag{A.4}$$

which proves that the first invariant is an affine — and thus convex — function of the thermodynamic driving force.

We now investigate the convexity of the second invariant J_2 with respect to the stress tensor $\boldsymbol{\Sigma}$. Recall that $J_2(\boldsymbol{\Sigma}) = \frac{1}{2}\boldsymbol{\Sigma}' : \boldsymbol{\Sigma}'$, where $\boldsymbol{A}' := \boldsymbol{A} - \frac{1}{3}\,\mathrm{tr}(\boldsymbol{A})\,\boldsymbol{I}$ denotes the deviatoric part of a tensor. To prove convexity, we examine the second Gâteaux derivative $\mathcal{D}^2 J_2(\boldsymbol{\Sigma})[\boldsymbol{H},\boldsymbol{H}]$ for all directions $\boldsymbol{H} \in \mathbb{R}^{3\times3}_{\text{sym}}$.

First, we compute the first derivative

$$\mathcal{D}J_2(\boldsymbol{\Sigma})[\boldsymbol{H}] = \frac{1}{2}\,\frac{\mathrm{d}}{\mathrm{d}\epsilon}\left[\mathrm{tr}\left((\boldsymbol{\Sigma}'+\epsilon\boldsymbol{H}')^2\right)\right]\Big|_{\epsilon=0} = \boldsymbol{\Sigma}' : \boldsymbol{H}' = \boldsymbol{\Sigma}' : \boldsymbol{H}. \tag{A.5}$$

Then, taking the second Gâteaux derivative, we obtain

$$\mathcal{D}^2 J_2(\boldsymbol{\Sigma})[\boldsymbol{H},\boldsymbol{H}] = \boldsymbol{H}' : \boldsymbol{H}' = \mathrm{tr}\left(\boldsymbol{H}'^2\right). \tag{A.6}$$

This expression is non-negative for all symmetric $\boldsymbol{H}$, since it is a scalar product of a tensor with itself. Hence,

$$\mathcal{D}^2 J_2(\boldsymbol{\Sigma})[\boldsymbol{H},\boldsymbol{H}] \geq 0 \quad \forall \boldsymbol{H} \in \mathbb{R}^{3\times3}_{\text{sym}}, \tag{A.7}$$

which proves that $J_2(\boldsymbol{\Sigma})$ is a convex function with respect to $\boldsymbol{\Sigma}$. Although we have shown that $J_2(\boldsymbol{\Sigma})$ is convex with respect to $\boldsymbol{\Sigma}$, we now examine whether the function $\sqrt{J_2(\boldsymbol{\Sigma})}$ is also convex. To this end, we compute the first and second Gâteaux derivatives

$$\mathcal{D}\sqrt{J_2(\boldsymbol{\Sigma})}[\boldsymbol{H}] = \frac{\mathrm{d}}{\mathrm{d}\epsilon}\left[\sqrt{J_2(\boldsymbol{\Sigma}+\epsilon\,\boldsymbol{H})}\right]\Big|_{\epsilon=0} = \frac{\boldsymbol{\Sigma}' : \boldsymbol{H}'}{\sqrt{2\,\boldsymbol{\Sigma}' : \boldsymbol{\Sigma}'}} \tag{A.8}$$

$$\mathcal{D}^2\sqrt{J_2(\boldsymbol{\Sigma})}[\boldsymbol{H},\boldsymbol{H}] = \frac{\mathrm{d}}{\mathrm{d}\epsilon}\left[\frac{(\boldsymbol{\Sigma}'+\epsilon\,\boldsymbol{H}') : \boldsymbol{H}'}{\sqrt{2\,(\boldsymbol{\Sigma}'+\epsilon\,\boldsymbol{H}') : (\boldsymbol{\Sigma}'+\epsilon\,\boldsymbol{H}')}}\right]\Bigg|_{\epsilon=0} = \frac{(\boldsymbol{H}' : \boldsymbol{H}')(\boldsymbol{\Sigma}' : \boldsymbol{\Sigma}') - (\boldsymbol{\Sigma}' : \boldsymbol{H}')^2}{\sqrt{2}\sqrt{(\boldsymbol{\Sigma}' : \boldsymbol{\Sigma}')^3}} \tag{A.9}$$

which is convex since the denominator in the latter is always positive for $\boldsymbol{\Sigma}' \neq \boldsymbol{0}$ and the nominator is positive according to the Cauchy–Schwarz inequality. Note that this is in line with the well-known property that the *von Mises* yield surface is convex with respect to the stress.

It remains to investigate the convexity of the third invariant J_3 with respect to the stress tensor $\boldsymbol{\Sigma}$. The third invariant of the deviatoric stress is given by

$$J_3(\boldsymbol{\Sigma}) = \frac{1}{3}\,\mathrm{tr}(\boldsymbol{\Sigma}'^3). \tag{A.10}$$

Again, we compute the second Gâteaux derivative $\mathcal{D}^2 J_3(\boldsymbol{\Sigma})[\boldsymbol{H},\boldsymbol{H}]$ for all directions $\boldsymbol{H} \in \mathbb{R}^{3\times3}_{\text{sym}}$.

First, the first derivative reads

$$\mathcal{D}J_3(\boldsymbol{\Sigma})[\boldsymbol{H}] = \mathrm{tr}\left(\boldsymbol{\Sigma}'^2\boldsymbol{H}'\right) = \left(\boldsymbol{\Sigma}'^2\right)' : \boldsymbol{H}, \tag{A.11}$$

and the second Gâteaux derivative becomes

$$\mathcal{D}^2 J_3(\boldsymbol{\Sigma})[\boldsymbol{H},\boldsymbol{H}] = 2\,\mathrm{tr}\left(\boldsymbol{\Sigma}'\boldsymbol{H}'\boldsymbol{H}'\right) = 2\,\boldsymbol{\Sigma}' : \boldsymbol{H}'^2. \tag{A.12}$$

Unlike in the case of J_2, this expression is not guaranteed to be non-negative for all $\boldsymbol{H}$; it can be positive, negative, or zero depending on $\boldsymbol{\Sigma}'$. Therefore, $J_3(\boldsymbol{\Sigma})$ is *not convex*. Also, taking the cubic root does not restore convexity, as the following counterexample demonstrates. Let

$$\boldsymbol{\Sigma}_1 = \begin{pmatrix}1 & 0 & 0\\ 0 & 0 & 0\\ 0 & 0 & -1\end{pmatrix}, \quad \boldsymbol{\Sigma}_2 = \begin{pmatrix}2 & 1 & 0\\ 1 & 2 & 0\\ 0 & 0 & 1\end{pmatrix}. \tag{A.13}$$

Then, their average is

$$\boldsymbol{\Sigma}_m = \tfrac{1}{2}(\boldsymbol{\Sigma}_1 + \boldsymbol{\Sigma}_2) = \begin{pmatrix}1.5 & 0.5 & 0\\ 0.5 & 1.0 & 0\\ 0 & 0 & 0\end{pmatrix}. \tag{A.14}$$

Computing the deviatoric parts and evaluating the third invariant, we find

$$\sqrt[3]{J_3(\boldsymbol{\Sigma}_1)} = 0, \quad \sqrt[3]{J_3(\boldsymbol{\Sigma}_2)} = \frac{2\cdot 2^{1/3}}{3}, \quad \sqrt[3]{J_3(\boldsymbol{\Sigma}_m)} = \frac{5^{2/3}}{6}. \tag{A.15}$$

Hence,

$$\sqrt[3]{J_3(\boldsymbol{\Sigma}_m)} > \tfrac{1}{2}\sqrt[3]{J_3(\boldsymbol{\Sigma}_1)} + \tfrac{1}{2}\sqrt[3]{J_3(\boldsymbol{\Sigma}_2)} = \frac{2^{1/3}}{3}, \tag{A.16}$$

which violates the convexity condition. Accordingly, we cannot guarantee the thermodynamic consistency of the dual potential ω^* as this is not necessarily convex with respect to $\boldsymbol{\Sigma}$.

However, as mentioned earlier, convexity with respect to $\boldsymbol{\Sigma}$ is a *sufficient* but not a *necessary* condition for thermodynamic consistency. With the derivatives of the invariants at hand, we obtain

$$\frac{\partial I_1}{\partial \boldsymbol{\Sigma}} = \boldsymbol{I}, \qquad \frac{\partial I_1}{\partial \boldsymbol{\Sigma}} : \boldsymbol{\Sigma} \quad = I_1, \tag{A.17}$$

$$\frac{\partial \sqrt{J_2}}{\partial \boldsymbol{\Sigma}} = \frac{1}{2\sqrt{J_2}}\,\boldsymbol{\Sigma}', \qquad \frac{\partial \sqrt{J_2}}{\partial \boldsymbol{\Sigma}} : \boldsymbol{\Sigma} = \sqrt{J_2}, \tag{A.18}$$

$$\frac{\partial \sqrt[3]{J_3}}{\partial \boldsymbol{\Sigma}} = \frac{1}{3\sqrt[3]{J_3^2}}\left(\boldsymbol{\Sigma}'^2\right)', \qquad \frac{\partial \sqrt[3]{J_3}}{\partial \boldsymbol{\Sigma}} : \boldsymbol{\Sigma} = \sqrt[3]{J_3}, \tag{A.19}$$

which yields the reduced dissipation inequality, in accordance with Eq. (5), as

$$\boldsymbol{\Sigma} : \boldsymbol{D}_i = \boldsymbol{\Sigma} : \frac{\partial \omega^*}{\partial \boldsymbol{\Sigma}} = \frac{\partial \omega^*}{\partial I_1} I_1 + \frac{\partial \omega^*}{\partial \sqrt{J_2}}\sqrt{J_2} + \frac{\partial \omega^*}{\partial \sqrt[3]{J_3}}\sqrt[3]{J_3}. \tag{A.20}$$

In shorthand notation (cf. Eq. (6)), this can be written as $\boldsymbol{\Sigma} : \boldsymbol{D}_i = \nabla\omega^*(\mathbf{z}) \cdot \mathbf{z}$. Thus, in analogy to Eqs. (A.1)–(A.3), we find that

$$\boldsymbol{\Sigma} : \boldsymbol{D}_i = \frac{\partial \omega^*}{\partial \mathbf{z}} \cdot \mathbf{z} \geq \omega^*(\mathbf{z}) \geq 0 \tag{A.21}$$

is satisfied if ω^* is convex, zero-valued, and non-negative with respect to the invariants. Accordingly, thermodynamic consistency is ensured as long as the dual potential is constructed in such a way that these requirements with respect to the invariants are fulfilled, though not necessarily with respect to $\boldsymbol{\Sigma}$.

Notably, this directly extends to the co-rotated quantities $\bar{\boldsymbol{\Sigma}}$ and $\bar{\boldsymbol{D}}_i$, which are related to their intermediate counterparts as $\bar{\boldsymbol{D}}_i = \boldsymbol{R}_i^{-1}\boldsymbol{D}_i\boldsymbol{R}_i$ and $\bar{\boldsymbol{\Sigma}} = \boldsymbol{R}_i^{-1}\boldsymbol{\Sigma}_i\boldsymbol{R}_i$. Consequently, each of these intermediate tensors shares the same invariants as their co-rotated equivalents. Moreover, the scalar product is preserved under this transformation, i.e., $\boldsymbol{\Sigma} : \boldsymbol{D}_i = \bar{\boldsymbol{\Sigma}} : \bar{\boldsymbol{D}}_i$.

A.2. Architecture of conventional recurrent neural network

The recurrent neural network (RNN) architecture employed in this work is based on a custom recurrent cell that integrates multiple fully connected layers with nonlinear activations. It represents a multilayer extension of a simple Elman recurrent neural network (Elman, 1990). At each time step t, the input vector $\mathbf{x}_t \in \mathbb{R}^{d_{\text{in}}}$ is concatenated with the previous hidden state $\mathbf{h}_{t-1} \in \mathbb{R}^{d_s}$ to form the combined input

$$\mathbf{z}_0 = \begin{bmatrix} \mathbf{x}_t \\ \mathbf{h}_{t-1} \end{bmatrix} \in \mathbb{R}^{d_{\text{in}}+d_s}. \tag{A.22}$$

This vector is sequentially passed through L fully connected layers of dimensions $d_1, \dots, d_L$, each followed by a nonlinear activation function f_ℓ, resulting in the transformation

$$\mathbf{z}_\ell = f_\ell\left(\mathbf{W}_\ell \mathbf{z}_{\ell-1} + \mathbf{b}_\ell\right), \quad \ell = 1, \dots, L, \tag{A.23}$$

where $\mathbf{W}_\ell \in \mathbb{R}^{d_\ell \times d_{\ell-1}}$ and $\mathbf{b}_\ell \in \mathbb{R}^{d_\ell}$ denote the weight matrix and bias vector of the ℓth layer, respectively, and $d_0 = d_{\text{in}} + d_s$. The output of the last hidden layer, $\mathbf{z}_L$, is then linearly projected to the hidden state dimension via

$$\mathbf{h}_t = \mathbf{W}_{\text{out}}\mathbf{z}_L + \mathbf{b}_{\text{out}}, \quad \mathbf{W}_{\text{out}} \in \mathbb{R}^{d_s \times d_L}, \quad \mathbf{b}_{\text{out}} \in \mathbb{R}^{d_s}. \tag{A.24}$$

The overall sequence model applies this recurrent cell iteratively over an input sequence $\mathbf{X} = (\mathbf{x}_1, \dots, \mathbf{x}_T) \in \mathbb{R}^{T \times d_{\text{in}}}$, initializing the hidden state with zeros, i.e.,

$$\mathbf{h}_0 = \mathbf{0}. \tag{A.25}$$

At each time step, the hidden state is updated according to Eq. (A.24) producing a sequence of hidden states $(\mathbf{h}_1, \dots, \mathbf{h}_T) \in \mathbb{R}^{T \times d_s}$. The final output at each time step is computed by applying a shared output layer to the hidden states:

$$\mathbf{y}_t = \mathbf{W}_y\mathbf{h}_t + \mathbf{b}_y, \quad \mathbf{W}_y \in \mathbb{R}^{d_{\text{out}} \times d_s}, \quad \mathbf{b}_y \in \mathbb{R}^{d_{\text{out}}}. \tag{A.26}$$

The full output sequence is thus given by

$$\mathbf{Y} = (\mathbf{y}_1, \dots, \mathbf{y}_T) \in \mathbb{R}^{T \times d_{\text{out}}}. \tag{A.27}$$

In the implementation used in this study, the hidden part of the recurrent cell consists of $L = 4$ fully connected layers, each with $d_\ell = 64$ units and ReLU activation functions, i.e.,

$$f_\ell(x) = \max(x, 0), \quad \forall \ell. \tag{A.28}$$

The input vector, $\mathbf{x}_t$, consists of the current time increment and the current right Cauchy–Green tensor, and thus, $d_{\text{in}} = 7$, while we choose the number of hidden state variable in accordance with the iCANN to be $d_S = 6$. The output vector, $\mathbf{y}_t$, contains the values of the second Piola–Kirchhoff stress tensor with $d_{\text{out}} = 6$. All components are implemented in `JAX` using the `Flax` neural network library.

A.3. Broyden's method

Algorithm 1 presents Broyden's method (Broyden, 1965) to iteratively solve for the inelastic stretch, $\boldsymbol{U}_{i_t}$, in a derivative-free manner. To directly compute the inverse of the Jacobian, $\mathbf{B}$, the Sherman–Morrison formula (Sherman and Morrison, 1950) is exploited.

Algorithm 1 Broyden's method to determine $\boldsymbol{U}_{i_t}$ in Voigt's notation $(\bullet)'$

Input: tolerance ϵ, weights $\mathbf{W}$, biases $\mathbf{b}$, Δt_t, $\boldsymbol{C}_t$, $\boldsymbol{U}_{i_{t-1}}$
Output: $\boldsymbol{U}_{i_t}$
Set $\boldsymbol{U}_i'^{(0)} \leftarrow \boldsymbol{U}'_{i_{t-1}}$
Initialize residual, $\mathbf{r}^{(0)}$, according to Eq. (17) in Voigt's notation
Set $\mathbf{B} \leftarrow \mathbf{I}_{6\times 6}$
for $m = 1$ to 50 **do**
  $\mathbf{s} \leftarrow -\mathbf{B}\,\mathbf{r}^{(m-1)}$
  $\boldsymbol{U}_i'^{(m)} \leftarrow \boldsymbol{U}_i'^{(m-1)} + \mathbf{s}$
  Compute new residual, $\mathbf{r}^{(m)}$, with updated inelastic stretch $\boldsymbol{U}_i^{(m)}$
  $\mathbf{y} \leftarrow \mathbf{r}^{(m)} - \mathbf{r}^{(m-1)}$
  $\mathbf{B} \leftarrow \mathbf{B} + \frac{\mathbf{s}-\mathbf{B}\,\mathbf{y}}{\mathbf{s}^T\mathbf{B}\,\mathbf{y}}\,\mathbf{s}^T\mathbf{B}$
  if $|\mathbf{r}^{(m)}| < \epsilon$ **then**
    break
  end if
end for
return $\boldsymbol{U}_{i_t}$

A.4. Additional stress invariants

We can find a relation between the additional stress invariants $I_2^{\bar{\Sigma}}$ and $I_3^{\bar{\Sigma}}$ and our three basic invariants as follows

$$I_2^{\bar{\Sigma}} = \frac{\left(I_1^{\bar{\Sigma}}\right)^2}{6} + J_2^{\bar{\Sigma}} \tag{A.29}$$

$$I_3^{\bar{\Sigma}} = \frac{\left(I_1^{\bar{\Sigma}}\right)^3}{27} + \frac{2}{3}\,I_1^{\bar{\Sigma}}\,J_2^{\bar{\Sigma}} + J_3^{\bar{\Sigma}}. \tag{A.30}$$

While $I_2^{\bar{\Sigma}}$ is included in the general architecture, we are unable to obtain $I_3^{\bar{\Sigma}}$ since neither the activation function $(\bullet)^3$ nor the multiplication $I_1^{\bar{\Sigma}}\,J_2^{\bar{\Sigma}}$ is present in the general network architecture. We can express the dual potential as $\omega^* = \tilde{\omega}^*\left(I_1^{\bar{\Sigma}}, \sqrt{J_2^{\bar{\Sigma}}}, \sqrt[3]{J_3^{\bar{\Sigma}}}, \sqrt{I_2^{\bar{\Sigma}}(I_1^{\bar{\Sigma}}, J_2^{\bar{\Sigma}})}, \sqrt[3]{I_3^{\bar{\Sigma}}(I_1^{\bar{\Sigma}}, J_2^{\bar{\Sigma}}, J_3^{\bar{\Sigma}})}\right)$. With these relations at hand, we find

$$\frac{\partial I_2^{\bar{\Sigma}}}{\partial \bar{\boldsymbol{\Sigma}}} : \bar{\boldsymbol{\Sigma}} = 2\,I_2^{\bar{\Sigma}} \tag{A.31}$$

$$\frac{\partial I_3^{\bar{\Sigma}}}{\partial \bar{\boldsymbol{\Sigma}}} : \bar{\boldsymbol{\Sigma}} = 3\,I_3^{\bar{\Sigma}} \tag{A.32}$$

which, in analogy to Eq. (6), proves thermodynamic consistency if the specific network (Fig. 4) is convex, zero-valued, and non-negative with respect to its five inputs.

Data availability

We shared our source code and data via Zenodo.org.

References

Abdolazizi, Kian P., Aydin, Roland C., Cyron, Christian J., Linka, Kevin, 2025. Constitutive Kolmogorov-arnold networks (CKANs): Combining accuracy and interpretability in data-driven material modeling. arXiv:2502.05682. URL https://arxiv.org/abs/2502.05682.

Abdolazizi, Kian P., Linka, Kevin, Cyron, Christian J., 2024. Viscoelastic constitutive artificial neural networks (vcanns) – A framework for data-driven anisotropic nonlinear finite viscoelasticity. J. Comput. Phys. (ISSN: 0021-9991) 499, 112704. http://dx.doi.org/10.1016/j.jcp.2023.112704, URL https://www.sciencedirect.com/science/article/pii/S0021999123007994.

Amos, Brandon, Xu, Lei, Kolter, J. Zico, 2017. Input convex neural networks. In: Precup, Doina, Teh, Yee Whye (Eds.), Proceedings of the 34th International Conference on Machine Learning. In: Proceedings of Machine Learning Research, vol. 70, PMLR, pp. 146–155, URL https://proceedings.mlr.press/v70/amos17b.html.

Arghavani, J., Auricchio, F., Naghdabadi, R., Reali, A., 2011. On the robustness and efficiency of integration algorithms for a 3D finite strain phenomenological SMA constitutive model. Internat. J. Numer. Methods Engrg. 85 (1), 107–134. http://dx.doi.org/10.1002/nme.2964, arXiv:https://onlinelibrary.wiley.com/doi/pdf/10.1002/nme.2964. URL https://onlinelibrary.wiley.com/doi/abs/10.1002/nme.2964.

As'ad, Faisal, Avery, Philip, Farhat, Charbel, 2022. A mechanics-informed artificial neural network approach in data-driven constitutive modeling. Internat. J. Numer. Methods Engrg. 123 (12), 2738–2759. http://dx.doi.org/10.1002/nme.6957, arXiv:https://onlinelibrary.wiley.com/doi/pdf/10.1002/nme.6957. URL https://onlinelibrary.wiley.com/doi/abs/10.1002/nme.6957.

As'ad, Faisal, Farhat, Charbel, 2023a. A mechanics-informed deep learning framework for data-driven nonlinear viscoelasticity. Comput. Methods Appl. Mech. Engrg. (ISSN: 0045-7825) 417, 116463. http://dx.doi.org/10.1016/j.cma.2023.116463, URL https://www.sciencedirect.com/science/article/pii/S004578252300587X.

As'ad, Faisal, Farhat, Charbel, 2023b. A mechanics-informed neural network framework for data-driven nonlinear viscoelasticity. In: AIAA SCITECH 2023 Forum. American Institute of Aeronautics and Astronautics, http://dx.doi.org/10.2514/6.2023-0949.

Baek, Jonghyuk, Chen, Jiun-Shyan, 2024. A neural network-based enrichment of reproducing kernel approximation for modeling brittle fracture. Comput. Methods Appl. Mech. Engrg. (ISSN: 0045-7825) 419, 116590. http://dx.doi.org/10.1016/j.cma.2023.116590.

Baghous, Nareg, Barsoum, Imad, Al-Rub, Rashid K. Abu, 2022. The effect of lode parameter on the yield surface of schoen's iwp triply periodic minimal surface lattice. Mech. Mater. 175, 104473.

Battalgazy, Bekassyl, Khatamsaz, Danial, Ghasemi, Zahra, Mallick, Debjoy D., Arroyave, Raymundo, Srivastava, Ankit, 2025. A Bayesian-based approach for constitutive model selection and calibration using diverse material responses. Acta Mater. (ISSN: 1359-6454) 287, 120796. http://dx.doi.org/10.1016/j.actamat.2025.120796.

Bergstra, James, Bardenet, Rémi, Bengio, Yoshua, Kégl, Balázs, 2011. Algorithms for hyper-parameter optimization. Adv. Neural Inf. Process. Syst. 24.

Bessa, M.A., Bostanabad, R., Liu, Z., Hu, A., Apley, Daniel W., Brinson, C., Chen, W., Liu, Wing Kam, 2017. A framework for data-driven analysis of materials under uncertainty: Countering the curse of dimensionality. Comput. Methods Appl. Mech. Engrg. (ISSN: 0045-7825) 320, 633–667. http://dx.doi.org/10.1016/j.cma.2017.03.037, URL https://www.sciencedirect.com/science/article/pii/S0045782516314803.

Bischl, Bernd, Binder, Martin, Lang, Michel, Pielok, Tobias, Richter, Jakob, Coors, Stefan, Thomas, Janek, Ullmann, Theresa, Becker, Marc, Boulesteix, Anne-Laure, Deng, Difan, Lindauer, Marius, 2023. Hyperparameter optimization: Foundations, algorithms, best practices, and open challenges. WIREs Data Min. Knowl. Discov. 13 (2), e1484. http://dx.doi.org/10.1002/widm.1484, arXiv:https://wires.onlinelibrary.wiley.com/doi/pdf/10.1002/widm.1484. URL https://wires.onlinelibrary.wiley.com/doi/abs/10.1002/widm.1484.

Boes, Birte, Simon, Jaan-Willem, Holthusen, Hagen, 2024. Accounting for plasticity: An extension of inelastic constitutive artificial neural networks. arXiv:2407.19326. URL https://arxiv.org/abs/2407.19326.

Bradbury, James, Frostig, Roy, Hawkins, Peter, Johnson, Matthew James, Leary, Chris, Maclaurin, Dougal, Necula, George, Paszke, Adam, VanderPlas, Jake, Wanderman-Milne, Skye, Zhang, Qiao, 2018. JAX: composable transformations of python+numpy programs. URL http://github.com/jax-ml/jax.

Bresler, B., Pister, K.S., 1985. Strength of concrete under combined stresses. ACI J. (ISSN: 0020-7683) 551 (26), 321–345.

Broyden, Charles G., 1965. A class of methods for solving nonlinear simultaneous equations. Math. Comp. 19 (92), 577–593.

Chaboche, J.-L., 1997. Thermodynamic formulation of constitutive equations and application to the viscoplasticity and viscoelasticity of metals and polymers. Int. J. Solids Struct. (ISSN: 0020-7683) 34 (18), 2239–2254. http://dx.doi.org/10.1016/S0020-7683(96)00162-X, URL https://www.sciencedirect.com/science/article/pii/S002076839600162X.

Coleman, Bernard D., Gurtin, Morton E., 1967. Thermodynamics with internal state variables. J. Chem. Phys. 47 (2), 597–613. http://dx.doi.org/10.1063/1.1711937.

Coleman, Bernard D., Noll, Walter, 1961. Foundations of linear viscoelasticity. Rev. Modern Phys. 33, 239–249. http://dx.doi.org/10.1103/RevModPhys.33.239, URL https://link.aps.org/doi/10.1103/RevModPhys.33.239.

Coleman, Bernard D., Noll, Walter, 1963. The thermodynamics of elastic materials with heat conduction and viscosity. Arch. Ration. Mech. Anal. (ISSN: 1432-0673) 13 (1), 167–178. http://dx.doi.org/10.1007/BF01262690.

Collins, Jack A., 1993. Failure of Materials in Mechanical Design, second ed. John Wiley & Sons, Nashville, TN.

Collins, I.F., Kelly, P.A., 2002. A thermomechanical analysis of a family of soil models. Géotechnique (ISSN: 1751-7656) 52 (7), 507–518. http://dx.doi.org/10.1680/geot.2002.52.7.507.

Dettmer, Wulf, Reese, Stefanie, 2004. On the theoretical and numerical modelling of armstrong–frederick kinematic hardening in the finite strain regime. Comput. Methods Appl. Mech. Engrg. (ISSN: 0045-7825) 193 (1), 87–116. http://dx.doi.org/10.1016/j.cma.2003.09.005, URL http://www.sciencedirect.com/science/article/pii/S0045782503005218.

Drucker, Daniel Charles, Prager, William, 1952. Soil mechanics and plastic analysis or limit design. Quart. Appl. Math. 10 (2), 157–165.

Eckart, Carl, 1948. The thermodynamics of irreversible processes. IV. The theory of elasticity and anelasticity. Phys. Rev. 73, 373–382. http://dx.doi.org/10.1103/PhysRev.73.373, URL https://link.aps.org/doi/10.1103/PhysRev.73.373.

Eggersmann, R., Kirchdoerfer, T., Reese, S., Stainier, L., Ortiz, M., 2019. Model-free data-driven inelasticity. Comput. Methods Appl. Mech. Engrg. (ISSN: 0045-7825) 350, 81–99. http://dx.doi.org/10.1016/j.cma.2019.02.016, URL https://www.sciencedirect.com/science/article/pii/S0045782519300878.

Eghtesad, Adnan, Tan, Jingye, Fuhg, Jan Niklas, Bouklas, Nikolaos, 2024. NN-EVP: A physics informed neural network-based elasto-viscoplastic framework for predictions of grain size-aware flow response. Int. J. Plast. (ISSN: 0749-6419) 181, 104072. http://dx.doi.org/10.1016/j.ijplas.2024.104072, URL https://www.sciencedirect.com/science/article/pii/S0749641924001992.

Elman, Jeffrey L., 1990. Finding structure in time. Cogn. Sci. 14 (2), 179–211. http://dx.doi.org/10.1207/s15516709cog1402_1, arXiv:https://onlinelibrary.wiley.com/doi/pdf/10.1207/s15516709cog1402_1. URL https://onlinelibrary.wiley.com/doi/abs/10.1207/s15516709cog1402_1.

Esmaeili, Ahmad, Ghorrati, Zahra, Matson, Eric T., 2023. Agent-based collaborative random search for hyperparameter tuning and global function optimization. Systems (ISSN: 2079-8954) 11 (5), http://dx.doi.org/10.3390/systems11050228, URL https://www.mdpi.com/2079-8954/11/5/228.

Ferle, Maximilian, Grieb, Nora, Kreuz, Markus, Platzbecker, Uwe, Neumuth, Thomas, Reiche, Kristin, Oeser, Alexander, Merz, Maximilian, 2024. Predicting progression events in multiple myeloma from routine blood work. arXiv:2405.18051. URL https://arxiv.org/abs/2405.18051.

Flaschel, Moritz, Kumar, Siddhant, De Lorenzis, Laura, 2022. Discovering plasticity models without stress data. Npj Comput. Mater. (ISSN: 2057-3960) 8 (1), 91. http://dx.doi.org/10.1038/s41524-022-00752-4.

Flaschel, Moritz, Kumar, Siddhant, De Lorenzis, Laura, 2023. Automated discovery of generalized standard material models with EUCLID. Comput. Methods Appl. Mech. Engrg. (ISSN: 0045-7825) 405, 115867. http://dx.doi.org/10.1016/j.cma.2022.115867, URL https://www.sciencedirect.com/science/article/pii/S0045782522008234.

Flaschel, Moritz, Steinmann, Paul, De Lorenzis, Laura, Kuhl, Ellen, 2024. Convex neural networks learn generalized standard material models. http://dx.doi.org/10.2139/ssrn.5023581.

Fuhg, Jan N., Anantha Padmanabha, Govinda, Bouklas, Nikolaos, Bahmani, Bahador, Sun, WaiChing, Vlassis, Nikolaos N., Flaschel, Moritz, Carrara, Pietro, De Lorenzis, Laura, 2024a. A review on data-driven constitutive laws for solids. Arch. Comput. Methods Eng. (ISSN: 1886-1784) http://dx.doi.org/10.1007/s11831-024-10196-2.

Fuhg, Jan N., Jadoon, Asghar, Weeger, Oliver, Seidl, D. Thomas, Jones, Reese E., 2024b. Polyconvex neural network models of thermoelasticity. arXiv:2404.15562. URL https://arxiv.org/abs/2404.15562.

Germain, Paul, 1998. Functional concepts in continuum mechanics. Meccanica (ISSN: 1572-9648) 33 (5), 433–444. http://dx.doi.org/10.1023/A:1004304224398.

Germain, P., Nguyen, Q.S., Suquet, P., 1983. Continuum thermodynamics. J. Appl. Mech. (ISSN: 0021-8936) 50 (4b), 1010–1020. http://dx.doi.org/10.1115/1.3167184, arXiv:https://asmedigitalcollection.asme.org/appliedmechanics/article-pdf/50/4b/1010/6362862/1010_1.pdf.

Ghaboussi, J., Garrett, J.H., Wu, X., 1991. Knowledge-based modeling of material behavior with neural networks. J. Eng. Mech. (ISSN: 1943-7889) 117 (1), 132–153. http://dx.doi.org/10.1061/(asce)0733-9399(1991)117:1(132).

Ghouli, Saeid, Flaschel, Moritz, Kumar, Siddhant, Lorenzis, Laura De, 2025. A topology optimisation framework to design test specimens for one-shot identification or discovery of material models. arXiv:2501.12756. URL https://arxiv.org/abs/2501.12756.

Girardi, Ivan, Ji, Pengfei, phi Nguyen, An, Hollenstein, Nora, Ivankay, Adam, Kuhn, Lorenz, Marchiori, Chiara, Zhang, Ce, 2018. Patient risk assessment and warning symptom detection using deep attention-based neural networks. arXiv:1809.10804. URL https://arxiv.org/abs/1809.10804.

Glüge, Rainer, Bucci, Sara, 2017. Does convexity of yield surfaces in plasticity have a physical significance? Math. Mech. Solids (ISSN: 1741-3028) 23 (9), 1364–1373. http://dx.doi.org/10.1177/1081286517721599.

Halphen, Bernard, Nguyen, Quoc Son, 1975. Sur les matériaux standard généralisés. J. de Méc. 14, 39–63, URL https://hal.science/hal-00105514.

Hartmann, Stefan, Neff, Patrizio, 2003. Polyconvexity of generalized polynomial-type hyperelastic strain energy functions for near-incompressibility. Int. J. Solids Struct. (ISSN: 0020-7683) 40 (11), 2767–2791. http://dx.doi.org/10.1016/S0020-7683(03)00086-6, URL https://www.sciencedirect.com/science/article/pii/S0020768303000866.

Holthusen, Hagen, Brepols, Tim, Linka, Kevin, Kuhl, Ellen, 2025. Automated model discovery for tensional homeostasis: Constitutive machine learning in growth and remodeling. Comput. Biol. Med. (ISSN: 0010-4825) 186, 109691. http://dx.doi.org/10.1016/j.compbiomed.2025.109691, URL https://www.sciencedirect.com/science/article/pii/S0010482525000411.

Holthusen, Hagen, Lamm, Lukas, Brepols, Tim, Reese, Stefanie, Kuhl, Ellen, 2024a. Theory and implementation of inelastic constitutive artificial neural networks. Comput. Methods Appl. Mech. Engrg. (ISSN: 0045-7825) 428, 117063. http://dx.doi.org/10.1016/j.cma.2024.117063, URL https://www.sciencedirect.com/science/article/pii/S0045782524003190.

Holthusen, Hagen, Lamm, Lukas, Brepols, Tim, Reese, Stefanie, Kuhl, Ellen, 2024b. Polyconvex inelastic constitutive artificial neural networks. PAMM 24 (3), e202400032. http://dx.doi.org/10.1002/pamm.202400032.

Holthusen, Hagen, Rothkranz, Christiane, Lamm, Lukas, Brepols, Tim, Reese, Stefanie, 2023a. Inelastic material formulations based on a co-rotated intermediate configuration—Application to bioengineered tissues. J. Mech. Phys. Solids (ISSN: 0022-5096) 172, 105174. http://dx.doi.org/10.1016/j.jmps.2022.105174, URL https://www.sciencedirect.com/science/article/pii/S0022509622003507.

Holthusen, Hagen, Rothkranz, Christiane, Lamm, Lukas, Brepols, Tim, Reese, Stefanie, 2023b. A novel anisotropic stress-driven model for bioengineered tissues accounting for remodeling and reorientation based on homeostatic surfaces. PAMM 22 (1), e202200015. http://dx.doi.org/10.1002/pamm.202200015, arXiv:https://onlinelibrary.wiley.com/doi/pdf/10.1002/pamm.202200015. URL https://onlinelibrary.wiley.com/doi/abs/10.1002/pamm.202200015.

Holtzman, B.K., Chrysochoos, A., Daridon, L., 2018. A thermomechanical framework for analysis of microstructural evolution: Application to olivine rocks at high temperature. J. Geophys. Res.: Solid Earth 123 (10), 8474–8507. http://dx.doi.org/10.1029/2018JB015613, arXiv:https://agupubs.onlinelibrary.wiley.com/doi/pdf/10.1029/2018JB015613. URL https://agupubs.onlinelibrary.wiley.com/doi/abs/10.1029/2018JB015613.

Hornik, Kurt, Stinchcombe, Maxwell, White, Halbert, 1989. Multilayer feedforward networks are universal approximators. Neural Netw. (ISSN: 0893-6080) 2 (5), 359–366. http://dx.doi.org/10.1016/0893-6080(89)90020-8, URL https://www.sciencedirect.com/science/article/pii/0893608089900208.

Hossain, Mokarram, Vu, Duc Khoi, Steinmann, Paul, 2012. Experimental study and numerical modelling of VHB 4910 polymer. Comput. Mater. Sci. (ISSN: 0927-0256) 59, 65–74. http://dx.doi.org/10.1016/j.commatsci.2012.02.027, URL https://www.sciencedirect.com/science/article/pii/S0927025612001152.

Hudobivnik, Blaž, Korelc, Jože, 2016. Closed-form representation of matrix functions in the formulation of nonlinear material models. Finite Elem. Anal. Des. (ISSN: 0168-874X) 111, 19–32. http://dx.doi.org/10.1016/j.finel.2015.12.002, URL https://www.sciencedirect.com/science/article/pii/S0168874X15001845.

Jadoon, Asghar Arshad, Meyer, Knut Andreas, Fuhg, Jan Niklas, 2025. Automated model discovery of finite strain elastoplasticity from uniaxial experiments. Comput. Methods Appl. Mech. Engrg. (ISSN: 0045-7825) 435, 117653. http://dx.doi.org/10.1016/j.cma.2024.117653, URL https://www.sciencedirect.com/science/article/pii/S0045782524009071.

Kalina, Karl A., Gebhart, Philipp, Brummund, Jörg, Linden, Lennart, Sun, WaiChing, Kästner, Markus, 2024. Neural network-based multiscale modeling of finite strain magneto-elasticity with relaxed convexity criteria. Comput. Methods Appl. Mech. Engrg. (ISSN: 0045-7825) 421, 116739. http://dx.doi.org/10.1016/j.cma.2023.116739, URL https://www.sciencedirect.com/science/article/pii/S0045782523008629.

Kepner, Jeremy, Cho, Kenjiro, Claffy, KC, Gadepally, Vijay, Michaleas, Peter, Milechin, Lauren, 2019. Hypersparse neural network analysis of large-scale internet traffic. In: 2019 IEEE High Performance Extreme Computing Conference. HPEC, pp. 1–11. http://dx.doi.org/10.1109/HPEC.2019.8916263.

Kestin, Joseph, Rice, John R., 1969. Paradoxes in the Application of Thermodynamics to Strained Solids. pp. 275–298, URL https://api.semanticscholar.org/CorpusID:14356083.

Kingma, Diederik P., Ba, Jimmy, 2017. Adam: A method for stochastic optimization. arXiv:1412.6980. URL https://arxiv.org/abs/1412.6980.

Klein, Dominik K., Roth, Fabian J., Valizadeh, Iman, Weeger, Oliver, 2023. Parametrized polyconvex hyperelasticity with physics-augmented neural networks. Data-Centric Eng. 4, e25. http://dx.doi.org/10.1017/dce.2023.21.

Kröner, Ekkehart, 1959. Allgemeine kontinuumstheorie der versetzungen und eigenspannungen. Arch. Ration. Mech. Anal. (ISSN: 1432-0673) 4 (1), 273–334. http://dx.doi.org/10.1007/BF00281393.

Le, B.A., Yvonnet, J., He, Q.-C., 2015. Computational homogenization of nonlinear elastic materials using neural networks. Internat. J. Numer. Methods Engrg. 104 (12), 1061–1084. http://dx.doi.org/10.1002/nme.4953, arXiv:https://onlinelibrary.wiley.com/doi/pdf/10.1002/nme.4953. URL https://onlinelibrary.wiley.com/doi/abs/10.1002/nme.4953.

Lemaitre, J., Chaboche, J.-L., 1994. Mechanics of Solid Materials. Cambridge University Press.

Leuschner, M., Fritzen, F., van Dommelen, J.A.W., Hoefnagels, J.P.M., 2015. Potential-based constitutive models for cohesive interfaces: Theory, implementation and examples. Compos. Part B: Eng. (ISSN: 1359-8368) 68, 38–50. http://dx.doi.org/10.1016/j.compositesb.2014.08.024, URL https://www.sciencedirect.com/science/article/pii/S1359836814003461.

Linden, Lennart, Klein, Dominik K., Kalina, Karl A., Brummund, Jörg, Weeger, Oliver, Kästner, Markus, 2023. Neural networks meet hyperelasticity: A guide to enforcing physics. J. Mech. Phys. Solids (ISSN: 0022-5096) 179, 105363. http://dx.doi.org/10.1016/j.jmps.2023.105363, URL https://www.sciencedirect.com/science/article/pii/S0022509623001679.

Linka, Kevin, Hillgärtner, Markus, Abdolazizi, Kian P., Aydin, Roland C., Itskov, Mikhail, Cyron, Christian J., 2021. Constitutive artificial neural networks: A fast and general approach to predictive data-driven constitutive modeling by deep learning. J. Comput. Phys. (ISSN: 0021-9991) 429, 110010. http://dx.doi.org/10.1016/j.jcp.2020.110010, URL https://www.sciencedirect.com/science/article/pii/S0021999120307841.

Linka, Kevin, Holzapfel, Gerhard A., Kuhl, Ellen, 2025. Discovering uncertainty: Bayesian constitutive artificial neural networks. Comput. Methods Appl. Mech. Engrg. (ISSN: 0045-7825) 433, 117517. http://dx.doi.org/10.1016/j.cma.2024.117517, URL https://www.sciencedirect.com/science/article/pii/S0045782524007710.

Linka, Kevin, Kuhl, Ellen, 2023. A new family of constitutive artificial neural networks towards automated model discovery. Comput. Methods Appl. Mech. Engrg. (ISSN: 0045-7825) 403, 115731. http://dx.doi.org/10.1016/j.cma.2022.115731, URL https://www.sciencedirect.com/science/article/pii/S0045782522006867.

Linka, Kevin, Kuhl, Ellen, 2024. Best-in-class modeling: A novel strategy to discover constitutive models for soft matter systems. Extrem. Mech. Lett. (ISSN: 2352-4316) 70, 102181. http://dx.doi.org/10.1016/j.eml.2024.102181, URL https://www.sciencedirect.com/science/article/pii/S2352431624000610.

Masi, Filippo, Stefanou, Ioannis, 2022. Multiscale modeling of inelastic materials with thermodynamics-based artificial neural networks (TANN). Comput. Methods Appl. Mech. Engrg. (ISSN: 0045-7825) 398, 115190. http://dx.doi.org/10.1016/j.cma.2022.115190, URL https://www.sciencedirect.com/science/article/pii/S0045782522003450.

Masi, Filippo, Stefanou, Ioannis, 2023. Evolution TANN and the identification of internal variables and evolution equations in solid mechanics. J. Mech. Phys. Solids (ISSN: 0022-5096) 174, 105245. http://dx.doi.org/10.1016/j.jmps.2023.105245, URL https://www.sciencedirect.com/science/article/pii/S0022509623000492.

Masi, Filippo, Stefanou, Ioannis, Vannucci, Paolo, Maffi-Berthier, Victor, 2021. Thermodynamics-based artificial neural networks for constitutive modeling. J. Mech. Phys. Solids (ISSN: 0022-5096) 147, 104277. http://dx.doi.org/10.1016/j.jmps.2020.104277, URL https://www.sciencedirect.com/science/article/pii/S0022509620304841.

Matzenmiller, A., Lubliner, J., Taylor, R.L., 1995. A constitutive model for anisotropic damage in fiber-composites. Mech. Mater. (ISSN: 0167-6636) 20 (2), 125–152. http://dx.doi.org/10.1016/0167-6636(94)00053-0.

McCulloch, Jeremy A., St. Pierre, Skyler R., Linka, Kevin, Kuhl, Ellen, 2024. On sparse regression, L-regularization, and automated model discovery. Internat. J. Numer. Methods Engrg. 125 (14), e7481. http://dx.doi.org/10.1002/nme.7481, arXiv:https://onlinelibrary.wiley.com/doi/pdf/10.1002/nme.7481. URL https://onlinelibrary.wiley.com/doi/abs/10.1002/nme.7481.

Mozaffar, M., Bostanabad, R., Chen, W., Ehmann, K., Cao, J., Bessa, M.A., 2019. Deep learning predicts path-dependent plasticity. Proc. Natl. Acad. Sci. 116 (52), 26414–26420. http://dx.doi.org/10.1073/pnas.1911815116, arXiv:https://www.pnas.org/doi/pdf/10.1073/pnas.1911815116. URL https://www.pnas.org/doi/abs/10.1073/pnas.1911815116.

Nagle, Matt, Conroy Broderick, Hannah, Buganza Tepole, Adrian, Fop, Michael, Ní Annaidh, Aisling, 2024. A machine learning approach to predict in vivo skin growth. Sci. Rep. (ISSN: 2045-2322) 14 (1), 17456. http://dx.doi.org/10.1038/s41598-024-67056-z.

Pedregosa, Fabian, 2016. Hyperparameter optimization with approximate gradient. In: Balcan, Maria Florina, Weinberger, Kilian Q. (Eds.), Proceedings of the 33rd International Conference on Machine Learning. In: Proceedings of Machine Learning Research, vol. 48, PMLR, New York, New York, USA, pp. 737–746, URL https://proceedings.mlr.press/v48/pedregosa16.html.

Pedroso, Dorival M., Sheng, Daichao, Sloan, Scott W., 2008. Stress update algorithm for elastoplastic models with nonconvex yield surfaces. Internat. J. Numer. Methods Engrg. 76 (13), 2029–2062. http://dx.doi.org/10.1002/nme.2407, arXiv:https://onlinelibrary.wiley.com/doi/pdf/10.1002/nme.2407. URL https://onlinelibrary.wiley.com/doi/abs/10.1002/nme.2407.

Piunno, Giovanni, Stefanou, Ioannis, Jommi, Cristina, 2025. A POD-TANN approach for the multiscale modeling of materials and macro-element derivation in geomechanics. Int. J. Numer. Anal. Methods Geomech. 49 (2), 700–719. http://dx.doi.org/10.1002/nag.3891, arXiv:https://onlinelibrary.wiley.com/doi/pdf/10.1002/nag.3891. URL https://onlinelibrary.wiley.com/doi/abs/10.1002/nag.3891.

Prume, E., Gierden, C., Ortiz, M., Reese, S., 2025. Direct data-driven algorithms for multiscale mechanics. Comput. Methods Appl. Mech. Engrg. (ISSN: 0045-7825) 433, 117525. http://dx.doi.org/10.1016/j.cma.2024.117525, URL https://www.sciencedirect.com/science/article/pii/S0045782524007795.

Prume, E., Reese, S., Ortiz, M., 2023. Model-free data-driven inference in computational mechanics. Comput. Methods Appl. Mech. Engrg. (ISSN: 0045-7825) 403, 115704. http://dx.doi.org/10.1016/j.cma.2022.115704, URL https://www.sciencedirect.com/science/article/pii/S0045782522006594.

Reese, Stefanie, Govindjee, Sanjay, 1998. A theory of finite viscoelasticity and numerical aspects. Int. J. Solids Struct. (ISSN: 0020-7683) 35 (26), 3455–3482. http://dx.doi.org/10.1016/S0020-7683(97)00217-5, URL https://www.sciencedirect.com/science/article/pii/S0020768397002175.

Rodriguez, Edward K., Hoger, Anne, McCulloch, Andrew D., 1994. Stress-dependent finite growth in soft elastic tissues. J. Biomech. (ISSN: 0021-9290) 27 (4), 455–467. http://dx.doi.org/10.1016/0021-9290(94)90021-3, URL https://www.sciencedirect.com/science/article/pii/0021929094900213.

Rosenkranz, Max, Kalina, Karl A., Brummund, Jörg, Sun, WaiChing, Kästner, Markus, 2024. Viscoelasticty with physics-augmented neural networks: model formulation and training methods without prescribed internal variables. Comput. Mech. (ISSN: 1432-0924) http://dx.doi.org/10.1007/s00466-024-02477-1.

Shannon, C.E., 1948. A mathematical theory of communication. Bell Syst. Tech. J. (ISSN: 0005-8580) 27 (3), 379–423. http://dx.doi.org/10.1002/j.1538-7305.1948.tb01338.x.

Sheng, Daichao, Augarde, Charles E., Abbo, Andrew J., 2011. A fast algorithm for finding the first intersection with a non-convex yield surface. Comput. Geotech. (ISSN: 0266-352X) 38 (4), 465–471. http://dx.doi.org/10.1016/j.compgeo.2011.02.008, URL https://www.sciencedirect.com/science/article/pii/S0266352X11000255.

Sherman, Jack, Morrison, Winifred J., 1950. Adjustment of an inverse matrix corresponding to a change in one element of a given matrix. Ann. Math. Stat. 21 (1), 124–127. http://dx.doi.org/10.1214/aoms/1177729893.

Sidoroff, F., 1974. UN modele viscoelastique non lineaire avec configuration intermediaire. J. MEC.; FR.; DA. 1974; VOL. 13; NO 4; PP. 679-713; ABS. ANGL.; BIBL. 18 REF..

Spencer, AJM, 1971. Part III. Theory of invariants. Contin. Phys. 1, 239–353.

Stassi-D'Alia, Ferdinando, 1967. Flow and fracture of materials according to a new limiting condition of yelding. Meccanica (ISSN: 1572-9648) 2 (3), 178–195. http://dx.doi.org/10.1007/BF02128173.

Sun, Yanan, Xue, Bing, Zhang, Mengjie, Yen, Gary G., 2019. Completely automated CNN architecture design based on blocks. IEEE Trans. Neural Netw. Learn. Syst. 31 (4), 1242–1254.

Svendsen, Bob, 2001. On the modelling of anisotropic elastic and inelastic material behaviour at large deformation. Int. J. Solids Struct. (ISSN: 0020-7683) 38 (52), 9579–9599. http://dx.doi.org/10.1016/S0020-7683(01)00140-8, URL http://www.sciencedirect.com/science/article/pii/S0020768301001408.

Tac, Vahidullah, Kuhl, Ellen, Tepole, Adrian Buganza, 2024. Data-driven continuum damage mechanics with built-in physics. Extrem. Mech. Lett. (ISSN: 2352-4316) 71, 102220. http://dx.doi.org/10.1016/j.eml.2024.102220, URL https://www.sciencedirect.com/science/article/pii/S2352431624001007.

Tac, Vahidullah, Sahli Costabal, Francisco, Tepole, Adrian B., 2022. Data-driven tissue mechanics with polyconvex neural ordinary differential equations. Comput. Methods Appl. Mech. Engrg. (ISSN: 0045-7825) 398, 115248. http://dx.doi.org/10.1016/j.cma.2022.115248, URL https://www.sciencedirect.com/science/article/pii/S0045782522003838.

Tschoegl, N.W., 1971. Failure surfaces in principal stress space. J. Polym. Sci. Part C: Polym. Symp. 32 (1), 239–267. http://dx.doi.org/10.1002/polc.5070320113, arXiv:https://onlinelibrary.wiley.com/doi/pdf/10.1002/polc.5070320113. URL https://onlinelibrary.wiley.com/doi/abs/10.1002/polc.5070320113.

Upadhyay, Kshitiz, Fuhg, Jan N., Bouklas, Nikolaos, Ramesh, K.T., 2024. Physics-informed data-driven discovery of constitutive models with application to strain-rate-sensitive soft materials. Comput. Mech. (ISSN: 1432-0924) http://dx.doi.org/10.1007/s00466-024-02497-x.

von Mises, Richard, 1913. Mechanik der festen körper im plastisch- deformablen zustand. Nachrichten Von der Ges. der Wiss. Zu Gött., Mathematisch-Physikalische Kl. 1913, 582–592, URL http://eudml.org/doc/58894.

Watson, Joe, Song, Chen, Weeger, Oliver, Gruner, Theo, Le, An T., Hansel, Kay, Hendawy, Ahmed, Arenz, Oleg, Trojak, Will, Cranmer, Miles, D'Eramo, Carlo, Bülow, Fabian, Goyal, Tanmay, Peters, Jan, Hoffman, Martin W., 2024. Machine learning with physics knowledge for prediction: A survey. arXiv:2408.09840. URL https://arxiv.org/abs/2408.09840.

Wu, Jia, Chen, SenPeng, Liu, XiYuan, 2020. Efficient hyperparameter optimization through model-based reinforcement learning. Neurocomputing (ISSN: 0925-2312) 409, 381–393. http://dx.doi.org/10.1016/j.neucom.2020.06.064, URL https://www.sciencedirect.com/science/article/pii/S0925231220310523.

Xu, Haotian, Flaschel, Moritz, De Lorenzis, Laura, 2025. Discovering non-associated pressure-sensitive plasticity models with EUCLID. Adv. Model. Simul. Eng. Sci. (ISSN: 2213-7467) 12 (1), 1. http://dx.doi.org/10.1186/s40323-024-00281-3.

Xu, Jiaxing, Yang, Yunhan, Huang, David Tse Jung, Gururajapathy, Sophi Shilpa, Ke, Yiping, Qiao, Miao, Wang, Alan, Kumar, Haribalan, McGeown, Josh, Kwon, Eryn, 2023. Data-driven network neuroscience: On data collection and benchmark. arXiv:2211.12421. URL https://arxiv.org/abs/2211.12421.

Yi, Ruibang, Georgiou, Dimitrios, Liu, Xing, Athanasiou, Christos E., 2025. Mechanics-informed, model-free symbolic regression framework for solving fracture problems. J. Mech. Phys. Solids (ISSN: 0022-5096) 194, 105916. http://dx.doi.org/10.1016/j.jmps.2024.105916, URL https://www.sciencedirect.com/science/article/pii/S002250962400382X.

Zhang, Pin, Karapiperis, Konstantinos, Weeger, Oliver, 2025. T-PiNet: A thermodynamics-informed hierarchical learning for discovering constitutive relations of geomaterials. J. Mech. Phys. Solids (ISSN: 0022-5096) 197, 106049. http://dx.doi.org/10.1016/j.jmps.2025.106049, URL https://www.sciencedirect.com/science/article/pii/S0022509625000250.

Zhang, Yichi, Seibert, Paul, Otto, Alexandra, Raßloff, Alexander, Ambati, Marreddy, Kästner, Markus, 2024. DA-VEGAN: Differentiably augmenting VAE-GAN for microstructure reconstruction from extremely small data sets. Comput. Mater. Sci. (ISSN: 0927-0256) 232, 112661. http://dx.doi.org/10.1016/j.commatsci.2023.112661, URL https://www.sciencedirect.com/science/article/pii/S0927025623006559.

Zheng, Q.-S., 1994. Theory of representations for tensor functions—A unified invariant approach to constitutive equations. Appl. Mech. Rev. (ISSN: 0003-6900) 47 (11), 545–587. http://dx.doi.org/10.1115/1.3111066, arXiv:https://asmedigitalcollection.asme.org/appliedmechanicsreviews/article-pdf/47/11/545/5436932/545_1.pdf.